nature cancer

Resource

https://doi.org/10.1038/s43018-025-01072-4

A single-cell atlas characterizes dysregulation of the bone marrow immune microenvironment associated with outcomes in multiple myeloma

Received: 17 March 2025

Accepted: 10 October 2025

Published online: 09 January 2026

Check for updates

A list of authors and their affiliations appears at the end of the paper

Multiple myeloma (MM) remains incurable despite advances in treatment options. Although tumor subtypes and specific DNA abnormalities are linked to worse prognosis, the impact of immune dysfunction on disease emergence and/or treatment sensitivity remains unclear. We developed an Immune Atlas of MM by generating profiles of 1,397,272 single cells from the bone marrow (BM) of 337 newly diagnosed participants and characterized immune and hematopoietic cell populations. Cytogenetic risk-based analysis revealed heterogeneous associations with T cells of BM, with 17p13 deletion showing distinct enrichment of a type 1 interferon signature. The disease progression-based analysis revealed the presence of a proinflammatory immune senescence-associated secretory phenotype in rapidly progressing participants. Furthermore, signaling analyses suggested active intercellular communication involving a proliferation-inducing ligand and B cell maturation antigen, potentially promoting tumor growth and survival. Lastly, using independent discovery and validation cohorts, we demonstrated that integrating immune cell signatures with known tumor cytogenetics and individual characteristics significantly improves stratification for the prediction of survival.

Multiple myeloma (MM) is the second most prevalent hematological cancer and its incidence continues to rise globally[1,2]. An estimated 35,780 new diagnoses and 12,540 deaths are projected for 2024 in the United States[3]. The emergence of myeloma-targeting biologic and immune-based therapies has led to notable improvements in outcomes[4]. Nevertheless, curative outcomes are characteristically elusive and most persons with MM eventually succumb to the disease. Disease evolution is associated with progressive immune dysregulation. With the recent US Food and Drug Administration approval of immunotherapies such as chimeric antigen receptor (CAR) T cells and bispecific T cell engagers, understanding the immune elements in the myeloma microenvironment has become increasingly important for addressing disease emergence and/or response to treatment. Over the past 15 years, multiple studies[5–10], including the Clinical Outcomes in MM to Personal Assessment of Genetic Profiles (CoMMpass) registry[8,11], have investigated the genomic landscape and diversity of MM and identified specific tumor subtypes and their underlying associations with clinical outcomes. Furthermore, these studies have demonstrated that, like other cancers, MM tumors are multiclonal, with their clonal makeup evolving over the course of the disease progression and exposure to treatments. Notably, prognostic models leveraging these genetic determinants are limited in their capacity to identify high-risk (HR) participants for early relapse. This suggests that latent, tumor-extrinsic factors contributing to prognosis are not captured by current models.

The bone marrow (BM) microenvironment (BMME) composition in MM has been identified as a factor affecting tumor progression and therapeutic outcomes. Recent studies have pointed to T cell exhaustion[12,13] and the infiltration of immunomodulatory cell populations contributing to immunoediting and immune evasion in MM, such as myeloid-derived suppressor cells (MDSCs), regulatory T cells (Treg),

e-mail: mulligang@themmrf.org; lding@genome.wustl.edu; sacha.gnjatic@mssm.edu; ivlachos@bidmc.harvard.edu; manoj.bhasin@emory.edu

Th17 cells, dendritic cells (DCs) and dysregulated natural killer (NK) cells, as well as tumor-associated neutrophils and macrophages[14–17]. We hypothesized that profiling the BMME of persons with newly diagnosed MM (NDMM) before treatment with standard myeloma therapies could reveal immune populations and signaling pathways associated with disease emergence or clinical outcomes. Such insights can be used to refine current participant stratification tools including the revised International Staging System (R-ISS) and, importantly, inform strategies for target identification and rational integration of various immunotherapies in MM.

To this end, we generated a BMME Immune Atlas of participants with NDMM from the MM Research Foundation (MMRF) CoMMpass study (NCT01454297), which included corresponding detailed clinical and genomic information. We profiled and analyzed 1,149,344 cells from 263 participants with NDMM during the discovery phase to identify immune populations and phenotypes associated with MM subtypes and participant survival. These findings were further validated by generating profiles of an additional 247,928 cells from 74 participants with NDMM.

Results

An MM BMME cell atlas

To characterize the BMME of MM, we profiled CD138$^-$ BM aspirate from 263 and 74 participants with NDMM as discovery and validation cohorts, respectively (Fig. 1a and Extended Data Fig. 1a–e). The demographic and clinical characteristics of the discovery cohort are reflective of the CoMMpass study (Supplementary Table 1), including median age (62.9 versus 64.1 years), African American percentage (16.6% versus 17.5%), ISS stage 3 (27.9% versus 26.3%) and HR cytogenetics[18] (51.6% versus 53.2%) (Fig. 1b and Supplementary Table 1). Therapeutically, 184 participants initially received a combination of proteasome inhibitors (PIs), immunomodulatory drugs (IMiDs) and steroids, while 135 underwent autologous stem cell transplantation (ASCT) as first-line therapy (Fig. 1c). All samples were profiled using our previously standardized single-cell RNA sequencing (scRNA-seq) protocol[12,19,20].

Initially, we examined how the participant's immune landscape varied according to tumor type by stratifying participants on the basis of individual cytogenetic alterations, including del(17p13), t(14;16)[*MAF*], t(8;14)[*MAFA*], t(14;20)[*MAFB*], t(4;14)[W*HSC1/MMSET/NSD2*] and gain(1q21). We also investigated combining these cytogenetic alterations to define HR and standard-risk (SR) participants using the Davies risk definition[18] (Fig. 1d,e and Supplementary Table 2). We additionally stratified participants on the basis of their disease progression kinetics into rapid progressors (RPs; $n_{discovery} = 67$, $n_{validation} = 29$), with progression events occurring within 18 months of diagnosis, and nonprogressors (NPs; $n_{discovery} = 83$, $n_{validation} = 35$), with durable remission for at least 4 years following treatment (Fig. 1f,g). Interestingly, while evaluation of the discovery cohort confirmed that most HR participants were mainly associated with RPs and vice versa, we identified 32 HR participants as NPs and 19 SR participants as RPs, indicating that other factors, such as the immune environment, might have additional critical roles (Fig. 1f). As expected, participants categorized as SR had improved progression-free survival (PFS) relative to HR participants, suggesting that our risk classification strategy was informative for predicting outcomes (Fig. 1h; $P = 0.007$). Additionally, survival analysis on other clinical variables also demonstrated that discovery cohort participants who either underwent BM transplant ($P = 9.32 \times 10^{-8}$) or received triplet treatment (PI, IMiD and steroid) ($P = 0.0002$) or who were classified as ISS stage I had significantly ($P < 5.29 \times 10^{-6}$) better outcomes (Fig. 1h). Similar patterns of outcomes were also observed in the validation cohort, underscoring the similarity in our discovery and validation cohorts (Extended Data Fig. 1e and Supplementary Table 3).

Single-cell transcriptome profiling identifies traditional and rare cell populations of the myeloma BMME

Across 1,149,344 high-quality BM cells (Fig. 2a) the baseline BMME consisted of T cells (30.51% CD8$^+$, 23.39% CD4$^+$), NK cells (6.82%), B cells (8.51%), myeloid cells (12.20%), erythroblasts and erythrocytes (7.87%) and plasma cells (9.17%), with the remainder comprising small, independent populations (hematopoietic stem cells (HSCs), plasmacytoid DCs (pDCs) and fibroblasts; 1.53%) (Fig. 2b,c). Canonical lineage markers were used for cell type and subtype annotation (Fig. 2b,c). The cellular profiles showed subtle variations associated with the processing sites (that is, Mayo, Emory, Washington University and Icahn School of Medicine at Mount Sinai) and batch-corrected using the Harmony approach (Extended Data Fig. 2a–f).

The T and NK cell compartment formed 30 clusters across CD4$^+$ (11 clusters), CD8$^+$ (15 clusters) and NK (four clusters) cell populations (Fig. 2d,e and Extended Data Fig. 3a–c). CD4$^+$ T cell clusters comprised naive (Tn), central memory (Tcm), effector (Teff) memory, Treg and helper (Th) cells (Fig. 2f and Extended Data Fig. 3b). This large-scale analysis also enabled the identification of rare cytotoxic CD4$^+$ T cells with high expression of *GZMB* and *PRF1* markers. Similarly, the CD8$^+$ T cell population also comprised multiple clusters of memory and Teff cells, as well as activated Teff subtypes (that is, CD8_Teff_HLA) with low expression of cytotoxic markers but high expression of human leukocyte antigen (HLA) markers (Fig. 2g and Extended Data Fig. 3c). The NK cell clusters comprised classical CD56$^{+bright}$ and CD56^{+dim} cell types, as well as rare adaptive and BM-resident cell types (Fig. 2h).

The myeloid lineage comprised 18 clusters of classical CD14$^+$ and nonclassical CD16$^+$ monocytes, granulocytes, neutrophils, conventional DCs (cDCs), pDCs and macrophages (Fig. 2i,j). The B cell compartment contained pro-B cells, as well as immature transitional, naive and memory B cells (Fig. 2k,l). The compartment also captured immature hematopoietic populations, such as HSCs, mast cells and erythroblasts. A distinct population of mature erythrocytes was observed (Extended Data Fig. 3d,e), with nine subclusters exhibiting minimal participant-specific heterogeneity.

The plasma cells, ~9.17% of cells on average in baseline samples (Extended Data Fig. 3f–h), were likely residual myeloma cells that

Fig. 1 | Overview of the Immune Atlas design, workflow and participant characteristics. a, Overview of the Immune Atlas study design, discovery ($n_{participants} = 263$) and validation ($n_{participants} = 74$) participant cohorts, sample processing and analysis workflow. **b**, Clinical characteristics of participants ($n_{participants} = 263$) in the discovery cohort. The forest plot illustrates the effect of various clinical features on PFS. Error bars display the 95% confidence interval (CI). **c**, Dot plot depicting the cross-section of samples based on ASCT and frontline treatment, where the dot size indicates the number of participants and dot color indicates the type of treatment regimen. **d**, Bar chart showing the total number of participants with each of the six genetic events used for risk classification. **e**, UpSet plot showing the distribution of the major cytogenetic abnormalities comprising the Davies-based HR myeloma definition. **f**, UpSet plot showing the intersection of participants categorized as SR or HR and NP or RP at baseline. **g**, Overview of progression group categorization and study design for the discovery cohort. The participants with a progression event within the first 18 months following therapy were classified as RPs ($n_{participants} = 67$). Participants with durable remission or no observed progression for at least 4 years were classified as NPs ($n_{participants} = 83$). Participants with a progression event between 18 months and 4 years were classified as RPs ($n_{participants} = 71$). The participants who exited the study before 4 years of disease diagnosis without experiencing a progression event were classified as Inc ($n = 42$). **h**, Kaplan–Meier curves display the survival analysis for participants categorized on the basis of risk stratification (HR versus SR), transplant as a frontline treatment, treatment type and ISS staging. Participants lacking ISS stage information at baseline or WGS information for cytogenetic risk stratification were omitted from the relevant figure panels. The *P* values were estimated using a log-rank test. **a** and **g** were created with BioRender.com.

https://doi.org/10.1038/s43018-025-01072-4

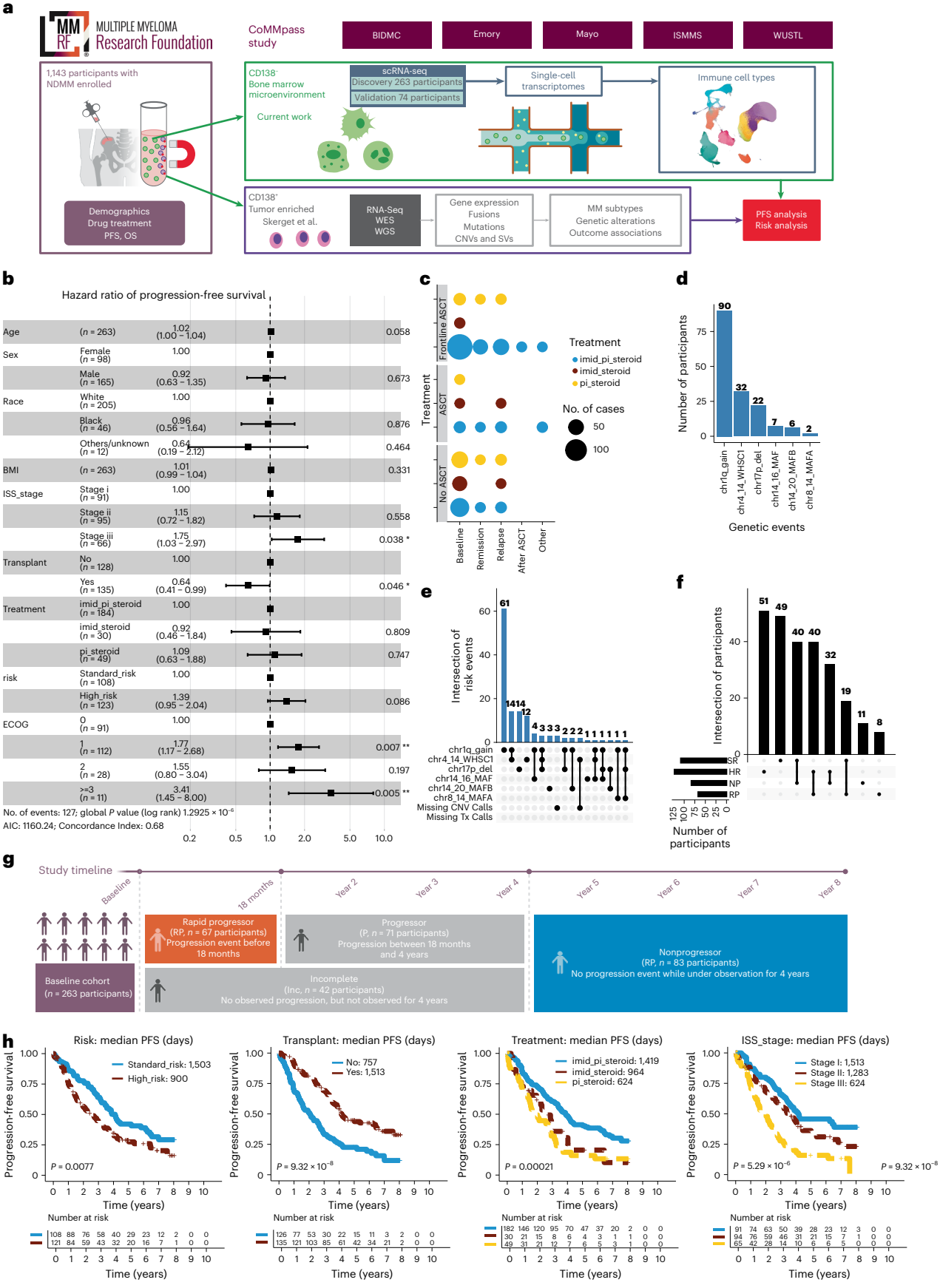

https://doi.org/10.1038/s43018-025-01072-4

were not effectively depleted by CD138 bead selection. The number of plasma cells was significantly correlated with levels of plasma cells measured before the CD138 selection step, indicating the inefficiency of the bead selection method for samples with high tumor cell content (Extended Data Fig. 3i,j; $R^2 = 0.63$, $P = 1.68 \times 10^{-56}$). Plasma cells captured in scRNA-seq also showed enrichment for mutations in the driver genes, indicating that these were malignant cells (Extended Data Fig. 3k). The higher malignant plasma cell proportions were associated with RPs, with potential implications for participant outcomes (Extended Data Fig. 3l,m).

Analysis of tumor cytogenetic subgroups reveals heterogeneous impact on T cell compartment

To explore the potential relationship between tumor cytogenetic subgroups and their BM immune microenvironment, we assessed key abnormalities, including 1q21 gain, translocations (t(4;14)[*NSD2*], t(14;16)[*MAF*], t(8;14)[*MAFA*] and t(14;20)[*MAFB*]) and 17p13 deletion. We also assessed the combined effects of these cytogenetic alterations by stratifying participants into HR and SR groups[18]. Overall, most immune populations had similar abundances across cytogenetic subgroups, both when combined and when individually assessed (Fig. 3a). Some differences in specific cell types were detectable, including a higher abundance of rare cytotoxic CD4$^+$ T cells in *NSD2* t(4;14) participants (Fig. 3a; $P = 0.017$). The participants with *NSD2* t(4;14) and 1q21 gain showed significant depletion of CD4$^+$IFN (interferon)$^+$ Teff memory ($P_{NSD2} = 0.043$, $P_{1q21} = 0.001$) and CD4$^+$IFN$^+$ Tcm cells ($P_{NSD2} = 0.043$, $P_{1q21} = 0.011$) (Fig. 3a). Interestingly, participants with *MAF* translocation exhibited significant dysregulation in the B cells rather than the T cells with depletion of naive and memory B cell populations ($P_{naive} = 0.001$, $P_{mem} = 0.004$) (Fig. 3a) and enrichment of immature B cell states ranging from the CD34$^+$ pro-B population to the transitional B cell population (Fig. 3a; $P < 0.005$). The *MAF* translocation participants also uniquely displayed significant enrichment of an immunosuppressive macrophage cluster (Fig. 3a; $P = 0.031$). Notably, across myeloid and T cell compartments, type 1 IFN (IFN-I) response-associated clusters depict reversed trends in participants with 17p13 deletion as compared to *NSD2* or 1q21 abnormalities. In contrast to the reductions in IFN-I-responsive CD4$^+$ memory populations observed in *NSD2* t(4;14) and 1q21 gain participants, participants with 17p13 deletion tended to possess a higher abundance of IFN-stimulated populations, with significant enrichment of CD4$^+$ Teff memory IFN-I cells (Fig. 3a; $P = 0.007$). Further combined analysis of these putative HR tumor abnormalities revealed significant enrichment of the late-activated CD8$^+$HLA$^+$ Teff (that is, CD8_Teff_HLA; $P = 0.041$) population and reduction in CD8$^+$ Tn cells and CD4$^+$TNF (tumor necrosis factor)$^+$ Teff cells ($P = 0.006$ and 0.042, respectively; Fig. 3a). This higher abundance of CD8_Teff_HLA Teff population was significantly associated with poor overall survival (OS) ($P = 0.036$; Extended Data Fig. 4a), and a trend toward worse PFS ($P = 0.062$; Extended Data Fig. 4b).

To further investigate the associations of individual HR abnormalities and their combined impact on the transcriptome, we conducted an in-depth analysis focusing on T cell compartments (Fig. 3b). Participants with *NSD2* and 1q21 gain showed higher-than-average expression of CD4$^+$ and CD8$^+$ T cell cytotoxicity and senescence-related genes (Fig. 3b). Interestingly, participants with *MAF* translocation showed higher exhaustion marker expression among CD8$^+$ T cells, a feature that was primarily found in the early activated GZMK$^+$ Teff memory cells (Extended Data Fig. 4c,d). The combined analysis of HR participants also highlighted overexpression of major histocompatibility complex class II (MHC-II) and cytotoxicity markers across CD8$^+$ T cells (Fig. 3b) driven by the higher abundance of the CD8_Teff_HLA population (Fig. 3c; $P = 0.016$). The interaction analysis of cytogenetic abnormalities suggested that the co-occurrence of *NSD2* and 1q21 gain significantly contributed toward the enrichment of the CD8_Teff_HLA Teff population (Fig. 3c; $P = 0.021$) associated with poor outcomes (Extended Data Fig. 4a,b). The trajectory analysis on the T cell compartment showed that the HR-enriched CD8_Teff_HLA population represented a transitional state between early activated CD8$^+$ memory to terminally differentiated cytotoxic populations (Fig. 3d). This population also showed enrichment of T cell dysfunction characteristics among participants with HR cytogenetics, measured as a function of the expression of exhaustion or senescence markers ($P = 2.35 \times 10^{-16}$; Fig. 3e, Extended Data Fig. 4c,d and Supplementary Table 4). This shift or accumulation of activated T cell states was mainly observed in participants with *NSD2* and 1q21 gain, while participants with biallelic 17p13 deletion or 17p13 deletion paired with a nonsynonymous *TP53* mutation had lower levels of differentiated CD8$^+$ T cells, possibly suggesting different immune escape mechanisms among the HR cytogenetic events (Fig. 3b and Extended Data Fig. 4e,f).

Tumor and microenvironment cells of participants with 17p13 deletions depict distinct enrichment of IFN-I signature

To further study the distinct IFN-I-associated gene expression enrichment observed in T cells of 17p13 participants across other compartments, we generated an IFN-I signature using top marker genes from T cell IFN-I clusters (Supplementary Table 4). Participants with elevated expression of the IFN-I signature in one lineage, such as T cells, showed overexpression across all other compartments, including malignant plasma cells (Extended Data Fig. 4g). Across risk groups, IFN-I signature enrichment was specific to 17p13 cytogenetic groups only (Fig. 3f). Further interaction analysis of 1q21 with other HR abnormalities indicated that IFN-I downregulation was primarily associated with 1q21

Fig. 2 | Single-cell Immune Atlas of samples from participants with MM. a, UMAP embedding of 1,149,344 CD138$^-$ BMME cells collected from participants with MM. A total of 106 clusters were observed, spanning five major compartments defined by canonical markers: T and NK cells, B cells and erythroblasts, myeloid cells, erythrocytes and plasma cells. Populations identified as doublets are colored gray. **b**, Feature plots displaying the normalized gene expression for a selection of lineage-specific markers. UMAPs and per-aliquot cluster compositions to depict the effects of batch correction for major lineages are shown in Extended Data Fig. 2. **c**, A stacked bar chart displaying the average per-participant cell type composition at baseline. Clusters are colored by their lineage and shaded by subtype. Doublet populations are omitted. **d**, UMAP of the T lymphocyte and NK compartment. Cells are colored by individual cell type, with shaded boundaries representing regions predominantly containing CD4$^+$ (purple), CD8$^+$ (orange) or NK (green) cells. The color for specific cell types is included in the corresponding dot plots (**f**–**h**). An extended dot plot for precise annotation of different T and NK cell subtypes is shown in Extended Data Fig. 3a. UMAPs for only the CD8$^+$ and CD4$^+$ T cells are also shown in Extended Data Fig. 3b,c. **e**, Feature plots displaying the normalized gene expression per cell for markers to distinguish CD4$^+$, CD8$^+$ and NK cells. **f**–**h**, Dot plots displaying the average scaled expression of select marker genes used for precise cluster annotation. Expression is visualized on a red–blue color scale, with the size of each dot corresponding to the percentage expression. Dot plots are split by lineage into NK cells (**f**), CD8$^+$ T cells (**g**) and CD4$^+$ T cells (**h**). The colored triangle next to the cluster name matches the cluster color in the corresponding UMAP (**d**). Percent.mt refers to the percentage of mitochondrial transcripts. **i**, UMAP of the myeloid compartment. Cells are shaded by their subtype. Doublet populations are colored gray. **j**, Dot plot displaying the average scaled expression of select marker genes for precise cluster annotation in the myeloid compartment. Expression is visualized on a red–blue color scale, with the size of each dot corresponding to the percentage expression. The triangle next to the cluster name matches the cluster color in the corresponding UMAP. **k**, UMAP of the B cell and erythroblast compartment. Cells are colored by their lineage (B cells, cyan; erythrocytes, red; others, dark blue), shaded by subtype. Doublet populations are colored gray. **l**, Dot plot displaying the average scaled expression of select marker genes used for precise cluster annotation in the B cell and erythroblast compartment. Expression is visualized on a red–blue color scale, with the size of each dot corresponding to the percentage expression.

https://doi.org/10.1038/s43018-025-01072-4

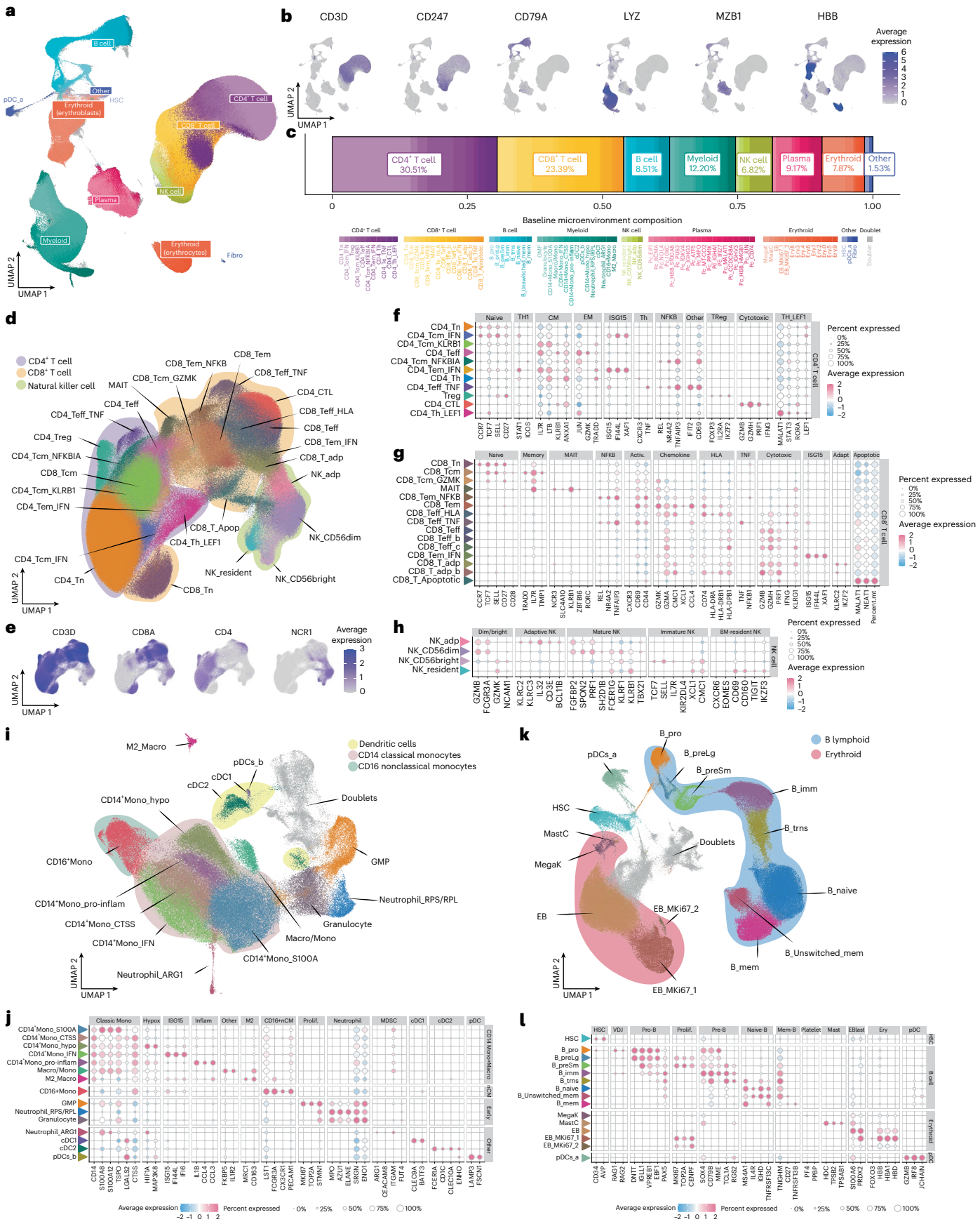

https://doi.org/10.1038/s43018-025-01072-4

gain (Extended Data Fig. 4h; $P < 0.05$). Conversely, enrichment of IFN-I populations was strongly associated with participants having a complete loss of *TP53* (Extended Data Fig. 4i; $P < 0.05$). This IFN-I signature enrichment in the plasma cells from scRNA-seq was confirmed on independently generated bulk RNA-seq data from CD138$^+$ malignant cells of these participants ($R^2 = 0.75$, $P = 1.63 \times 10^{-32}$; Fig. 3g). Analysis of CD138$^+$ bulk RNA-seq data from the CoMMpass cohort ($n_{participants} = 660$) confirmed opposite IFN-I activity patterns between 1q21 gain and TP53 loss; participants with 1q21 gain or amplification showed reduced IFN-I activity (Fig. 3h; $P = 0.003$), whereas those with partial or complete TP53 loss exhibited increased activity (Fig. 3i; $P = 0.015$).

Furthermore, we also examined additional HR abnormalities, including chromothripsis and APOBEC (apolipoprotein B mRNA-editing enzyme, catalytic polypeptide) activity, which showed no T cell dysregulation but some alterations in myeloid and B cell compartments (Extended Data Fig. 4j).

GZMK$^+$ Teff memory cell level correlates with the abundance of myeloma cells

In addition, we also examined the impact of plasma cell levels on immune cells and, as expected, most nonmalignant BM populations were reduced in participants with elevated plasma cell levels (Fig. 3j). However, GZMK$^+$CD8$^+$ Teff memory cells, BM-resident NK cells and fibroblasts showed significant positive correlations with plasma cell percentages ($P = 2.4 \times 10^{-9}$; Fig. 3k–m and Extended Data Fig. 4k–m). In participants with higher plasma cell percentages, CD8$^+$ T cells showed increased TIGIT and TOX expression ($P = 0.035$ and 0.014, respectively; Fig. 3n), mainly within GZMK$^+$ Teff memory cells (Extended Data Fig. 4c,d), suggesting that high plasma cell levels might be promoting T cell exhaustion in BM.

RPs display accumulation of Teff and depletion of Tn populations

We subsequently investigated potential BMME alterations in RPs within <18 months ($n_{participants} = 67$) of initial therapy, compared to those who had not progressed for at least 4 years (NP, $n_{participants} = 83$) (Fig. 1g). Most of these participants received standard triplet therapy, consisting of a PI, IMiD and a steroid as their first line of therapy (Supplementary Table 5). Broadly, RPs had lower abundances of CD4$^+$ T cells and B cells and higher levels of myeloid, plasma and erythroid cells relative to NPs (Fig. 4a). The lower levels of B cells were driven by a large reduction in transitional, immature and naive B cells ($P = 0.003$; Fig. 4b and Extended Data Fig. 5a,b).

To investigate myeloid compartment enrichment ($P = 0.027$) in the RPs, we performed a trajectory analysis that revealed anticipated progression from immature to activated CD14$^+$ monocytes, culminating into mature CD16$^+$ monocytes (Fig. 4c). RPs were significantly enriched for CD14$^+$CD163$^+$ monocytes (Macro/Mono, $P = 0.006$) and depleted of IFN-I-stimulated CD14$^+$ monocytes (CD14$^+$Mono_IFN, $P = 0.026$) (Fig. 4c and Extended Data Fig. 5c). This IFN-I monocyte cluster contains several IFN-I signature markers, which have been previously noted in persons with *TP53* loss (Fig. 3f–i). Differential gene expression analysis (DGEA) of CD14$^+$ monocyte populations identified significant upregulation of proinflammatory markers in RPs, such as *CCL3*, *CCL4*, *IL1B* and *CXCL8*, whereas IFN-I signaling-related genes were increased in NPs (that is, *ISG15*, *IFI6*, *IFI44* and *MX1*) (Fig. 4d). Pathway analysis revealed enrichment of proinflammatory pathways (TNF, interleukin (IL)-10 and chemokine signaling) in RPs, indicating an immunosuppressive phenotype. In contrast, NPs showed enrichment of MHC-II antigen presentation and IFN signaling, consistent with classical antigen processing (Fig. 4e).

The focused analysis on the T cell compartment identified a significantly higher proportion of CD8$^+$ T cells (45.5%) in RPs in comparison to NPs (39.9%) (Fig. 4f; $P = 0.01$). Significant enrichment of CD8$^+$ Tn ($P = 0.015$) and CD8$^+$ GZMK$^+$ Tcm (CD8_Tcm_GZMK, $P = 0.023$) cells was observed in NPs, while RPs exhibited higher abundance of differentiated CD8$^+$ cytotoxic Teff (CD8_Teff, $P = 0.0008$) and HLA$^+$ Teff (CD8_Teff_HLA, $P = 0.001$) populations (Fig. 4f and Extended Data Fig. 5d). Furthermore, DGEA supported this cytotoxic shift of T cells in RPs by identifying a significant upregulation of cytotoxicity markers (*NKG7*, *GNLY*, *PRF1*, *FGFBP2*, *KLRD1*, *GZMB* and *GZMA*). The T cells of NPs demonstrated significant upregulation of genes for early-stage,

Fig. 3 | BMME alterations associated with cytogenetic abnormalities. a, BM immune cell type and subtype abundances comparing HR versus SR participants or stratifying by individual HR abnormalities. Proportions were normalized to the total number of nonmalignant cells per participant. Colors indicate the coefficient of a linear model fitted to logit-transformed proportion adjusting for processing site, with orange and blue indicating cell populations with higher and lower abundances, respectively. Shapes denote two-sided *P* values (circles, not significant; diamonds, $P < 0.05$; squares, $P < 0.01$). **b**, Expression of marker genes representing CD4$^+$ and CD8$^+$ T cell states in participants stratified by composite risk (that is, HR versus SR) or individual cytogenetic risk abnormalities. The colors indicate *z* score normalization, with positive values indicating higher expression levels (red) in participants with the risk event compared to the dataset average, whereas negative values (blue) indicate lower expression levels. **c**, Box plots show per-participant proportions for CD8$^+$ Teff HLA cells as a fraction of total CD8$^+$ cells, stratified by combined Davies risk (HR, $n_{participants} = 123$; SR, $n_{participants} = 108$) or the presence of 1q21 gain ($n_{participants} = 72$), *NSD2* t(4;14) ($n_{participants} = 12$), their combination ($n_{participants} = 18$) or neither ($n_{participants} = 127$). Two-sided *P* values were computed using a linear model on logit-transformed proportions adjusting for site. **d**, Pseudotime trajectory of the CD8$^+$ T cells, with arrows indicating the paths along the trajectory originating at CD8$^+$ Tn cells. The cell types with high and lower proportions in HR as compared to SR are shown with shades of orange and blue colors, respectively. Proportions are shown as log odds ratios relative to total CD8$^+$ T cells. **e**, Putative dysfunctional T cell signature (Supplementary Table 4) enrichment in CD8 Teff HLA$^+$ cells from participants with HR NDMM ($n_{participants} = 123$) as compared to SR ($n_{participants} = 108$). The significance of the difference in signature levels was determined using the Wilcoxon rank-sum test, two-sided. The dashed red line indicates the median dysfunctional signature score for standard-risk patients. **f**, IFN-I response signature levels across major cell compartments, grouped by composite or individual HR abnormalities. Per-participant IFN-I response scores across each compartment are in Extended Data Fig. 4g. **g**, Correlation between IFN-I response signature scores between plasma cells of CD138$^+$ (bulk RNA-seq, GSVA) and CD138$^-$ (pseudobulk scRNA-seq) compartments. Participants with greater than 50 plasma cells in scRNA-seq and matching bulk data were included ($n_{participants} = 108$). Significance of the correlation was calculated using a linear model, adjusting for processing site using a two-sided test. **h**,**i**, IFN-I response signature scores derived from bulk RNA-seq, comparing participants with and without 1q21 copy-number alterations (**h**; normal, $n_{participants} = 408$; gain, $n_{participants} = 213$; Amp, $n_{participants} = 39$) and participants with and without *TP53* loss-of-function mutations (**i**; none, $n_{participants} = 571$; partial, $n_{participants} = 55$; complete, $n_{participants} = 24$). Participants included in the CoMMpass registry with available risk information and CD138$^+$ bulk RNA-seq data were analyzed. The significance of differences in enrichment was evaluated using pairwise two-sided Student's *t*-tests between groups. **j**, Dot plot summarizing differential abundance results across cell populations, including plasma cells. The marker shape indicates two-sided *P* values and color represents the log odds ratios from a linear model fitted to logit-transformed proportions, with positive values denoting enrichment correlated with plasma cell levels. Proportions were computed as a fraction of all cell populations, excluding doublets. Differential abundance was assessed using the plasma cell percentage as both a continuous covariate and a categorical covariate (≥20% versus <20%). **k**–**m**, Scatter plots illustrating the relationship between BM plasma cell percentages, as estimated by flow cytometry before CD138 isolation (*x* axis) and the abundance of CD8$^+$ Teff memory cells (**k**), BM-resident NK cells (**l**) and fibroblasts (**m**). **n**, Comparison of exhaustion-related markers TIGIT and TOX expression across CD8$^+$ T cells between participants with less than (blue; $n = 189$) and greater than (orange; $n_{participants} = 74$) 20% plasma cells. In the box plots, bounds of the box represent the 25th and 75th percentiles, with the center displaying the median. Whiskers extend to 1.5× the interquartile range (IQR) beyond the bounds of the box.

https://doi.org/10.1038/s43018-025-01072-4

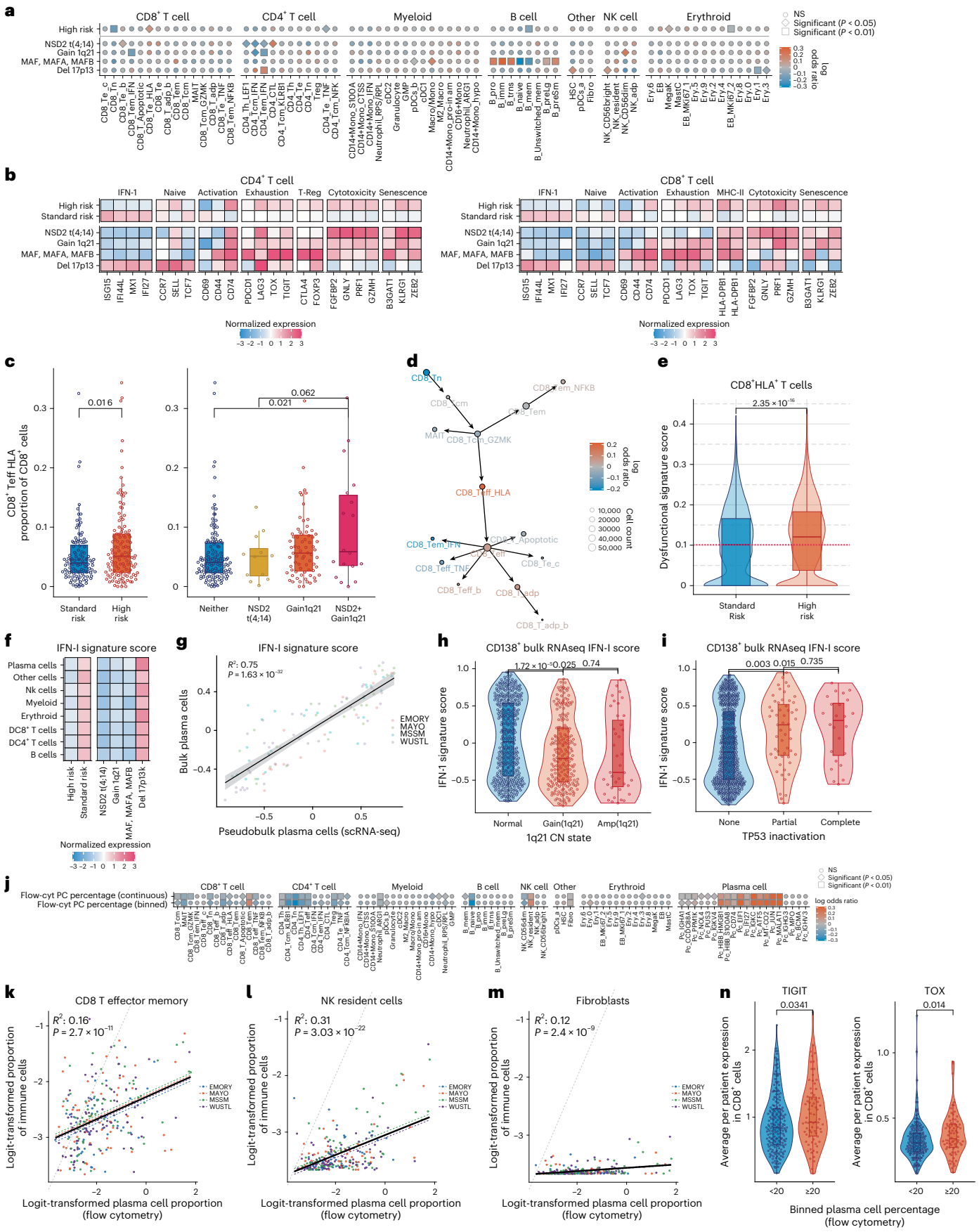

https://doi.org/10.1038/s43018-025-01072-4

Tn populations (*LTB*, *TCF7* and *SELL*) (Fig. 4g). RPs showed enrichment of interleukin and chemokine signaling, while NPs were enriched in ribosomal and translational pathways linked to Tn cells (Fig. 4h). Trajectory analysis of CD8$^+$ cytotoxic lineages revealed higher densities of RP cells at later pseudotime points (that is, CD8_Teff_HLA and CD8_Teff), whereas NPs were enriched at earlier stages (CD8_Tn and CD8_Tcm_GZMK) (Fig. 4i,j). Cytotoxic markers (*NKG7*, *GZMH* and *FGFBP2*) peaked at late pseudotimes, associated with RPs, while Tn markers (*CCR7*, *SELL*, *TCF7*, *CD27* and *CD28*) peaked at early pseudotimes, associated with NPs (Fig. 4k). This suggests the accumulation of terminally differentiated, cytotoxic, CD27$^-$CD28$^-$CD8$^+$ Teff cells in RPs, accompanied by a corresponding reduction in the healthy Tn and Tcm pool necessary for mounting an immunological memory, which might be associated with poor outcomes.

To further explore this hypothesis, we evaluated associations of independent cytotoxic and Tn CD8$^+$ signatures from the pan-cancer T cell atlas[21] to predict outcomes in our myeloma dataset. Elevated T cell cytotoxicity signature was significantly associated with worse PFS ($P = 0.012$) (Fig. 4l and Supplementary Table 4). Conversely, participants enriched in a Tn-like signature across their T cell compartment displayed better PFS ($P = 0.002$) (Fig. 4m and Supplementary Table 4). Exhaustion signature enrichment also showed negative associations with PFS ($P = 0.021$) (Fig. 4n and Supplementary Table 4). However, the expression of exhaustion did not correspond to the RP-enriched CD8_Teff population and seemed to primarily originate from CD8_Tem, CD8_Teff_HLA, CD8_Tem_IFN and CD8_T_adp populations (Extended Data Fig. 4c,d). This is further supported by the significant association of curated putative dysfunctional T cell signature encompassing exhaustion and senescence markers (Supplementary Table 4) with poor survival ($P = 0.011$) (Fig. 4o).

We repeated the above T cell compartment analysis using only samples from participants treated with triplet therapy. While therapy itself cannot impact the baseline immune composition, it can influence outcomes. These analyses showed enrichment of Tn CD8$^+$ cells and B cells in NPs, whereas RPs on triplet therapy were enriched for differentiated T cells, including CD8_Teff and CD8_Teff_HLA (Extended Data Fig. 5e).

RPs with SR profiles showed an accumulation of apoptotic CD8$^+$ T cells and M2 macrophages

Considering the cellular alterations observed across cytogenetic and progression-based groups, we next sought to determine whether immunologic alterations remained associated with RPs even in participants without HR abnormalities. The analysis of SR-RP participants ($n_{\text{participants}} = 19$) compared to SR-NP participants ($n_{\text{participants}} = 40$) exhibited significant enrichment of both CD8_Teff_HLA ($P = 0.008$) and CD8_Teff ($P = 0.018$) populations, along with depletion of CD8$^+$ Tn cells ($P = 0.007$; Fig. 5a). Additionally, these participants also depicted enrichment of M2 macrophages ($P = 0.023$) and depletion of naive B cells ($P = 0.039$) and IFN-stimulated T cell populations ($P < 0.038$) (Fig. 5a).

Because of the observed trends in reduced B cells paired with the enrichment of myeloid cells in RPs (Fig. 4b), we investigated the potential for altered hematopoiesis within the BMME. DGEA on HSCs revealed a shift toward myelopoiesis in the RPs, with overexpression of myeloid lineage commitment markers, while the NPs exhibited an overexpression of lymphoid lineage commitment markers, such as *SOX4* (Fig. 5b).

Cellular communication analysis depicts IFNγ-driven proinflammatory and immunosuppressive changes in participants with poor outcomes

To explore potential BMME signaling changes associated with cytogenetic risk and disease progression, we investigated intercellular communication patterns, revealing several key pathways in outcome-associated subpopulations (Fig. 5c and Supplementary Table 6). MHC-II expression was enriched in antigen-presenting cells (B cells, M2 macrophages and cDCs), associated with NPs (Fig. 4e), pointing toward an improved adaptive immune response in these groups. We also observed increased expression of IFNγ in CD8$^+$ Teff populations (CD8_Teff_TNF, CD8_Teff_HLA and CD8_Tem; Figs. 2f,g and 5c,d), CD4$^+$ cytotoxic populations (CD4_CTL) and cytomegalovirus (CMV) adaptive NK cells (NK_adp). Higher IFNγ receptor expression was also observed in the RP-associated immunosuppressive macrophage cluster (Macro/Mono). Markedly, CD8_Teff_HLA cells were associated with RPs and HR (Figs. 3c and 4f), suggesting that IFNγ signaling in the

Fig. 4 | Single-cell level alterations in the BMME of MM RPs. a, Stacked bar chart of mean per-participant cell type proportions at baseline in RP versus NP participants. Clusters are colored by their major cell type and shaded by individual clusters. The average proportion of major cell types is shown on the graph, normalized as a fraction of all cells, excluding doublets. **b**, Proportions of T, B and myeloid cells per participant by progression groups (RP, $n_{\text{participants}} = 67$; NP, $n_{\text{participants}} = 83$), calculated from total immune cells. Two-sided *P* values were calculated using a linear model adjusting for processing sites. Nonsignificant *P* values > 0.05 are not shown. **c**, CD14$^+$ monocyte trajectory with differential abundance results. Arrows indicate lineage paths from immature Neutrophil_RPS/RPL. Circles represent clusters, with labels adjacent to each center and size representing the number of cells within a cluster. Colors correspond to the log odds ratio for RP and NP participants, computed as a fraction of myeloid cells. **d**, A volcano plot displaying the differentially expressed genes between NP and RP participants in CD14$^+$ monocytes. The *x* axis displays the natural log fold change and the *y* axis displays the $-\log_{10}$ two-sided BH-adjusted *P* value. Significantly differentially expressed genes associated with inflammation and IFN-I response pathways are shown in red and blue, respectively. **e**, A bar plot displaying GSEA for differentially expressed genes shown in **d**. The *x* axis shows the NES, with positive values indicating association with NP-enriched markers and negative values indicating association with RP-enriched markers. Pathways are colored by the sign of the NES and shaded by $-\log_{10}$FDR; those with BH-adjusted *P* values < 0.1 were considered significant. **f**, Box plots displaying the distribution of CD8$^+$ cells (left) and selected significantly enriched T cell subtypes (right) as a fraction of CD3$^+$ T cells. Open circles represent individual participants. The difference in proportions between RPs ($n_{\text{participants}} = 67$) and NPs ($n_{\text{participants}} = 83$) was assessed using a linear model (two-sided *P* value). **g**, A volcano plot displaying the differentially expressed genes between NP and RP participants in CD3$^+$ T cells. The *x* axis displays the natural log fold change and the *y* axis displays the $-\log_{10}$ two-sided BH-adjusted *P* value. Select genes are highlighted and colored on the basis of their associated function. **h**, Bar plot displaying GSEA results for the differentially expressed genes shown in **g**. The *x* axis shows the NES, with positive and negative values indicating association with the NP-enriched and RP-enriched markers, respectively. The pathways are colored by the sign of the NES and shaded by the $-\log_{10}$FDR; those with BH-adjusted *P* values < 0.1 were considered significant. **i**, The trajectory of CD8$^+$ cells along with differential abundance results. Arrows indicate lineage paths from CD8$^+$ Tn cells. Circles represent clusters, with labels shown adjacent to each center and size representing the number of cells within a cluster. The lineage highlighted in red corresponds to the trajectory associated with cytotoxic cells. Colors correspond to the log odds ratio for RP and NP participants, computed as a fraction of all CD8$^+$ T cells. **j**, A density plot showing the distribution of cells by pseudotime along the cytotoxicity lineage, from the original cluster (CD8_Tn, low pseudotime) to differentiated cytotoxic clusters (high pseudotime). **k**, Smoothed normalized expression along the cytotoxicity lineage's pseudotime for five Tn-associated genes (blue) and five cytotoxicity-associated genes (red), weighted by Slingshot's lineage assignment weight. **l**–**o**, Survival plots displaying the relationship between PFS and the participant's average cytotoxicity signature (**l**), Tn signature (**m**), exhaustion signature (**n**) or putative T cell dysfunction signature (**o**) scores across CD3$^+$ T cells. Significance values were determined using two-sided *P* values from a Cox proportional hazards (PH) model. For the survival curves, participants were binned into groups with 'high' (brown) or 'low' (blue) expression, with the cutoff determined using maximally selected rank statistics. In the box plots, the middle bar represents the median, lower and upper hinges correspond to first and third quartiles and upper whiskers extend to the largest value no further than 1.5× the IQR.

https://doi.org/10.1038/s43018-025-01072-4

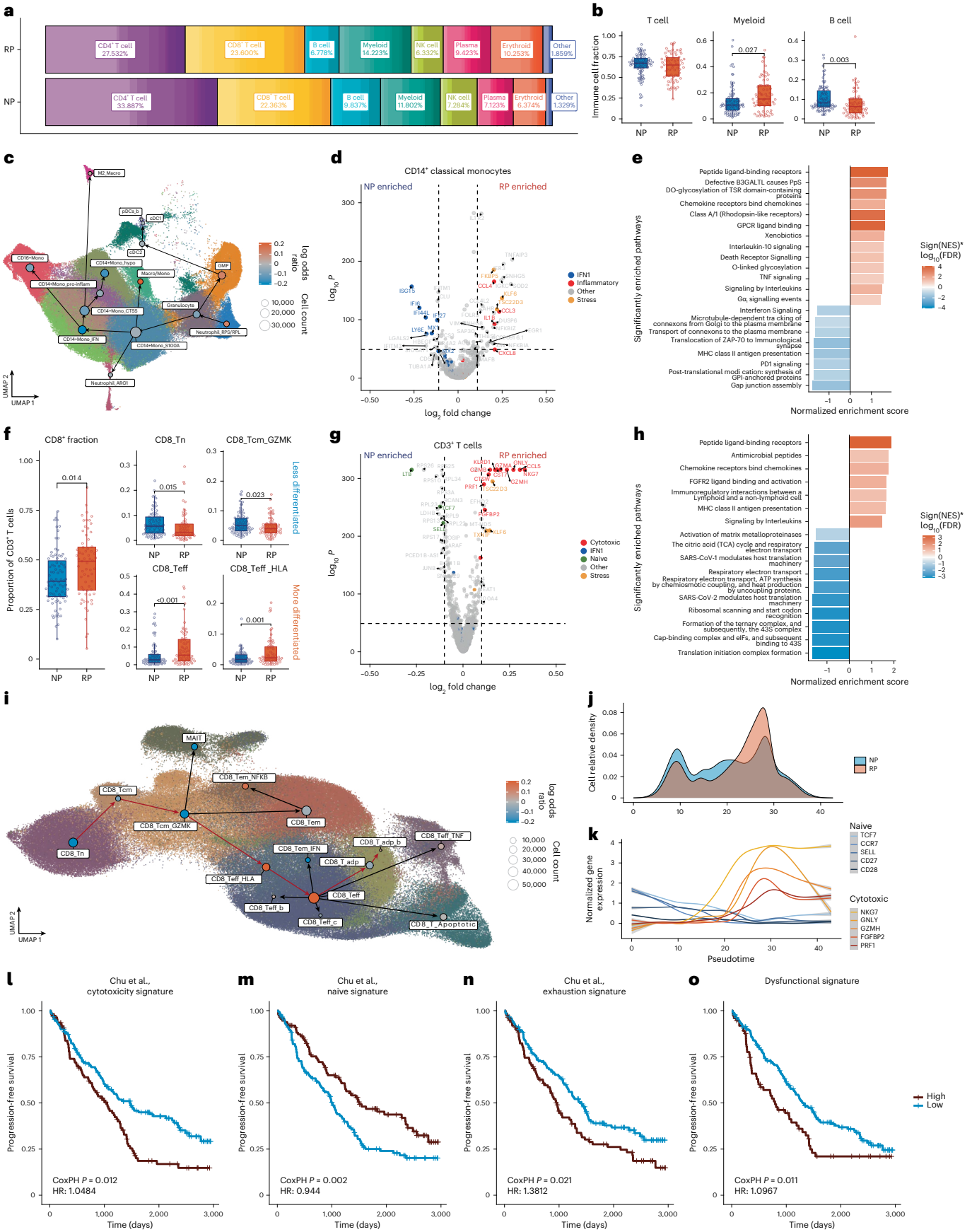

https://doi.org/10.1038/s43018-025-01072-4

BME may contribute to inflammatory alterations in the monocytes of RPs. Notably, the RP-associated cluster (Macro/Mono; Fig. 4c and Extended Data Fig. 5c) was also found to express *BAG6*, an inhibitor of NK-mediated cytotoxicity in its soluble form, and well-documented molecules in MM oncogenesis and progression, thrombospondin-1 (THBS1) and a proliferation-inducing ligand (APRIL). In contrast, the IFN-I-associated monocyte cluster, associated with NP participants (Fig. 4c and Extended Data Fig. 5c), was found to highly express B cell-activating factor (BAFF), an essential promoter of B cell survival and terminal differentiation. Previous studies also reported BAFF expression associated with IFN-I signaling across multiple diseases[22]. BAFF can bind to transmembrane activator and CAML interactor (TACI) expressed on plasma cells, although it has a much higher affinity to BAFF-R expressed on the mature B cell populations.

Given that IFNγ overexpression in the T cell compartment correlates with RPs, we further investigated IFNγ expression in SR participants and its relationship to outcomes. SR-RPs also showed significantly higher average IFNγ expression across their T cell compartment (Fig. 5e), associated with poor outcomes (Fig. 5f). Furthermore, $CD14^+$ monocytes of SR-RPs had significantly higher IFNγ receptor (that is, *IFNGR2*) expression (Fig. 5g), which was also associated with poor outcomes (Fig. 5h). These findings appeared to indicate that heightened IFNγ expression before therapy may be a prognostic indicator of poor outcomes.

In a systems biology analysis, we further investigated gene regulatory networks (GRNs), particularly focusing on myeloid subpopulations associated with HR and disease progression (for example, $CD14^+$ Mono_IFN) and identified enrichment of GRNs for IFN regulatory factor 2 (IRF2), IRF7, IRF9 and signal transducer and activator of transcription 1 (STAT1) transcription factors (TFs) (Fig. 5i–k, Extended Data Fig. 6 and Supplementary Table 7). These TFs are regulated by IFNα and promote the transcription of IFNα-stimulated genes, including *ISG15* (refs. 23,24). Examining the survival association of IRF7 regulon activity within the myeloid compartment, we observed that participants with increased IRF7 regulon activity exhibited better outcomes (Cox proportional hazards (CoxPH) $P = 0.005$; Fig. 5j). Additionally, regulatory networks of cell proliferation related to *E2F1* and *E2F8* TFs were enriched in the granulocyte-monocyte progenitor (GMP) population (Fig. 5i,k), elevated in RPs (Fig. 5a). Increased E2F8 regulon activity was linked with poor survival outcomes within the myeloid compartment, aligning with our previous observation of increased myelopoiesis in RPs (CoxPH $P = 0.034$; Fig. 5j).

Independent validation of BM immune landscape features that are predictive of myeloma outcomes

To independently validate immune microenvironment alterations associated with clinical outcomes, we analyzed an additional 74 samples from participants with NDMM as a validation cohort (Fig. 6a). This effort produced high-quality scRNA-seq data comprising approximately 247,928 cells after integration, clustering and batch correction (Fig. 6b and Extended Data Fig. 7a). The validation cohort identified all major immune cell types of BM, with T cells being the most frequent, followed by B cells, myeloid cells and plasma cells (Fig. 6b,c and Extended Data Fig. 7b–i). Further comparative analysis of cellular abundances between the validation and discovery cohorts revealed striking similarities, reinforcing the robustness and reliability of the validation cohort (Fig. 6d). The validation cohort depicted PFS similar to the discovery cohort, consisting of a nearly equal number of RPs ($n_{participants} = 29$) and NPs ($n_{participants} = 35$) (Fig. 6a). According to the Davies risk definition, the validation cohort contained 34 HR samples, although cytogenetic abnormalities were mostly restricted to gains of 1q21 or *NSD2* (Fig. 6a and Extended Data Fig. 1b,c). In the validation cohort, RPs depicted significant enrichment of $CD8^+$ Teff cells ($P = 0.045$), including $CD8^+HLA^+$ Teff cells ($P = 0.036$; Fig. 6d), and reductions in immature B cells ($P < 0.020$; Fig. 6d), consistent with the discovery cohort. We also observed the enrichment of M2 macrophages ($P = 0.0095$), previously observed in the RPs with SR (Fig. 5a). The enrichment of $CD8^+HLA^+$ Teff cells (CD8_Teff_HLA) also depicted a trend toward poorer OS ($P = 0.07$; Fig. 6e) and PFS ($P = 0.01$; Fig. 6f), supporting discovery cohort results. Further DGEA depicted significant overexpression of cytotoxicity-associated markers and downregulation of Tn markers in the RPs (Fig. 6g). The validation cohort also showed a shift toward cytotoxic $CD8^+$ and Tn cell populations in RPs and NPs, respectively (Fig. 6h). Additionally, the validation cohort also confirmed discovery cohort findings, demonstrating higher T cell cytotoxicity scores ($P = 0.030$, hazard ratio = 1.07; Fig. 6i) and putative dysfunctional scores ($P = 0.028$, hazard ratio = 1.14; Fig. 6j) with poor outcomes. These findings underscore the association of terminally differentiated T cell enrichment with rapid progression of myeloma and poor outcomes.

Integrating baseline immune signatures with cytogenetic risk improves our ability to predict outcomes

To test the hypothesis that immune risk is nonparallel to cytogenetic risk, we aimed to assess the ability of immune clusters or signatures to

Fig. 5 | Pathway and systems biology analysis to decipher mechanisms of poor outcomes in MM. a, Top: differential cell population abundances stratified by composite cytogenetic risk (HR versus SR), progression (RP versus NP) and progression within the subsets of SR participants (SR: RP versus NP) and HR participants (HR: RP versus NP). The color indicates the linear model coefficient fitted to logit-transformed proportions, with orange indicating higher abundance in the first group of each comparison and blue indicating lower abundance. Shapes indicate the two-sided *P* value for the coefficient, with circles representing no significant difference, diamonds representing $P < 0.05$ and squares representing $P < 0.01$. Proportions were computed as a fraction of all immune cells excluding plasma cells, erythroid cells and doublets. Bottom: average normalized scores for select immune signatures (Supplementary Table 4) across the various cell populations. **b**, Bar graph of differentially enriched markers within the $CD34^+$ HSC population. The $\log_2$ fold change values are relative to RPs, with overexpressed genes in orange and downregulated genes in blue. **c**, Heatmap of intercellular communication depicting key patterns of outgoing (top) and incoming (bottom) signaling between cell types. All cell types, including plasma cells, were included, although some populations were combined to simplify the interpretability of the cell communication analysis (Supplementary Table 6). Each row corresponds to a ligand–receptor pair. The heatmaps show relative strength of outgoing signals (top; ligand expression) and the corresponding incoming signals (bottom; receptor expression) by each cell type. **d**, Chord diagram indicating the IFNγ signaling network in all cells. Chords are colored by the 'sender' cell type (ligand) and point toward the 'receiver' cell type (receptor). **e**–**h**, Average expression of IFNγ in T cells (**e**,**f**) and IFNγR2 in $CD14^+$ monocytes (**g**,**h**) and their associations with outcome in SR participants. Box and violin plots (**e**,**g**) compare the per-participant average expression between SR-NP and SR-RP participants, with each dot representing a participant. *P* values were calculated using a two-sided Wilcoxon rank-sum test. In the box plots, the middle bar represents the median, lower and upper hinges correspond to first and third quartiles and upper whiskers extend to the largest value no further than 1.5× the IQR. Kaplan–Meier curves (**f**,**h**) display the association between expression level and PFS, stratified by median expression (high, above the median; low, below the median). Hazard ratios and two-sided *P* values were estimated using CoxPH models. **i**, Heatmap showing normalized average AUC scores for transcriptional regulons on selected myeloid populations. Additional columns display hazard ratios and two-sided *P* values, from CoxPH models fitted on average participant AUC scores categorized into high and low activity using a cutpoint approach. **j**, Survival plots display survival associations between regulon activity in the myeloid compartment and participant outcomes, where high E2F8 regulon expression (bottom) and low IRF7 regulon expression (top) are associated with poor outcomes. The two-sided *P* values from Cox models are shown. **k**, Feature plots of the per-cell AUC values for IRF7 (left) and E2F8 (right) TF regulons across key myeloid populations. Blue indicates low activity (or AUC) and red indicates high activity. The color bar represents the regulon enrichment score.

https://doi.org/10.1038/s43018-025-01072-4

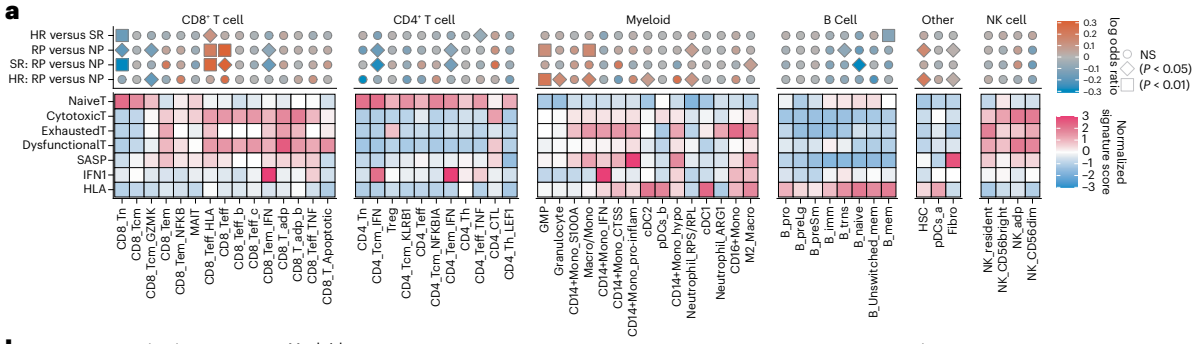

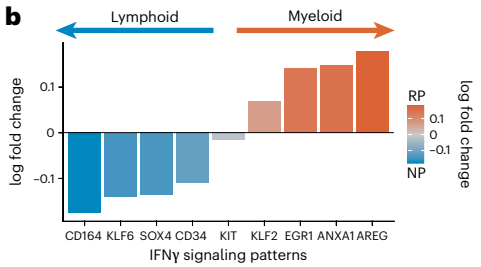

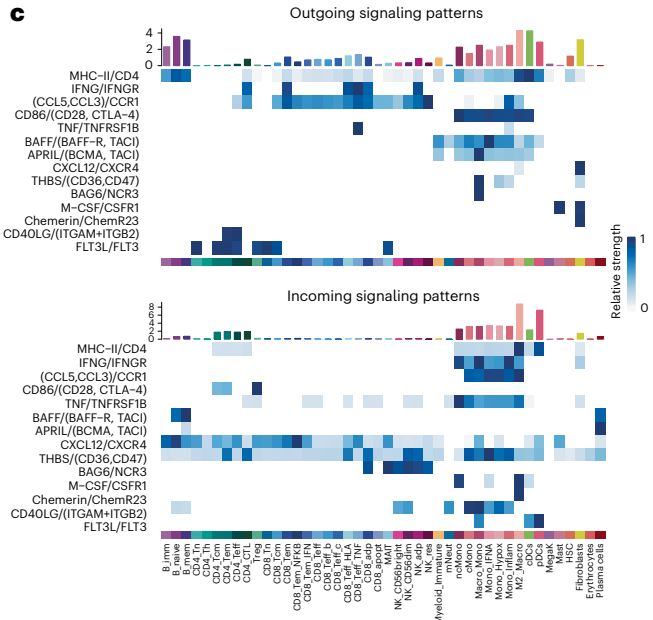

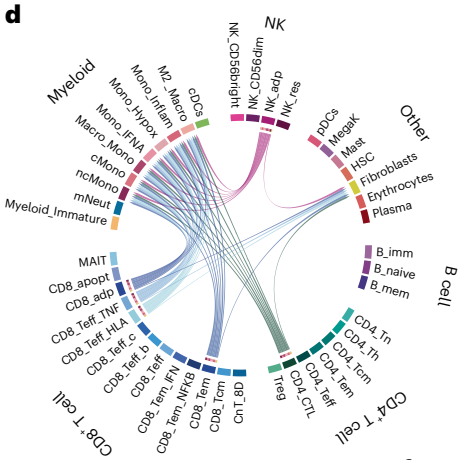

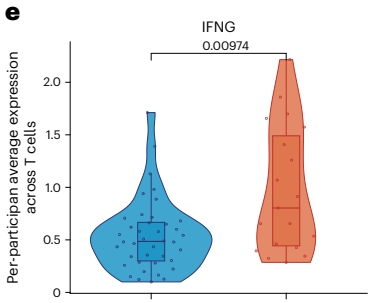

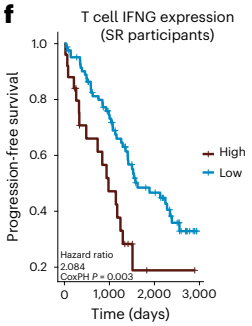

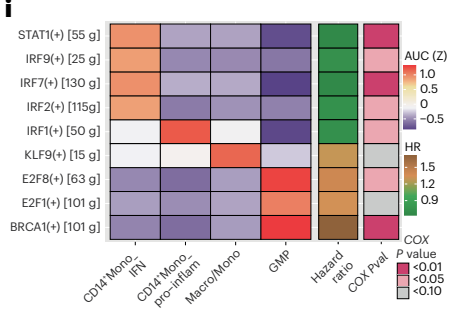

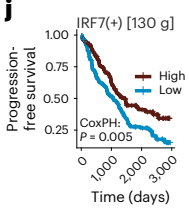

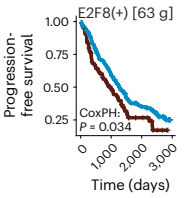

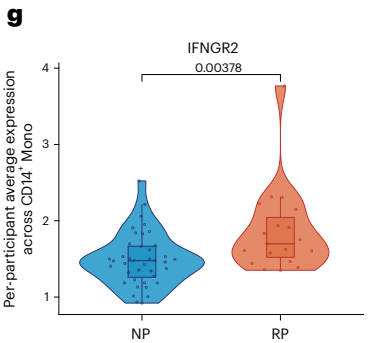

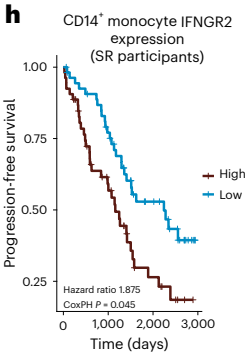

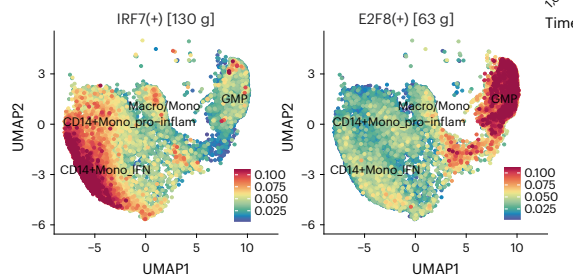

predict disease progression in a univariate and multivariable framework while also including covariates such as age, sex, stage and cytogenetic risk. We used a bootstrapping approach to ensure model robustness and used three different statistical methods (elastic net, logistic regression and Cox models) to validate findings on an independent cohort (Fig. 7a).

Clinical data alone yielded an area under the curve (AUC) value of 0.7 in predicting PFS (Fig. 7b,c). Incorporating cytogenetic risk with clinical variables (stage and demographics) increased the PFS prediction to 0.73 (Fig. 7b,d). Similarly, the predictive power of any single immune subcluster combined with clinical variables only marginally improved prediction (AUC = 0.75; Fig. 7b,e). Iterative feature selection combining subsets of BMME immune clusters with clinical covariates and cytogenetics improved the average AUC for predicting PFS (Fig. 7b,f,g). Specifically, combining Immune Atlas clusters, clinical variables and cytogenetics resulted in AUC values ranging from 0.75 (any given subcluster) to 0.96 (all subclusters), contingent on the number of subclusters considered during modeling (Fig. 7b,g). This substantial increase in AUC by combining clinical and immune features (Extended Data Fig. 8a–c) further highlights the importance of the BMME. Although marginal differences in AUC were observed among individual cell clusters alone, integrative models showcased a notable advantage over simpler models (Extended Data Fig. 8a–c and Supplementary Table 8). Lastly, we identified the most relevant 11 subclusters selected using an elbow test on predictive power versus number of clusters, resulting in a model with high precision and recall (AUC = 0.81; Fig. 7b,f,h). This model for stratifying participants into progressors (Ps) and NPs (Fig. 7b,f,h) included differentiated T cytotoxic populations (CD8_Teff and CD8_Teff_HLA) along with inflammatory myeloid populations ($CD14^+$ Mono_ProInflam) (Fig. 7h).

Next, we investigated the predictive ability of immune cell populations toward OS. Using the same approach as for PFS described above, we identified that OS was predicted at lower true positive rates than PFS (Extended Data Fig. 8d). Furthermore, cytogenetics provided little improvement over models using simple demographics (Extended Data Fig. 8e,f). Yet, integrative models, including immune subclusters, improved the predictions slightly with values around 0.7, although not as strongly as observed for PFS (Extended Data Fig. 8g,h). Consistent with the PFS model, we identified populations significantly associated with OS that included HSCs, T cells and megakaryocytes (Extended Data Fig. 8i).

To further independently validate our finding of immune BM clusters' importance in improving PFS and OS prediction, we investigated our validation cohort of 74 participants with NDMM. The investigation of key clinical variables and cell proportions revealed that ASCT status was a strong confounder of PFS and OS outcomes in the validation cohort. To remove the confounding effects of ASCT, we modeled PFS and OS with and without this confounder to investigate this effect and rule out that our models were biased for validation by not including it in the prediction models for PFS (Fig. 7i and Extended Data Fig. 8j–o) and OS (Extended Data Fig. 8p–t). The PFS prediction model excluding ASCT status achieved an AUC of 0.80 (Fig. 7i and Extended Data Fig. 8n) by incorporating key immune clusters, representing a significant improvement over the combined prediction based on age, ISS and cytogenetics alone[18]. This underscores the synergy and critical role of immune clusters in predicting myeloma progression.

Integrating the minimal ($n_{clusters}$ = 11) immune subset signature from the discovery cohort to our validation cohort exceeded expectations by revealing that the prediction of PFS and OS increased to AUC values of 0.94 (Fig. 7j and Extended Data Fig. 8o) and 0.73 (Extended Data Fig. 8r,t), respectively. These results clearly show the potential biases of clinical covariates and demonstrate that integrative scores using clinical data and genomic and immune cell populations can potentially enhance risk stratification and outcome prediction.

Lastly, to further investigate the robustness of the signature against other proposed cytogenetic risk criteria, we investigated whether immune populations could add to the prognostic capability of the recently proposed International Myeloma Working Group (IMWG) criteria as an alternative to the previously used Davies risk definition[25] (Extended Data Fig. 9a–j and Supplementary Table 1). Top predictive subclusters included many of the same immune populations, including $CD8^+HLA^+$ T cells and $CD8^+$ Teff cells (Extended Data Fig. 9h). Integrating these immune populations with the clinical and cytogenetic variables outlined by the IMWG significantly improved the predictive AUC from 0.73 (Extended Data Fig. 9d) to 0.80 (Extended Data Fig. 9f,i). This finding further highlights the unbiased and critical importance of the immune microenvironment in accurately predicting myeloma progression.

Discussion

In this study, we generated a comprehensive single-cell Immune Atlas of the myeloma BMME by profiling ~1.4 million cells, capturing diverse cell states, including rare subtypes, such as cytotoxic $CD4^+$ T cells, mast cells, HSCs and fibroblasts. This enabled deciphering BMME variations among participants with diverse risk profiles and outcomes; notably, these participants were not treated with recently approved

Fig. 6 | Terminally differentiated and senescent T cells predict poor outcomes in an independent validation cohort of 74 participants. a, Characteristics of the validation cohort. Left: scRNA-seq analysis on $CD138^-$ BM of 74 participants with NDMM yielded 247,928 high-quality cells. Middle: PFS curves comparing the discovery (gray) and validation (red) cohorts. Dashed lines indicate the median survival time for each cohort. The adjacent box plot indicates the number of RPs and NPs in the validation cohort. Right: number of participants from the validation cohort with different HR abnormalities per the Davies risk definition. prob., probability. **b**, UMAP embedding of 247,928 $CD138^-$ BMME cells from the validation cohort (Fig. 2a). Major cell types are shown in consistent colors with the discovery cohort, with shades representing different cell states and subtypes. **c**, Correlation of cellular abundances between discovery and validation cohorts. Points represent individual cell types and subtypes, with colors corresponding to the Kendall correlation coefficient. The shaded region represents the 95% CI. **d**, Top: differential abundance analysis of RPs vs NPs in the validation cohort. Colors indicate the log odds ratio derived from a linear model on logit-transformed proportions, adjusting for the study site, with orange indicating higher abundance in RP and blue indicating lower abundance. Shapes indicate the two-sided *P* value for the coefficient, with circles representing no significant difference, diamonds representing $P < 0.05$ and squares representing $P < 0.01$. Proportions were estimated as a fraction of all immune cells. Bottom: average normalized signature scores for select immune signatures (Supplementary Table 4) across immune populations. **e**,**f**, Survival analysis of $CD8^+$ Teff HLA^+ cell abundance, as a fraction of all $CD8^+$ cells, for OS (**e**; $P = 0.07$, log-rank test) and PFS (**f**; $P = 0.011$, log-rank test). **g**, Volcano plot of the differentially expressed genes across $CD3^+$ T cells in the validation cohort between RPs (right) and NPs (left). The *x* axis shows the batch-corrected $\log_2$ fold change, with positive values corresponding to higher expression in RP participants and negative values corresponding to higher expression in NP participants. The *y* axis shows the $-\log_{10}$ BH-adjusted *P* value based on a two-sided test using a linear model fit to log-normalized expression. Vertical dashed lines mark the $\log_2$ fold change ± 0.1 and the horizontal dashed line marks adjusted $P = 1 \times 10^{-50}$. Certain genes are highlighted on the basis of their functional role (red, cytotoxic or cytolytic; blue, IFN-I; green, Tn cell; yellow, stress). **h**, Pseudotime trajectory of $CD8^+$ T cells, with arrows indicating the paths along the trajectory originating at $CD8^+$ Tn cells. Circles represent clusters and colors indicate the log odds ratio of proportion as a fraction of $CD8^+$ T cells between RP and NP participants, with orange showing higher abundance in RP and blue showing higher abundance in NP. **i**,**j**, Survival plots of PFS associated with the participant's average cytotoxicity signature score (**i**) or average dysfunction signature score (**j**) across all $CD3^+$ T cells. CoxPH models were fit on continuous signature scores, with hazard ratios and two-sided *P* values reported. For the survival curves, participants were binned into groups with high or low expression, with the cutoff determined using maximally selected rank statistics.

https://doi.org/10.1038/s43018-025-01072-4

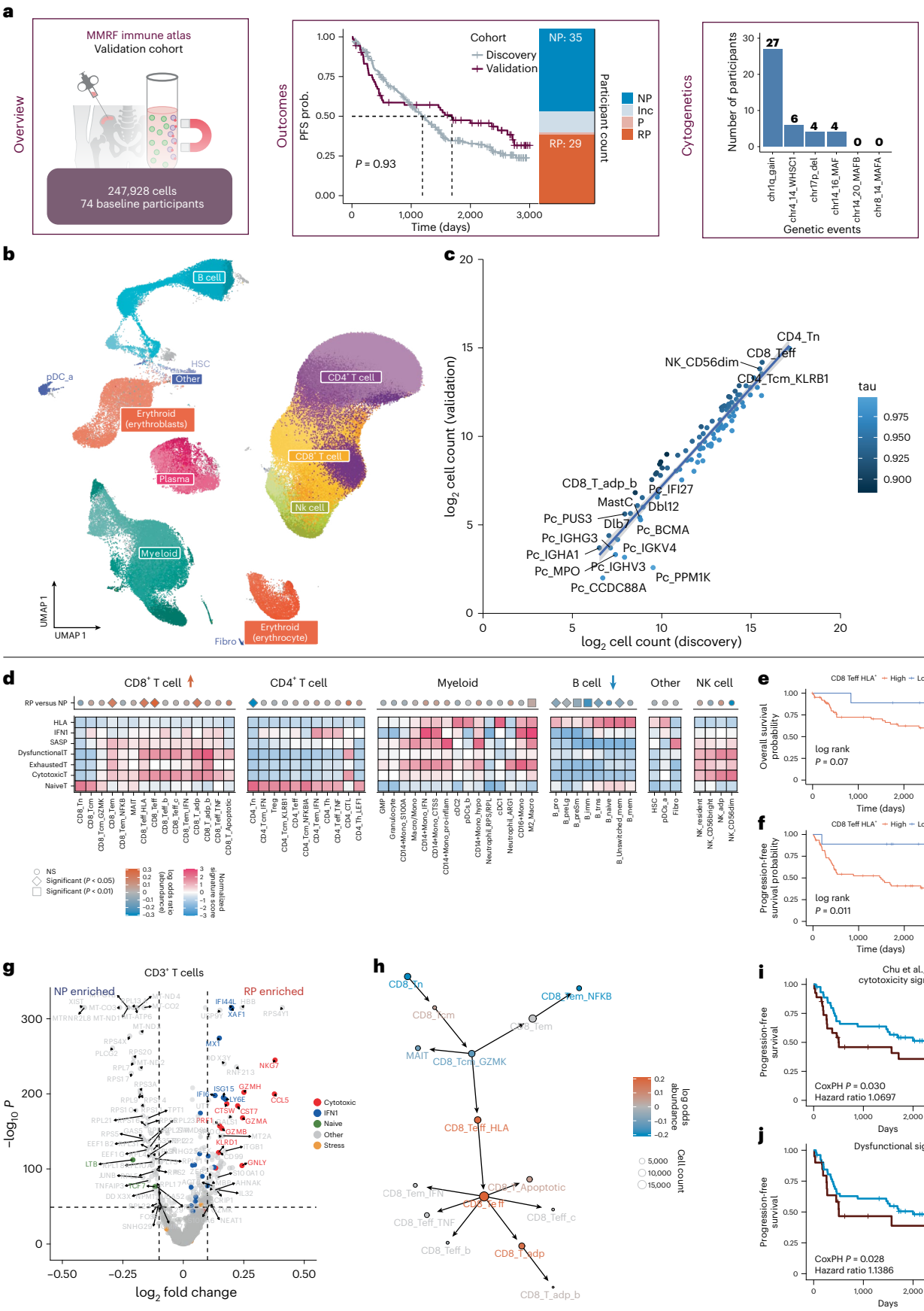

immunotherapies, suggesting that the immune system has a broad, treatment-independent role in myeloma outcomes.

The BMME analysis by stratifying participants on the basis of individual HR abnormalities emphasized the heterogeneous impact of T, myeloid and B cell compartments. Participants with HR abnormalities except 17p13 deletion demonstrated a reduction in IFN-stimulated cell populations and expression. Interestingly, participants with 17p13 deletion had universal elevation of IFN-I-associated genes in T cells, other immune cells and malignant plasma cells. Acute IFN-I stimulation is crucial for mounting an effective antitumor immune response[26] through the activation of pathways such as cGAS–STING[27] but lesions such as 1q21 gain or amplification may block this, enabling immune evasion and progression[28]. Conversely, as IFN-I's apoptotic and senescent effects often depend on p53 (refs. 29,30), del(17p13) may allow tumors to persist despite IFN-I overactivation, with chronic activity potentially impairing T cells[31]. Ultimately, these data underscore the complex interactions between HR cytogenetic alterations and critical antitumor pathways such as IFN-I, emphasizing the need to balance IFN-I signaling for therapeutic benefit. Agents such as bortezomib capable of acutely activating the IFN-I response might synergize with immunotherapies to boost antitumor response in persons with 1q21 gain or *NSD2* abnormalities[32]. Strategies to alleviate immune impairment from chronic IFN-I signaling, such as checkpoint inhibitors targeting exhaustion markers (for example, PD1 and LAG3), could restore T cell function and counteract immune suppression in persons with 17p13 deletion. Kawano et al. already showed that IFNAR1 inhibition results in MM-driven Treg expansion and activation[33], thereby reducing immunosuppressive function and myeloma progression.

The T cell compartment of RPs displayed an accumulation of terminally differentiated CD8$^+$ Teff cells, specifically late-activated cytotoxic cells, with reduced Tn populations (Fig. 7k). This state is sometimes referred to as immunosenescence, with low levels of cytotoxicity, inhibitory *KIR* and *KLRG1* genes and a lack of costimulatory receptors CD27 and CD28, resulting in impaired antigen-mediated proliferation[34–38]. Additionally, studies have indicated that the immunomodulatory effects of drugs such as IMiDs may be through the costimulatory CD28$^+$ pathway[39]; therefore, this population may show a diminished response to standard first-line therapies, potentially leading to poorer outcomes. Depletion of the Tn pool can be driven both by thymic involution[40,41] or by antigenic pressure driven from either myeloma cells or other chronic infections such as CMV or Epstein–Barr virus[42–44]. Impairment of Tn cells reduces the TCR repertoire clonality[38,45], which is typically associated with worse outcomes in various malignancies[46,47]. Additionally, accumulation of these differentiated T cell populations contributes to the inflammatory microenvironment through the production of cytokines such as IFNγ, which we observed highly expressed in the HLADR$^+$CD28$^-$ population associated with both HR and poor outcomes. Unlike exhaustion, it is not well understood whether this senescent state can be reversed, although some studies have indicated that it may be possible[48]. Given that immune therapies could aggravate the T cell imbalance, it may be better to use more targeted therapies, such as bispecific antibodies and CAR-T cells, as the first line of therapy, rather than only in the relapsed setting.

In addition to T cell alterations, RPs displayed a shift toward myelopoiesis in the BM, reflected by general depletion of the B cell compartment, including the BM-native immature populations, compensated for by the enrichment of the myeloid compartment. Myelopoiesis in the BM can be driven by stress or inflammation that drives HSCs to differentiate toward myeloid lineages at a higher frequency[49]. Myeloid cells are also a major source of inflammatory cytokines promoting tumor survival, immunosuppression or angiogenesis, as observed in RPs, displaying enrichment of senescent-associated secretory profile factors, including IL-8, CCL3 or IL-1β[50]. The increased expression of these proinflammatory and immunomodulatory molecules aligns with previous findings, which identified neutrophils as major mediators of cytokine and chemokine signaling promoting the inflammatory BMME in NDMM[51] (Extended Data Fig. 9k). The enrichment of these inflammatory factors may be related to IFNγ produced by the expanded CD8$^+$ Teff cell populations, as the inflamed myeloid cells both express the receptor *IFNGR2* and the TF *IRF1*, which is associated with IFNγ activity[52].

Cell–cell communication analysis identified both BAFF (*TNFSF13B*) and APRIL (*TNFSF13*) expression in the myeloid compartment. BAFF expression was primarily associated with myeloid populations enriched in NPs such as IFN-associated monocytes. BAFF can bind to TACI expressed on plasma cells, although it has a much higher affinity to BAFF-R expressed in mature B cell populations to promote their differentiation and survival. Conversely, APRIL was most strongly associated with the Macro/Mono population enriched in RPs. APRIL is known to bind to TACI (*TNFRSF13B*) on malignant plasma cells, promoting their survival and MM progression[53,54].

Cytogenetics alone demonstrated positive predictive capabilities, yet integrating information from the BMME could enhance

Fig. 7 | Prediction of MM progression by integration of cytogenetic risk along with immune signatures. a, Schematic of variables tested (immune signatures, cytogenetics and clinical variables (covariates)) and the three regression strategies used (elastic net, logistic regression and Cox), followed by bootstrap validation used for model selection. **b**, Receiver operating characteristic curves for progression prediction models based on single clusters, clinical variables and cytogenetics or Immune Atlas variables alone and in combination. Curves are colored by model. The labels indicate subclusters (SubC) and covariates (CoV), including age, batch, site, ISS and cytogenetic. **c**–**e**, Kaplan–Meier curves showing the separation of participants by predicted PFS based on age, ISS stage and batch (**c**), cytogenetics, age, ISS stage and batch (**d**) and Immune Atlas signatures, age, ISS stage and batch (**e**). **f**,**g**, Kaplan–Meier curves showing the separation of participants when cytogenetic risk scores are combined with the best 11 predictive Immune Atlas subclusters (**f**) or with all 83 subclusters (**g**). **h**, Importance of immune subclusters for predicting the progression. The clusters with better and poor MM outcomes are shown with blue and red colors, respectively. The red dashed line marks the *P* value threshold of 0.1 from the ANOVA Wald chi-squared test. **i**, PFS predictive model with 11 predictive immune clusters, excluding ASCT, in the discovery cohort stratifying participants by high versus low risk (AUC = 0.80). **j**, Validation of the PFS predictive model based on 11 immune clusters and clinical covariates (excluding ASCT) on an independent validation cohort of 74 participants with NDMM. The model demonstrates excellent performance in stratifying participants at higher risk of progression from a low-risk category, achieving an AUC of 0.94. All survival curves display the two-sided *P* value from a log-rank test. **k**, Summary of the key cellular subtypes and signaling pathways comprising the MM BMME and their association with participant outcomes. Within the aging BM, a state of chronic inflammation, known as 'inflammaging', results in altered lymphoid and myeloid cell populations, enabling immune escape of malignant plasma cells. Within the T cell compartment, participants with MM showing poor outcomes exhibit a shift toward immunosenescent and late-activated CD8$^+$ T cells, producing type 2 interferon (IFN-II) that drives senescence-associated and immunosuppressive phenotypes in myeloid compartment. In contrast, participants with MM showing better outcomes display highly proliferative Tn and Tcm CD8$^+$ subsets, in addition to enriched Th populations driven by increased MHC-II antigen presentation among myeloid cells. T cell and myeloid populations in these participants appear to be stimulated by IFN-I, in contrast to participants with poor outcomes exhibiting enrichment of IFN-II signaling. This difference in IFN stimulation appears to be linked to participant outcomes, in part, through the differential expression of BAFF by IFN-I-stimulated monocytes and APRIL by IFN-II-stimulated monocytes. Notably, BAFF preferentially binds to mature B cells to promote survival, potentially enhancing B cell-mediated immunity and leading to improved outcomes. Conversely, APRIL has been shown to inhibit memory B cell function and promote malignant plasma cell survival. This dysregulation is further highlighted in the shift from B cell development toward increased myelopoiesis in participants with poor outcomes. **k** was created with BioRender.com.

https://doi.org/10.1038/s43018-025-01072-4

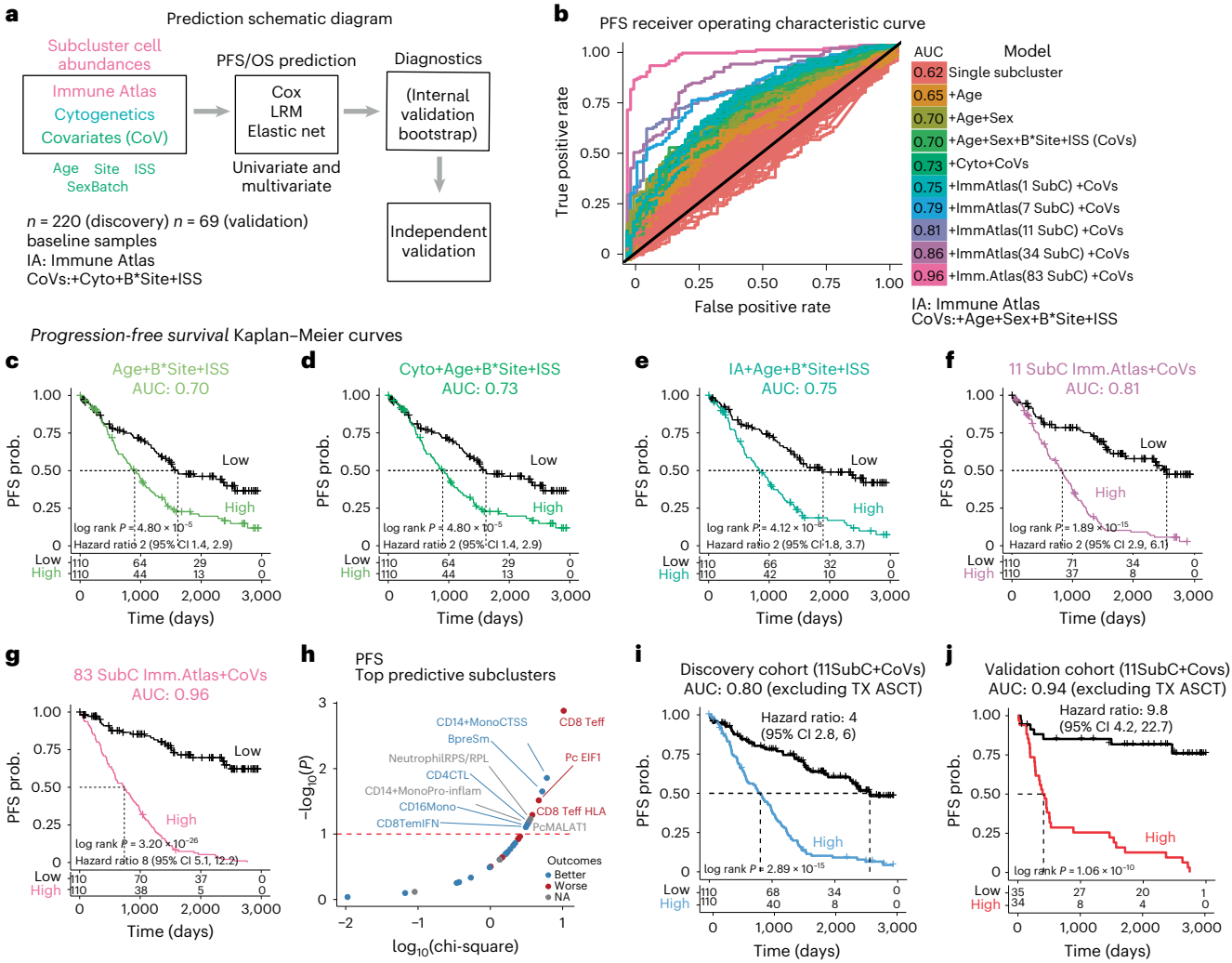

stratification and guide optimal therapeutic selection. We observed that the prevalence of differentiated BMME immune cell populations could predict outcomes with good accuracy in our cohort regardless of cytogenetics. Importantly, combining tumor cytogenetics and immune signatures can significantly improve the accuracy in stratifying myeloma outcomes. Participants with immunosenescent and inflamed BMME might have poor overall or event-free survival even with a favorable genetic makeup. Therefore, we posit that future treatments targeting the immune microenvironment could improve outcomes of myeloma. This observation can elevate the importance of capturing the BMME as a prognostic marker for MM. Increasing the studies capturing such information at the cohort scale could enable us to establish a new generation of comprehensive risk scores or the derivation of simplified lower-cost assays that focus only on the most informative populations. Furthermore, these data may identify ancillary therapeutic targets that improve the efficacy of current treatment strategies and may contribute to rationally designed, personalized treatment regimens based on both the tumor and the immune microenvironment.

This study created an extensive and comprehensive resource to map the granular cellular landscape of myeloma from baseline samples. However, the study had multiple limitations, including only studying gene expression, and did not include any proteomic or functional profiling. Additionally, the study lacked information on T cell repertoire profiling, which is crucial for understanding the expansion of antitumor T cell clones. This expansion is particularly important when analyzing longitudinal samples to ascertain treatment responses rather than relying solely on baseline NDMM samples profiled in this study. Future comparison of the findings herein against age-matched, non-MM biopsies could inform how aging contributes to alterations in the BMME.

This study highlights the importance of the immune landscape in better stratification of persons with myeloma in addition to tumor alterations. This paradigm can enable us to better understand the combinations of factors that influence outcomes in MM and move closer to the goal of optimizing therapy for each individual to ensure the best outcomes.

Methods

Ethics approval and participant consent

All samples for the study were obtained from the MMRF CoMMpass clinical trial (NCT01454297). Procedures involving human participants as part of this trial were performed according to the ethical standards of the MMRF research committee. Written informed consent was obtained from participants for the collection and analysis of samples and clinical information by the MMRF. The institutional review board at each participating medical center approved the study protocol. The list of participating institutes that approved the study protocol is available from ClinicalTrials.gov (NCT01454297).

Experimental model and human subject details

A total of 337 CD138$^-$ MM BM mononuclear cell samples were collected from participants with MM enrolled in the MMRF CoMMpass study (NCT01454297) and profiled in the discovery (n = 263) and validation (n = 74) phases. Participants enrolled in the study were monitored through quarterly checkins for up to 8 years following initial disease diagnosis. All participants were required to be eligible for either standard triplet therapy (IMiD, PI and glucocorticoid) or doublet therapy. Most participants received triplet therapy in their first line of therapy. Participants' information is available in Supplementary Table 3 for the discovery and validation cohorts. Samples were acquired before therapy (baseline) and after therapy (relapse or remission) and then processed at four institutions: Emory University, Mayo Clinic Rochester, Icahn School of Medicine at Mount Sinai and Washington University.

CD138$^-$ cell isolation and cryopreservation of cell samples

BM aspirates from the MM Research Consortium tissue bank were separated into CD138$^+$ (myeloma cells) and CD138$^-$ (immune, BM cells) fractions using immunomagnetic cell selection targeting CD138 surface expression (automated RoboSep and manual EasySep from StemCell Technologies). Before bead-based separation, each sample was assessed for malignant plasma cell levels using flow cytometry. Briefly, the CD138$^-$ cells were centrifuged at 400g for 5 min. The resulting cell pellet was resuspended in freezing medium consisting of 90% fetal calf serum and 10% DMSO at a concentration of 5–30 million cells per ml in multiple aliquots. Cell concentrations and aliquot locations were documented before storing in liquid nitrogen for future studies.

scRNA-seq sample preparation, library construction and sequencing

To generate high-quality and comparable single-cell data, we developed a highly detailed single-cell protocol on the basis of our pilot studies[12,19,20] for implementation across centers and performed profiling using single-cell 3′ profiling (10x Genomics). Briefly for scRNA-seq, aliquots of the CD138$^-$ BMME samples were thawed quickly in 37 °C water bath. Cells were washed with a warm medium and pelleted by spinning at 370g for 5 min at 4 °C. The cell pellet was resuspended in ice-cold PBS with 1% BSA and cell viability was measured. If cell viability was <90%, dead cell removal was performed using the dead cell removal kit (Miltenyi Biotec). The cell pellet was resuspended in 100 µl of dead cell removal microbead solution and incubated at room temperature for 15 min. Magnetic removal of labeled dead cells was performed using the MS column or autoMACS Pro separator. The eluted supernatant containing the live cells was pelleted by centrifugation at 370g for 5 min at 4 °C. Cells were finally resuspended in ice-cold PBS containing 1.0% BSA. To assess for potential batch effects between sequencing runs, a subset of samples were spiked in with approximately 100–150 cells from a murine sarcoma line (NIH/3t3; American Type Culture Collection (ATCC), CRL-1658), as described below. The cells were loaded onto the 10x Genomics Chromium Controller according to the manufacturer's instructions, followed by reverse transcription (RT)–PCR, complementary DNA (cDNA) amplification and library preparation using the Chromium Next-GEM single-cell 3′ GEM, library and gel bead kit version 2.1. Briefly, approximately 8,000 cells were partitioned into nanoliter droplets to achieve single-cell resolution for a maximum of 5,000 individual cells per sample. The resulting cDNA was tagged with a common 16-nt cell barcode and 10-nt unique molecular identifier (UMI) during the RT reaction. Full-length cDNA from poly(A) mRNA transcripts was enzymatically fragmented and size-selected to optimize the cDNA amplicon size (~400 bp) for library construction as per recommendations from 10x Genomics. The concentration of the single-cell library was accurately determined through qPCR (Kapa Biosystems) to produce cluster counts appropriate for the paired-end sequencing using NovaSeq 6000 platforms (Illumina). The sequencing data were generated by targeting 25,000–50,000 reads per cell, which provided gene expression profiles of 1,000–4,000 transcripts per cell.

NIH/3t3 spike-in and filtering for downstream analyses

In some samples, cells from murine sarcoma lines (NIH/3t3; ATCC CRL-1658) were spiked into the final human single-cell suspension to qualitatively assess batch effects across centers. The vial of NIH/3t3 cells was thawed by gentle agitation in a 37 °C water bath. Contents of the vial were transferred to a 1.5-ml sterile tube and spun at approximately 400g for 4 min. The supernatant was discarded; the resulting pellet was washed with 1× PBS and then spun down at the same speed. After discarding PBS, the pellet was resuspended in complete medium, DMEM (ATCC, 30-2002) supplemented with 10% FBS and 1% penicillin–streptomycin. Cell viability was assessed and kept on ice while the participant's sample was prepared. After cells from the participant's

BM aspirate were resuspended, approximately 100–150 NIH/3t3 cells were spiked in, targeting a 1:50 ratio of spike-in to human cells.

To identify the murine sarcoma spike-in cells in the scRNA-seq data, we additionally mapped the raw data to the 2020A combined human (GRCh38) and mouse (mm10) reference genome provided by 10x Genomics using Cell Ranger (version 6.0.1; 10x Genomics) and analyzed the resulting data using Seurat. Clusters in which at least 80% of cells had fewer than 95% of reads mapped to the human reference genome were identified as mm10 spike-in cell lines. These populations were assessed to see whether variance in alignment between processing centers or between subsequent sequencing runs within the same center would result in sample-specific or processing-center-specific populations for the spike-in cell line to determine whether batch correction would be required. Cell barcodes corresponding to NIH/3t3 spike-in cells were removed from the final merged object after alignment to the 10x Genomics 2020A GRCh38 reference genome before calculating highly variable genes or clusters. Two samples with over 65% of cells being identified as NIH/3t3 spike-in cells were excluded from the integrated object and subsequent downstream analyses.

scRNA-seq genome alignment and quality control

For the analysis of scRNA-seq samples, Cell Ranger (version 6.0.1; 10x Genomics) was used for demultiplexing sequence data into FASTQ files, aligning reads to the human genome (GRCh38) and generating gene-by-cell UMI count matrices. Empty droplets were removed using DropletUtils[55] (version 1.14.2) (false discovery rate (FDR) < 0.001). Ambient RNA was removed using CellBender[56] (version 0.3.0) (false positive rate = 0.01). For quality control, cells with <1,000 UMI reads, <200 unique genes or >20% of UMIs mapped to mitochondrial genes were filtered out using Seurat (version 4.3). Harmony[57] (version 0.1) was implemented to mitigate batch effects from processing sites and shipment batches in the resulting cell clusters and embeddings. For a small subset of downstream analyses that directly operate on the count matrix and do not support controlling for a batch covariate, such as CellChat[58] or SCENIC[59], a corrected count matrix was generated as described below.

Batch-corrected count matrices for GRN and cellular communication analysis

Batch effect estimation. First, the Poisson Pearson residuals were computed for each gene across all cells. Genes with zero UMI counts across all cells were excluded from further steps. For the remaining genes, the proportion of variance explained by batch in the Pearson residuals was estimated using the R^2 from a linear regression model. Genes where the batch explained less than 1% of the variance were removed to avoid overcorrection.

Batch-corrected counts. The reference count distribution for each gene affected by batch was modeled as either Poisson (when the mean was equal to the variance) or negative binomial. The Poisson parameter was estimated using the maximum-likelihood estimator, while the negative binomial mean and dispersion parameters were estimated using a gamma Poisson generalized linear model. The batch correction was performed in two steps: (1) scaling and centering the Pearson residuals using the batch-level means and s.d. to account for the differences between batches and (2) transforming the standardized Pearson residuals onto the probability scale using the empirical distribution function and then the batch-corrected counts using the quantile function of the reference Poisson or negative binomial distribution. A pseudocount of 1 and the original zeros observed in the uncorrected UMI counts were restored to preserve the observed sparsity.

Clustering and cell annotation

Following the removal of NIH/3t3 spike-in cells as described previously, raw counts were log-normalized (scale factor = 10,000) using Seurat[60] (version 4.3). The first 25 principal components derived from principal component analysis were computed from the top 3,000 variable genes to reduce data dimensionality. Harmony was applied to these principal components to generate batch-corrected embeddings, where each combination of processing center and shipment batch was considered an independent variable. To cluster cells of similar transcriptome profile, Louvain clustering was performed on the batch-corrected Harmony embeddings using Seurat's 'FindClusters' function. Clusters were visualized using uniform manifold approximation and projection (UMAP). Clusters were aggregated into five major connected components called compartments based on their separability on the UMAP. To annotate these compartments, a combination of SingleR[61] and cell-type-specific or subtype-specific marker expression was used. The identified compartments included 'T/NK' (T cells and NK cells), 'B-Ery' (B cells, $CD34^+$ populations and erythroblasts), 'myeloid' (monocytes, neutrophils and DCs), 'plasma' (plasma cells) and 'Ery' (erythrocytes). A small independent cluster of fibroblasts (946 cells, discovery cohort) was observed in the initial UMAP and was not included in any compartment.

More precise annotation of individual cell compartments was performed separately by repeating the above process on each compartment, leveraging variable genes specific to each compartment. Because of the highly participant-specific nature of myeloma populations, batch correction in the plasma compartment was performed per aliquot instead of per batch. Each cluster was manually annotated on the basis of the expression of canonical markers or top genes of the clusters. While annotating cells, if a possible subset was identified within a given cluster on the basis of marker expression, further subclustering was performed specific to that cluster using the same procedure. Multiple resolutions were assessed, with the final subclustering used being the result that isolated the subpopulation of interest while minimizing the formation of minor or participant-specific clusters.

Validation cohort data processing and cell annotation label transfer

The validation cohort samples ($n = 74$) were processed and quality-controlled using the same procedures applied to the discovery cohort described above. The discovery and validation cohort samples were then merged into a single dataset using Seurat's merge function for batch correction and annotation. Harmony was applied to correct batch effects while preserving shared biological variation. The resulting merged dataset was used for clustering and to derive UMAP embeddings. Subclusters in the validation cohort ($n = 74$) were inferred using the discovery cohort ($n = 263$) as the reference. Label transfer was performed using a k-nearest neighbor (kNN) approach ($k = 1$) on the basis of UMAP embeddings from the merged dataset ($n = 337$). For each cell in the validation cohort, the label of its single nearest neighbor in the discovery cohort was transferred. The FNN package[62] (version 1.1.4) was used to implement the kNN search.

Single-cell mutation mapping and copy-number variation inference

To better understand tumor heterogeneity and malignancy of plasma cell populations, we profiled mutations and copy-number changes of plasma cells. First, we used a mutation mapping strategy to detect mutations within each cell by looking for reads supporting the reference or variant alleles at variant sites in mapped reads from scRNA-seq BAM files. This was achieved by leveraging high-confidence somatic mutations derived from whole-exome sequencing data from the same participant. The code for mutation mapping is available from GitHub (https://github.com/ding-lab/10Xmapping). Furthermore, we used inferCNV (version 0.8.2; https://github.com/broadinstitute/inferCNV) with default parameters to identify sample-level chromosomal copy-number variations of plasma cells, using the immune cells as reference normal set.

Doublet detection

For the discovery cohort, doublets were identified by flagging clusters with high doublet proportions as predicted using DoubletFinder[63], Scrublet[64] (version 0.2.3) and Pegasus (version 1.8.1; https://github.com/lilab-bcb/pegasus). Scrublet was used to detect doublets with the expected doublet rate set at 0.06 and thresholded at 0.2. Doublet-enriched clusters, characterized by at least two methods (FDR < 0.05, Fisher's exact test), were manually reviewed and marked as doublets accordingly. Characteristics considered when reviewing doublet-enriched clusters include the simultaneous, high expression of canonical markers from unrelated lineages (for example, T cell markers *CD3*, *CD8A* and *GZMK* and myeloid markers *LYZ*, *CST3* and *CD14*) or UMI counts disproportionately high relative to similar cell types. A total of 17 cell clusters (n = 74,282) were flagged as doublets and were omitted from downstream differential expression, abundance and trajectory analysis. In the validation cohort, cells mapped to doublet populations were considered doublets and excluded from downstream analysis.

Differential expression among cell types and clinical groups

Differential expression analysis was performed using linear modeling (as implemented in limma[65]) R packages to identify markers enriched in each population, or between clinical groups of interest. Models were adjusted for technical covariates, such as processing site and batch. Significance was determined using moderated t-test statistics on the log-normalized expression. P values were adjusted for multiple comparisons using Benjamini–Hochberg (BH) correction.

Differential abundance of cell types and subtypes

Differential abundance was performed using limma by fitting a linear model to logit-transformed cell proportions across individual participant samples. The distribution of logit-transformed proportions was assumed to be normal but this was not formally tested. Proportions were computed as a fraction of a given set of cell types, as described by the relevant figures. Proportions of nonmalignant cells refer to cell populations other than plasma cells. Proportions of immune cells refer to nonerythroid and nonmalignant plasma populations. All models were adjusted according to the processing site. Significance was determined using a moderated t-test on the logit-transformed proportions. The coefficient of the model represents the log odds ratio between the two groups after adjusting for other confounding features. The logit-transformed proportions were computed using the car package[66] (version 3.1) with default parameters and the difference was considered statistically significant if $P < 0.05$.

Participant stratification based on time interval to disease progression

Participants in the CoMMpass study had regular 3-month checkins in which clinical parameters were evaluated following therapy. The day of disease progression was identified using standard IMWG criteria. Progression data used in this study were derived from the IA22 CoMMpass clinical metadata release. Participants were categorized into discrete progression groups on the basis of their PFS and the duration of time the participant was enrolled in the study. The extreme categories of RP and NP used cutoffs matching those of our pilot study[12]. RPs were those with a progression event within 18 months of therapy (PFS < 18 months). NPs included those who had no progression event for at least 4 years following therapy (PFS > 4 years). Ps were those who had a documented progression event between 18 months and 4 years (PFS > 18 months, PFS < 4 years). Incomplete (Inc) participants were those who exited the study before 4 years of disease diagnosis without experiencing a progression event.

Cytogenetic risk-based stratification of participant samples

The cytogenetic risk categorization was defined using translocation data or copy-number data derived from CD138$^+$ WGS results included in the IA21 CoMMpass metadata release. Thresholds for calling mutation events in the MMRF CoMMpass data are based on the work by Skerget et al.[11] HR participants were defined with one of the six following cytogenetic events: del17p13, t(14;16)[*MAF*], t(8;14)[*MAFA*], t(14;20)[*MAFB*], t(4;14)[*WHSC1/MMSET/NSD2*] and 1q gain. This extends the definition proposed by Skerget et al. by incorporating 1q gain. Participants with none of these six events were considered SR. Participants with partial mutation data, such as having only translocation or only copy-number data, could be classified as HR if an HR mutation was present in the available data; otherwise, these participants were excluded from downstream analyses involving risk-based stratification.

Additionally, we also used the revised HR definition proposed by the International Society of Myeloma (IMS) and IMWG for exploring immune associations. The revised IMS risk definition relies on the presence of one of the following cytogenetics abnormalities: (1) del(17p), with a cutoff of >20% clonal fraction, and/or *TP53* mutation; (2) an IgH translocation including t(4;14), t(14;16) or t(14;20) along with +1q and/or del(1p); or (3) monoallelic del(1p32) along with +1q or biallelic del(1p32)[25] (Supplementary Table 1).

Furthermore, we explored the association of APOBEC-induced mutational score with BM MM immune profile. The enrichment scores were computed using R package maftools[67]. Briefly, the enrichment scores are computed as a ratio between the number of C>T transitions occurring within a TCW motif over all the C>T transitions in a given sample and total background cytosines and TCW motifs within a 20-bp window of mutated bases.

Additionally, we obtained chromothripsis events for participants in this cohort from a prior study by Rustad et al.[68]

Prediction of participant progression based on immune cell abundances, cytogenetics and demographics

To assess the progression prediction capability of the immune signatures alone and in combination with clinical variables, we developed and evaluated multiple classifiers. We evaluated the predictive power of clusters containing cells from at least 50% of samples, resulting in the usage of 83 subclusters. Subsequently, the cell frequencies of these subclusters were used to construct both univariate and multivariate models applying three distinct methods: Cox regression, logistic linear regression (LRM) and elastic net regression. Internal validation using bootstrap was used to test the robustness of the results.

For the elastic net regression models, a sensitivity analysis of the coefficients was performed to facilitate feature selection and the identification of pertinent features. Likewise, features were selected from LRM and Cox models using P-value filtering. Our modeling approach was designed to assess individual or multiple subclusters, integrated with additional variables such as age, sex, disease stage (ISS) and the cytogenetic risk descriptor mentioned earlier.

To ensure the robustness of our models, a bootstrap validation approach was implemented, yielding bias-corrected indices specific to each model type. Model performance metrics, including the Somers index (*Dxy*) and diagnostic statistics were computed using Harrel's rms R package[69]. The R packages, glmnet[70], survival[71] and rms[69] were used for identifying and testing predictions of disease progression. Visualization was carried out using R packages such as ggplot, tidyverse, pheatmap, survminer and gtsummary.

Cell transition trajectory analysis

Pseudotemporal ordering of cells was performed using the Slingshot R package[72]. Cells with a known biological lineage were isolated from all other populations (for example, CD8$^+$ T cells) and doublet and mitochondrial-enriched populations were excluded. New variable features and batch-corrected embedding components were computed as described above. Slingshot was performed on the first 25 batch-corrected harmony embeddings. If an identified progenitor or less-differentiated population was detected through annotation, this

cluster was designated as the 'start cluster' for trajectory analysis. Pseudotimes for clusters, representing the distance along the trajectory from the starting cluster, were calculated using the Slingshot package.

Survival analysis

The participants were categorized on the basis of clinical characteristics and risk groups. To analyze survival outcomes, we calculated the probabilities for either PFS or OS and generated Kaplan–Meier curves using the survival[71] (version 3.2.7) and survminer[73] (version 0.4.9) packages in R. The PFS and OS data were derived from the IA22 CoMMpass clinical metadata release. Participants who left the study before any follow-up appointments or participants with large delays in the start of therapy from the initial baseline visit were excluded from survival analysis. CoxPH models were used to determine the clinical characteristics that had the most significant and independent impact on participant survival. The survival curves based on the CD8 Teff HLA^+ abundance were based on a CoxPH model regressing the OS on the Pearson residuals from a linear regression model with processing site as the covariate. The optimal cutoff to separate the participants at baseline in low-expression and high-expression groups was determined using maximally selected rank statistics implemented in the surv_cutpoint function from the survminer package[73].

Pathway activity analysis and signature scoring

Gene set enrichment analysis (GSEA) was performed to identify the pathways enriched across cell types or clinical groups. The GSEA analysis function gsePathway from ReactomePA[74] (version 1.42.0) was used to compute normalized enrichment scores (NESs) derived from an ordered gene list. Gene lists were ordered by $\log_2$ fold change computed using limma trend, correcting for processing site and batch among cell types or clinical groups, as described above. To evaluate the enrichment of a gene signature in individual cells, we computed a signature score using the AddModuleScore_UCell function from the UCell package[75] (version 2.2.0). A list of genes from each biological signature was provided as an input. Higher scores were given to cells that consistently showed higher expression of genes in the marker list relative to a randomly selected set of background genes. To derive a per-participant signature score, the mean signature score of all cells in the relevant compartment was computed. Wherever necessary, the *P* values were adjusted using the BH approach.

Processing of bulk RNA-seq data to determine IFN signature scores

Bulk RNA-seq data were obtained from the IA22 release from the MMRF CoMMpass Study. The edgeR package[76] (version 4.0.16) was used to normalize raw count data, filtering out genes with fewer than five counts per million (cpm) across all individual samples. The gene set variation analysis (GSVA) package (version 1.50.0) was used to compute per-sample signature scores for the IFN-I signature (Supplementary Table 4), using log cpm values as the input, and a Gaussian kernel density function. A Student's *t*-test using the rstatix package[77] (version 0.7.2) was used to determine whether the difference in IFN-I signature scores across participants with normal 1q21, 1q21 gain or 1q21 amplification or across participants with normal P53 activity, partial loss of P53 or complete loss of P53 was significant.

To determine whether IFN-I patterns identified in $CD138^+$ bulk RNA-seq were consistent with those found in $CD138^-$ sequencing, IFN-I scores in residual plasma cells in the $CD138^-$ scRNA-seq data were compared to the $CD138^+$ bulk RNA-seq data. Counts from baseline participants with at least 50 plasma cells captured in the scRNA data following quality control and doublet filtering were aggregated into pseudobulked count matrices using the pseudobulk expression function in Seurat version 4. Aggregated per-participant count matrices were subsequently filtered in an identical manner to the bulk RNA-seq data and GSVA IFN-I scores were computed.

Cell–cell communication analysis

CellChat[58] (version 2.1.0) was used to identify possible cell–cell interactions across the BMME. The normalized, batch-corrected count matrix described above was used as the input to CellChat. Doublet clusters were excluded from this analysis. For downstream analysis, some clusters representing biologically similar subtypes were aggregated. A table displaying the mapping between the original clusters and their CellChat clusters is provided in Supplementary Table 6.

GRN analysis

The GRNs for selected clusters within our dataset were estimated using pySCENIC, an implementation of SCENIC[59] (single-cell regulatory network inference and clustering). The analysis was focused on selected clusters of interest from the myeloid compartment ($CD14^+$ Mono_IFN, $CD14^+$ Mono pro-inflam, Macro/Mono and GMP). The batch-corrected count matrix served as the input to run GRNBoost2 and generate coexpression modules. GRNs were further inferred using the hg38_refseq-r80 (mc_v10_clust) motif database, hgnc motif annotation (version 9) and pySCENIC's default settings. Because of the stochastic nature of the GRNBoost2 algorithm, slightly varying regulons are detected in each run. Hence, high-confidence regulons were filtered out if they were present in >80% of runs, while their target genes were considered if they were detected in >90% of runs. Using AUCell from pySCENIC, each cell was assigned a gene signature score (AUC) indicating the degree of TF activity. The AUC values were normalized across each regulon and their mean was calculated for each cluster to identify regulons that were strongly associated with a specific cluster. AUC values for each cell in the clusters of interest were averaged to get a per-participant per-regulon score. The cutpoint algorithm was used for grouping samples into 'high' and 'low' regulon activity categories. Survival analysis was performed using the Kaplan–Meier method and CoxPH regression model on the variables 'high' and 'low' activity. As AUC values were derived from batch-corrected count matrices, the shipment batch was not adjusted for in the Cox model.

Statistics and reproducibility

No statistical method was used to predetermine sample sizes. Samples from participants with a baseline time point who were treated with standard doublet or triplet therapy in the CoMMpass study were prioritized for scRNA-seq. Each analysis used all processed scRNA-seq samples available that met our quality control requirements, with the required clinical, cytogenetic or demographic information for each analysis. Two scRNA-seq samples were excluded from all analyses, in which >65% of cells from the sample were identified as mm10 spike-in cells. Samples were from an observational clinical trial and no randomization was performed with regard to therapy. Therapy selection was determined by the physician. For creating scRNA-seq libraries, aliquots were randomly assigned to one of the four processing centers. Investigators were not blinded to allocation during experiments, as participant categorization for subsequent analyses was based on observed features and outcome assessments. Normality of data distribution was not formally tested, although variance stabilization transformations were applied where appropriate for the type of data, as described in the corresponding sections (logit transformation for proportion data in differential abundance and log normalization for expression data in differential expression).

Reporting summary

Further information on research design is available in the Nature Portfolio Reporting Summary linked to this article.

Data availability

All single-cell raw data, processed summary data and clinical information used for this project are under controlled access at MMRF's VLAB shared resource. MMRF requires anyone interested in accessing

the data apply for access at https://mmrfvirtuallab.org and to meet following minimum qualifications: (1) permanent employee of their institution and at a level equivalent to a tenure-track professor or (2) senior investigator that is overseeing laboratory or research program. If the access request is approved, usually within 1 week, investigators will receive an email with instructions to download the data. Alternatively, a Seurat object with limited metadata is available from Zenodo (https://doi.org/10.5281/zenodo.11150168)[78]. Zenodo additionally contains a copy of the *Immune Atlas Cell Annotation Dictionary*, which provides additional information about cluster annotation and marker expression for those who wish to use the preannotated dataset. For all other additional inquiries, please email ImmuneAtlasNetwork@themmrf.org. The data from this study can be explored online at https://myelomaimmuneatlas.themmrf.org/. Source data are provided with this paper.

Code availability

All the code used for data analysis and generation of figures is available on the MMRF Immune Atlas Consortium GitHub (https://github.com/theMMRF/MMRF_ImmuneAtlas). A copy of the Immune Atlas Cell Annotation Dictionary providing additional information about cluster annotation and marker expression will also be provided on the GitHub for those who wish to use the preannotated dataset.

References

1. Padala, S. A. et al. Epidemiology, staging, and management of multiple myeloma. *Med. Sci. (Basel)* **9**, 3 (2021).
2. Mikhael, J., Bhutani, M. & Cole, C. E. Multiple myeloma for the primary care provider: a practical review to promote earlier diagnosis among diverse populations. *Am. J. Med.* **136**, 33–41 (2023).
3. Cancer stat facts: myeloma. *National Cancer Institute Surveillance, Epidemiology, and End Results Program* https://seer.cancer.gov/statfacts/html/mulmy.html (2024).
4. Holstein, S. A. & McCarthy, P. L. Immunomodulatory drugs in multiple myeloma: mechanisms of action and clinical experience. *Drugs* **77**, 505–520 (2017).
5. Avet-Loiseau, H. et al. Genetic abnormalities and survival in multiple myeloma: the experience of the Intergroupe Francophone du Myélome. *Blood* **109**, 3489–3495 (2007).
6. Avet-Loiseau, H. Role of genetics in prognostication in myeloma. *Best Pract. Res. Clin. Haematol.* **20**, 625–635 (2007).
7. Chapman, M. A. et al. Initial genome sequencing and analysis of multiple myeloma. *Nature* **471**, 467–472 (2011).
8. Lohr, J. G. et al. Widespread genetic heterogeneity in multiple myeloma: implications for targeted therapy. *Cancer Cell* **25**, 91–101 (2014).
9. Morgan, G. J., Walker, B. A. & Davies, F. E. The genetic architecture of multiple myeloma. *Nat. Rev. Cancer* **12**, 335–348 (2012).
10. Walker, B. A. et al. A high-risk, double-hit, group of newly diagnosed myeloma identified by genomic analysis. *Leukemia* **33**, 159–170 (2019).
11. Skerget, S. et al. Comprehensive molecular profiling of multiple myeloma identifies refined copy number and expression subtypes. *Nat. Genet.* **56**, 1878–1889 (2024).
12. Pilcher, W. et al. Cross center single-cell RNA sequencing study of the immune microenvironment in rapid progressing multiple myeloma. *npj Genom. Med.* **8**, 3 (2023).
13. Zelle-Rieser, C. et al. T cells in multiple myeloma display features of exhaustion and senescence at the tumor site. *J. Hematol. Oncol.* **9**, 116 (2016).
14. Lopes, R. et al. The immune microenvironment in multiple myeloma: Friend or foe? *Cancers (Basel)* **13**, 625 (2021).
15. Desantis, V. et al. The leading role of the immune microenvironment in multiple myeloma: a new target with a great prognostic and clinical value. *J. Clin. Med.* **11**, 2513 (2022).
16. Kawano, Y. et al. Targeting the bone marrow microenvironment in multiple myeloma. *Immunol. Rev.* **263**, 160–172 (2015).
17. Noonan, K. & Borrello, I. The immune microenvironment of myeloma. *Cancer Microenviron.* **4**, 313–323 (2011).
18. Davies, F. E. et al. Perspectives on the risk-stratified treatment of multiple myeloma. *Blood Cancer Discov.* **3**, 273–284 (2022).
19. Yao, L. et al. Comprehensive characterization of the multiple myeloma immune microenvironment using integrated scRNA-seq, CyTOF, and CITE-seq analysis. *Cancer Res. Commun.* **2**, 1255–1265 (2022).
20. Bhasin, M. Multiple Myeloma Immune Atlas Consortium: gene expression profiling of the bone marrow microenvironment. *protocols.io* https://doi.org/10.17504/protocols.io.q26g718z3gwz/v1 (2024).
21. Zheng, L. et al. Pan-cancer single-cell landscape of tumor-infiltrating T cells. *Science* **374**, abe6474 (2021).
22. Sjöstrand, M. et al. The expression of BAFF is controlled by IRF transcription factors. *J. Immunol.* **196**, 91–96 (2016).
23. Kalvakolanu, D. V. & Borden, E. C. in *Encyclopedia of Cancer* (eds Boffetta, P. & Hainaut, P.) 511–521 (Elsevier, 2002).
24. Yuan, Y. et al. The functional roles of ISG15/ISGylation in cancer. *Molecules* **28**, 1337 (2023).
25. Caffrey, M. Reaching consensus on defining, treating high-risk myeloma. *AJMC* https://www.ajmc.com/view/reaching-consensus-on-defining-treating-high-risk-myeloma (2024).
26. Einhorn, S., Fernberg, J. O., Grandér, D. & Lewensohn, R. Interferon exerts a cytotoxic effect on primary human myeloma cells. *Eur. J. Cancer Clin. Oncol.* **24**, 1505–1510 (1988).
27. Samson, N. & Ablasser, A. The cGAS–STING pathway and cancer. *Nat. Cancer* **3**, 1452–1463 (2022).
28. Neben, K. et al. Administration of bortezomib before and after autologous stem cell transplantation improves outcome in multiple myeloma patients with deletion 17p. *Blood* **119**, 940–948 (2012).
29. Moiseeva, O., Mallette, F. A., Mukhopadhyay, U. K., Moores, A. & Ferbeyre, G. DNA damage signaling and p53-dependent senescence after prolonged β-interferon stimulation. *Mol. Biol. Cell* **17**, 1583–1592 (2006).
30. Porta, C. et al. Interferons α and γ induce p53-dependent and p53-independent apoptosis, respectively. *Oncogene* **24**, 605–615 (2005).
31. Tough, D. F. Modulation of T-cell function by type I interferon. *Immunol. Cell Biol.* **90**, 492–497 (2012).
32. Gulla, A. et al. Bortezomib induces anti-multiple myeloma immune response mediated by cGAS/sting pathway activation, type I interferon secretion, and immunogenic cell death: clinical application. *Blood* **136**, 7–8 (2020).
33. Kawano, Y. et al. Blocking IFNAR1 inhibits multiple myeloma-driven Treg expansion and immunosuppression. *J. Clin. Invest.* **128**, 2487–2499 (2018).
34. Effros, R. B. Loss of CD28 expression on T lymphocytes: a marker of replicative senescence. *Dev. Comp. Immunol.* **21**, 471–478 (1997).
35. Lenschow, D. J., Walunas, T. L. & Bluestone, J. A. Cd28/b7 system of t cell costimulation. *Annu. Rev. Immunol.* **14**, 233–258 (1996).
36. Hintzen, R. Q. et al. Engagement of CD27 with its ligand CD70 provides a second signal for T cell activation. *J. Immunol.* **154**, 2612–2623 (1995).
37. van Baarle, D., Tsegaye, A., Miedema, F. & Akbar, A. Significance of senescence for virus-specific memory T cell responses: rapid ageing during chronic stimulation of the immune system. *Immunol. Lett.* **97**, 19–29 (2005).
38. Lian, J., Yue, Y., Yu, W. & Zhang, Y. Immunosenescence: a key player in cancer development. *J. Hematol. Oncol.* **13**, 151 (2020).
39. LeBlanc, R. et al. Immunomodulatory drug costimulates T cells via the B7-CD28 pathway. *Blood* **103**, 1787–1790 (2004).

40. Palmer, S., Albergante, L., Blackburn, C. C. & Newman, T. J. Thymic involution and rising disease incidence with age. *Proc. Natl Acad. Sci. USA* **115**, 1883–1888 (2018).
41. Thomas, R., Wang, W. & Su, D.-M. Contributions of age-related thymic involution to immunosenescence and inflammaging. *Immun. Ageing* **17**, 2 (2020).
42. McElhaney, J. E. et al. The unmet need in the elderly: how immunosenescence, CMV infection, co-morbidities and frailty are a challenge for the development of more effective influenza vaccines. *Vaccine* **30**, 2060–2067 (2012).
43. Sauce, D. et al. Evidence of premature immune aging in patients thymectomized during early childhood. *J. Clin. Invest.* **119**, 3070–3078 (2009).
44. De Martinis, M., Franceschi, C., Monti, D. & Ginaldi, L. Inflamm-ageing and lifelong antigenic load as major determinants of ageing rate and longevity. *FEBS Lett.* **579**, 2035–2039 (2005).
45. Pawelec, G. Does patient age influence anti-cancer immunity? *Semin. Immunopathol.* **41**, 125–131 (2019).
46. Valpione, S. et al. The T cell receptor repertoire of tumor infiltrating T cells is predictive and prognostic for cancer survival. *Nat. Commun.* **12**, 4098 (2021).
47. Aran, A., Garrigós, L., Curigliano, G., Cortés, J. & Martí, M. Evaluation of the TCR repertoire as a predictive and prognostic biomarker in cancer: diversity or clonality? *Cancers (Basel)* **14**, 1771 (2022).
48. Di Mitri, D. et al. Reversible senescence in human $CD4^+CD45RA^+CD27^-$ memory T cells. *J. Immunol.* **187**, 2093–2100 (2011).
49. Townsend, L. et al. Severe COVID-19 is characterised by inflammation and immature myeloid cells early in disease progression. *Heliyon* **8**, e09230 (2022).
50. Visram, A. & Kourelis, T. V. Aging-associated immune system changes in multiple myeloma: the dark side of the moon. *Cancer Treat. Res. Commun.* **29**, 100494 (2021).
51. de Jong, M. M. E. et al. An IL-1β-driven neutrophil–stromal cell axis fosters a BAFF-rich protumor microenvironment in individuals with multiple myeloma. *Nat. Immunol.* **25**, 820–833 (2024).
52. Ribechini, E. et al. Novel GM-CSF signals via IFN-γR/IRF-1 and AKT/mTOR license monocytes for suppressor function. *Blood Adv.* **1**, 947–960 (2017).
53. Moreaux, J. et al. APRIL and TACI interact with syndecan-1 on the surface of multiple myeloma cells to form an essential survival loop. *Eur. J. Haematol.* **83**, 119–129 (2009).
54. Reijmers, R. M., Spaargaren, M. & Pals, S. T. Heparan sulfate proteoglycans in the control of B cell development and the pathogenesis of multiple myeloma. *FEBS J.* **280**, 2180–2193 (2013).
55. Lun, A. T. L. et al. EmptyDrops: distinguishing cells from empty droplets in droplet-based single-cell RNA sequencing data. *Genome Biol.* **20**, 63 (2019).
56. Fleming, S. J. et al. Unsupervised removal of systematic background noise from droplet-based single-cell experiments using CellBender. *Nat. Methods* **20**, 1323–1335 (2023).
57. Korsunsky, I. et al. Fast, sensitive and accurate integration of single-cell data with Harmony. *Nat. Methods* **16**, 1289–1296 (2019).
58. Jin, S. et al. Inference and analysis of cell–cell communication using CellChat. *Nat. Commun.* **12**, 1088 (2021).
59. Van de Sande, B. et al. A scalable SCENIC workflow for single-cell gene regulatory network analysis. *Nat. Protoc.* **15**, 2247–2276 (2020).
60. Hao, Y. et al. Integrated analysis of multimodal single-cell data. *Cell* **184**, 3573–3587 (2021).
61. Aran, D. et al. Reference-based analysis of lung single-cell sequencing reveals a transitional profibrotic macrophage. *Nat. Immunol.* **20**, 163–172 (2019).
62. Beygelzimer, A. et al. FNN: fast nearest neighbor search algorithms and applications. https://CRAN.R-project.org/package=FNN (2024).
63. McGinnis, C. S., Murrow, L. M. & Gartner, Z. J. DoubletFinder: doublet detection in single-cell RNA sequencing data using artificial nearest neighbors. *Cell Syst.* **8**, 329–337 (2019).
64. Wolock, S. L., Lopez, R. & Klein, A. M. Scrublet: computational identification of cell doublets in single-cell transcriptomic data. *Cell Syst.* **8**, 281–291 (2019).
65. Ritchie, M. E. et al. limma powers differential expression analyses for RNA-sequencing and microarray studies. *Nucleic Acids Res.* **43**, e47 (2015).
66. Fox, J. & Weisberg, S. *An R Companion to Applied Regression* 2nd edn (Sage, 2019).
67. Mayakonda, A., Lin, D.-C., Assenov, Y., Plass, C. & Koeffler, H. P. Maftools: efficient and comprehensive analysis of somatic variants in cancer. *Genome Res.* **28**, 1747–1756 (2018).
68. Rustad, E. H. et al. Revealing the impact of structural variants in multiple myeloma. *Blood Cancer Discov.* **1**, 258–273 (2020).
69. Harrel, F. E., Jr. rms: regression modeling strategies. https://CRAN.R-project.org/package=rms (2024).
70. Tay, J. K., Narasimhan, B. & Hastie, T. Elastic net regularization paths for all generalized linear models. *J. Stat. Softw.* **106**, 1–31 (2023).
71. Therneau, T. & Grambsch, P. *Modeling Survival Data: Extending the Cox Model* (Springer, 2001).
72. Street, K. et al. Slingshot: cell lineage and pseudotime inference for single-cell transcriptomics. *BMC Genomics* **19**, 477 (2018).
73. Kassambara, A., Kosinski, M. & Biecek, P. survminer: drawing survival curves using 'ggplot2'. https://CRAN.R-project.org/package=survminer (2021).
74. Yu, G. & He, Q.-Y. ReactomePA: an R/Bioconductor package for reactome pathway analysis and visualization. *Mol. Biosyst.* **12**, 477–479 (2016).
75. Andreatta, M. & Carmona, S. J. UCell: robust and scalable single-cell gene signature scoring. *Comput. Struct. Biotechnol. J.* **19**, 3796–3798 (2021).
76. Robinson, M. D., McCarthy, D. J. & Smyth, G. K. edgeR: a Bioconductor package for differential expression analysis of digital gene expression data. *Bioinformatics* **26**, 139–140 (2010).
77. Kassambara, A. rstatix: pipe-friendly framework for basic statistical tests. https://CRAN.R-project.org/package=rstatix (2023).
78. Pilcher, W. A single-cell atlas characterizes dysregulation of the bone marrow immune microenvironment associated with outcomes in multiple myeloma. *Zenodo* https://doi.org/10.5281/zenodo.11150168 (2025).

Acknowledgements

We would like to acknowledge funding support from the MMRF (M. Bhasin, S.G., S.N., D.A. and I.S.V.), Myeloma Solutions Fund (M. Bhasin, D.O., M.E.M. and W.C.P.), National Institutes of Health grants U24CA224319 (S.G.), U01DK124165 (S.G.) and P30CA196521 (S.G.), the MMRF fellowship program (D.K.), National Cancer Institute (NCI) grant R50CA211466 (M.P.R.), the Paula C. and Rodger O. Riney Blood Cancer Research Fund (J.F.D., R.V. and L.D.) and NCI grants R35CA210084 (J.F.D.), 5K12CA090628 (T.K.), U24CA211006 (L.D.), U2CCA233303 (L.D.), PJ000021702 (L.D.) and R01CA258776 (I.S.V.). Data analyses were performed on the Ithaca high-performance computing cluster (HPC), Spatial Technologies Unit/Precision RNA Medicine Core (RRID:SCR_024905) and the Harvard Medical School O2 HPC cluster. This work was supported in part through

the computational and data resources and staff expertise provided by Scientific Computing and Data at the Icahn School of Medicine at Mount Sinai and supported by the Clinical and Translational Science Award grant UL1TR004419 from the National Center for Advancing Translational Sciences.

Author contributions

Study design, W.C.P., E.G.-K., C.R.A., M.H., S.T.O., M.P.R., I.A.C., Z.C., S.L., S.S.B., R.V., G.M., L.D., S.G. and M. Bhasin. Data analysis, W.C.P., L.Y., E.G.-K., Y.P.J., D.K., M.E.M., S.N., S.S., J.S., D.D.S., D.O., K.E.F., M.A.F., J.V.D.S., I.C., I.F., Y.L., I.A.C., Z.C., A.L., S.K.-S., S.S.B., S.G. and M. Bhasin. Cell annotation, W.C.P., L.Y., E.G.-K., Y.P.J., D.K., C.R.A., M.E.M., S.S., Y.M., A.C., I.A.C., S.L., S.S.B. and M. Bhasin. Domain expertise, W.C.P., E.G.-K., Y.P.J., D.K., C.R.A., M.E.M., M.H., S.S., J.S., G.C., M. Bakhtiari, N.P., I.S., R.A., E.L., B.E.T., A.C., M.P.R., Y.L., S.D., I.A.C., Z.C., A.L., J.R., S.K.-S., S.L., S.K., S.S.B., T.K., D.A., H.J.C., G.M., L.D., S.G., I.S.V. and M. Bhasin. Clinical expertise, E.L., M.A.F., I.C., M.S., I.A.C., M.V.D., S.K., T.K. and D.A. Experiments, Y.S., K.S., M. Bakhtiari, R.A., K.N., R.C., B.E.T., J.F., E.A., M.A.S., V.A.S., I.A.C., A.H.R., S.L., E.R. and M. Bhasin. Data interpretation, W.C.P., L.Y., E.G.-K., Y.P.J., D.K., C.R.A., M.E.M., M.H., S.N., Y.S., J.T.W., S.S., R.G.J., J.A.F., A.C., I.C., Y.L., S.D., D.O., K.E.F., I.A.C., Z.C., A.L., S.K.-S., S.S.B., S.G. and M. Bhasin. Writing, W.C.P., L.Y., E.G.-K., Y.P.J., D.K., C.R.A., M.E.M., M.H., S.N., S.S., M. Bakhtiari, E.A., Y.L., S.D., M.A.S., V.A.S., D.O., K.E.F., I.A.C., S.L., S.K., S.S.B., T.K., G.M. and M. Bhasin. Supervision, E.G.-K., C.R.A., M.H., I.A.C., Z.C., A.L., J.F.D., S.K.-S., S.L., S.K., S.S.B., R.V., D.A., G.M., L.D., S.G., I.S.V. and M. Bhasin. M.E.M., M.H., S.N., Y.Z., K.S., J.T.W. and S.S. contributed equally as co-second authors.

Competing interests

S.G. reports other research funding from Boehringer-Ingelheim, Bristol-Myers Squibb, Celgene, Genentech, Regeneron and Takeda and consulting from Taiho Pharmaceuticals, not related to this study. J.F.D. is on the consulting or advisory committee for Rivervest, Bioline, Amphivena, Bluebird, Celegene, Incyte, NeoImmuneTech and Macrogenics and has ownership investment in Magenta and Wugen. J.R. declares consulting with Attivare, Parexel, Clario/Bioclinica, Imaging Endpoint and Wolters Kluwer Health, serves on a data and safety monitoring board with Karyopharm and has received grants and nonfinancial support from Celgene, BMS and Sanofi. J.R. also has a patent (PCT/US2021059199) pending. S.K. declares research funding for clinical trials to the institution from Abbvie, Amgen, Allogene, BMS, Carsgen, GSK, Janssen, Roche-Genentech, Takeda and Regeneron, as well as consulting or advisory board participation (with no personal payments) for Abbvie, BMS, Janssen, Roche-Genentech, Takeda, Pfizer, Loxo Oncology, K36, Sanofi, ArcellX and Beigene. T.K. declares research funding from Novartis and Pfizer, as well as advisory board participation for BMS. D.A. declares grants from MMRF, CTN (National Heart, Lung and Blood Institute), Celgene, Pharmacyclics and Kite Pharma, as well as other support from Juno, Partners TX, Karyopharm, BMS, Aviv MedTech, Takeda, Legend Bio Tech, Chugai, Caribou Biosciences, Janssen, Parexel, Sanofi and Kowa. D.A. also has a patent (PCT/US2021/059199) pending. I.S.V. reports grants from NCI, National Heart, Lung, and Blood Institute, National Institute of Diabetes and Digestive and Kidney Diseases, Harvard Stem Cell Institute and consulting for Mosaic, AlphaSights, NextRNA and Guidepoint Global outside of the submitted work. J.A.F. is a consultant for Cancer Prevention and Research Institute of Texas and Wugen on work unrelated to the manuscript. Unrelated to this work, J.A.F. has a monoclonal antibody licensed to EMD Millipore and is an inventor on patent or patent applications (WO 2019/152387 and US 63/018,108) licensed to Kiadis and held or submitted by Nationwide Children's Hospital on transforming growth factor-β-resistant, expanded NK cells. The other authors declare no competing interests.

Additional information

Extended data is available for this paper at https://doi.org/10.1038/s43018-025-01072-4.

Supplementary information The online version contains supplementary material available at https://doi.org/10.1038/s43018-025-01072-4.

Correspondence and requests for materials should be addressed to George Mulligan, Li Ding, Sacha Gnjatic, Ioannis S. Vlachos or Manoj Bhasin.

Peer review information *Nature Cancer* thanks Leng Han and the other, anonymous, reviewer(s) for their contribution to the peer review of this work.

William C. Pilcher[1,24], Lijun Yao[2,24], Edgar Gonzalez-Kozlova[3,24], Yered Pita-Juarez[4,5,6,24], Dimitra Karagkouni[4,5,6,24], Chaitanya R. Acharya[7,24], Marina E. Michaud[8], Mark Hamilton[7], Shivani Nanda[4,5,6], Yizhe Song[2], Kazuhito Sato[2], Julia T. Wang[2], Sarthak Satpathy[9], Yuling Ma[4,5,6], Jessica Schulman[7], Darwin D'Souza[3], Reyka G. Jayasinghe[2], Denis Ohlstrom[1], Katherine E. Ferguson[10], Giulia Cheloni[4,5], Mojtaba Bakhtiari[8], Nick Pabustan[7], Kai Nie[3], Jennifer A. Foltz[2], Isabella Saldarriaga[4], Rania Alaaeldin[8], Eva Lepisto[7], Rachel Chen[3], Mark A. Fiala[11], Beena E. Thomas[8], April Cook[7], Junia Vieira Dos Santos[12], Chiang I-ling[2], Igor Figueiredo[3], Julie Fortier[11], Michael Slade[11], Stephen T. Oh[13,14,15], Michael P. Rettig[16], Emilie Anderson[17], Ying Li[17], Surendra Dasari[17], Michael A. Strausbauch[17], Vernadette A. Simon[17], Immune Atlas Consortium*, Emir Radkevich[3], Adeeb H. Rahman[3], Zhihong Chen[3],

https://doi.org/10.1038/s43018-025-01072-4

Alessandro Lagana[12], John F. DiPersio[2], Jacalyn Rosenblatt[4,5,18], Seunghee Kim-Schulze[3], Sagar Lonial[8,19], Shaji Kumar[16], Swati S. Bhasin[8], Taxiarchis Kourelis[17], Madhav V. Dhodapkar[20,21], Ravi Vij[11,22], David Avigan[4,5,18], Hearn J. Cho[3,7], George Mulligan[7,25] ✉, Li Ding[2,22,25] ✉, Sacha Gnjatic[3,25] ✉, Ioannis S. Vlachos[4,5,6,18,23,25] ✉ & Manoj Bhasin[1,8,9,19,25] ✉

[1]Coultier Department of Biomedical Engineering, Georgia Institute of Technology, Atlanta, GA, USA. [2]Department of Medicine, Washington University in St. Louis, St. Louis, MO, USA. [3]Tisch Cancer Institute, Department of Immunology and Immunotherapy, Icahn School of Medicine at Mount Sinai, New York, NY, USA. [4]Beth Israel Deaconess Medical Center, Boston, MA, USA. [5]Harvard Medical School, Boston, MA, USA. [6]Broad Institute of MIT and Harvard, Cambridge, MA, USA. [7]MMRF, Norwalk, CT, USA. [8]Department of Pediatrics, Emory School of Medicine, Atlanta, GA, USA. [9]Department of Biomedical Informatics, Emory School of Medicine, Atlanta, GA, USA. [10]School of Biological Sciences, Georgia Institute of Technology, Atlanta, GA, USA. [11]Bone Marrow Transplantation & Leukemia Section, Division of Oncology, Washington University School of Medicine, St. Louis, MO, USA. [12]Tisch Cancer Institute, Department of Oncological Sciences, Icahn School of Medicine at Mount Sinai, New York, NY, USA. [13]Division of Hematology, Department of Medicine, Washington University School of Medicine, St. Louis, MO, USA. [14]Department of Pathology and Immunology, Washington University School of Medicine, St. Louis, MO, USA. [15]Immunomonitoring Laboratory, Center for Human Immunology and Immunotherapy Programs, Washington University School of Medicine, St. Louis, MO, USA. [16]Division of Oncology, Washington University School of Medicine, St. Louis, MO, USA. [17]Mayo Clinic, Rochester, MN, USA. [18]Cancer Center and Cancer Research Institute, Beth Israel Deaconess Medical Center, Boston, MA, USA. [19]Aflac Cancer and Blood Disorders Center, Children's Healthcare of Atlanta, Atlanta, GA, USA. [20]Department of Hematology Oncology, Emory School of Medicine, Atlanta, GA, USA. [21]Winship Cancer Institute, Emory School of Medicine, Atlanta, GA, USA. [22]Siteman Cancer Center, Washington University in St. Louis, St. Louis, MO, USA. [23]Spatial Technologies Unit, Harvard Medical School Initiative for RNA Medicine, Boston, MA, USA. [24]These authors contributed equally: William C. Pilcher, Lijun Yao, Edgar Gonzalez-Kozlova, Yered Pita-Juarez, Dimitra Karagkouni, Chaitanya R. Acharya. [25]These authors jointly supervised this work: George Mulligan, Li Ding, Sacha Gnjatic, Ioannis S. Vlachos, Manoj Bhasin. *A list of authors and their affiliations appears at the end of the paper. ✉e-mail: mulligang@themmrf.org; lding@genome.wustl.edu; sacha.gnjatic@mssm.edu; ivlachos@bidmc.harvard.edu; manoj.bhasin@emory.edu

Immune Atlas Consortium

William C. Pilcher[1,24], Lijun Yao[2,24], Edgar Gonzalez-Kozlova[3,24], Yered Pita-Juarez[4,5,6,24], Dimitra Karagkouni[4,5,6,24], Chaitanya R. Acharya[7,24], Marina E. Michaud[8], Mark Hamilton[7], Shivani Nanda[4,5,6], Yizhe Song[2], Kazuhito Sato[2], Julia T. Wang[2], Sarthak Satpathy[9], Yuling Ma[4,5,6], Jessica Schulman[7], Darwin D'Souza[3], Reyka G. Jayasinghe[2], Denis Ohlstrom[1], Katherine E. Ferguson[10], Giulia Cheloni[4,5], Mojtaba Bakhtiari[8], Nick Pabustan[7], Kai Nie[3], Jennifer A. Foltz[2], Isabella Saldarriaga[4], Rania Alaaeldin[8], Eva Lepisto[7], Rachel Chen[3], Mark A. Fiala[11], Beena E. Thomas[8], April Cook[7], Junia Vieira Dos Santos[12], I-ling Chiang[2], Igor Figueiredo[3], Julie Fortier[11], Michael Slade[11], Stephen T. Oh[13,14,15], Michael P. Rettig[16], Emilie Anderson[17], Ying Li[17], Surendra Dasari[17], Michael A. Strausbauch[17], Vernadette A. Simon[17], Nikolaos Kalavros[4,5,6], Jennifer Rogers[7], Travis Dawson[3], Brian H. Lee[3], Geoffrey Kelly[3], Laura Walker[3], Nicolas F. Fernandez[3], John Leech[3], Jarod Morgenroth-Rebin[3], Krista Angeliadis[3], Matthew A. Wyczalkowski[2], Song Cao[2], Omar Ibrahim[2], Roderick Lin[2], Todd A. Fehniger[2], Andrew Houston[16], Emir Radkevich[3], Adeeb H. Rahman[3], Zhihong Chen[3], Alessandro Lagana[12], John F. DiPersio[2], Jacalyn Rosenblatt[4,5,18], Seunghee Kim-Schulze[3], Sagar Lonial[8,19], Shaji Kumar[16], Swati S. Bhasin[8], Taxiarchis Kourelis[17], Madhav V. Dhodapkar[20,21], Ravi Vij[11,22], David Avigan[4,5,18], Hearn J. Cho[3,7], George Mulligan[7,25], Li Ding[2,22,25], Sacha Gnjatic[3,25], Ioannis S. Vlachos[4,5,6,18,23,25] & Manoj Bhasin[1,8,9,19,25]

https://doi.org/10.1038/s43018-025-01072-4

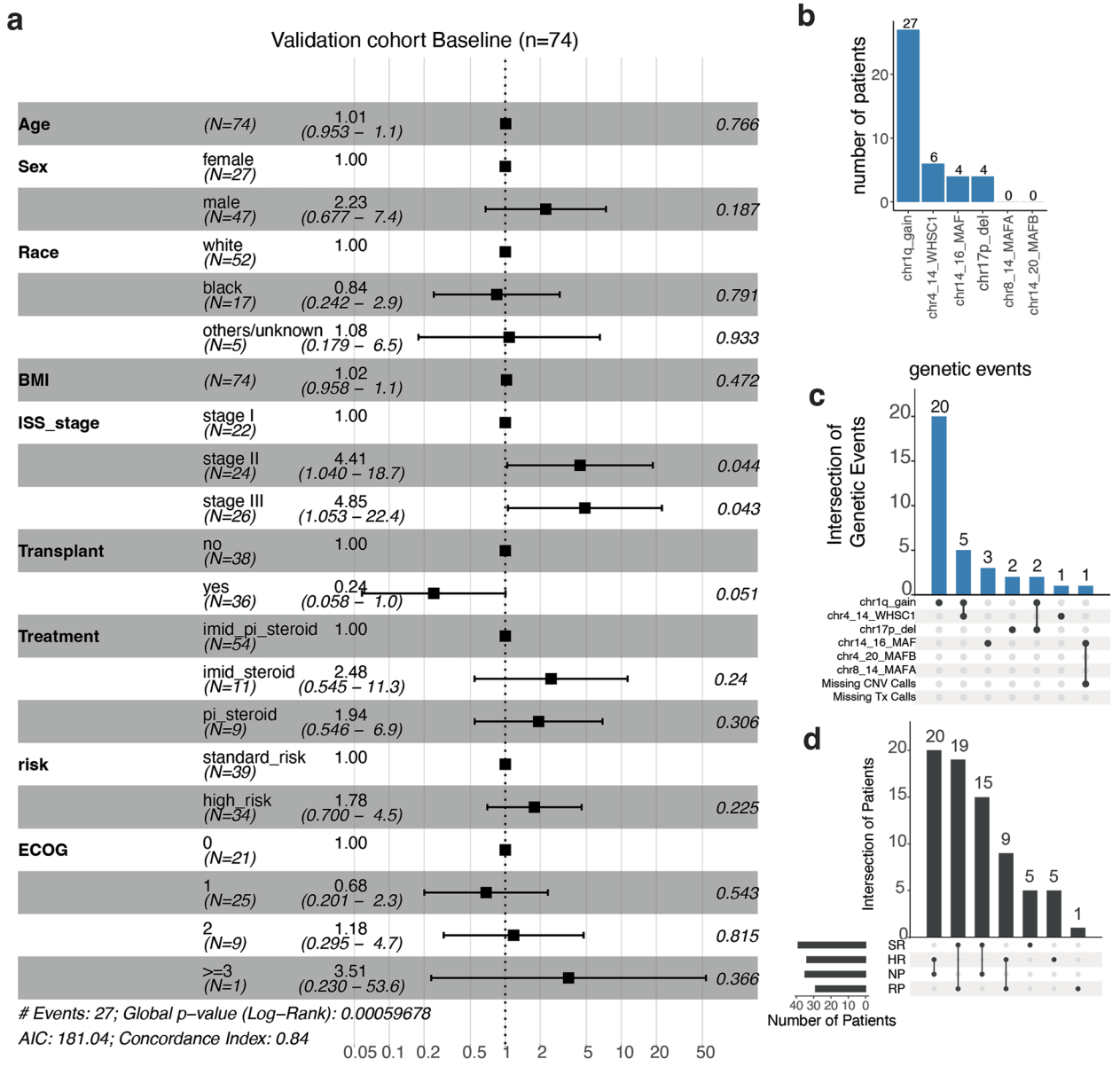

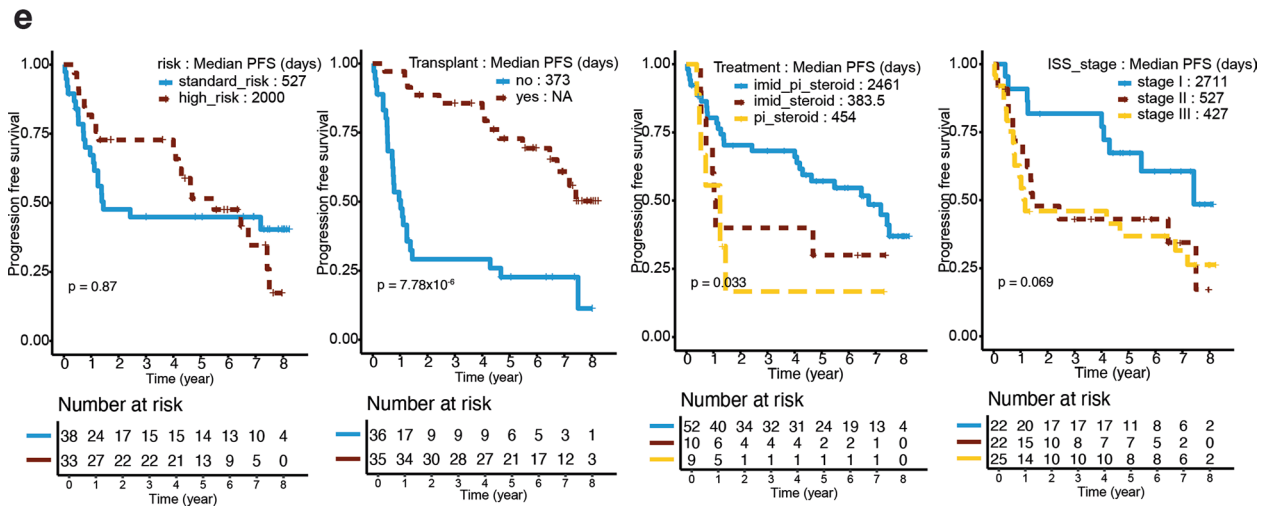

Extended Data Fig. 1 | See next page for caption.

https://doi.org/10.1038/s43018-025-01072-4

Extended Data Fig. 1 | Overview of clinical characteristics of the validation cohort of 74 NDMM patients. (**a**) Summary of clinical characteristics. The forest plot illustrates the effect of various clinical features on progression-free survival (PFS). Error bars display a 95% confidence interval. (**b**) Bar chart showing the total number of patients with each of the six cytogenetic events used for risk stratification. (**c**) UpSet plot showing the distribution and overlap of the major cytogenetic abnormalities comprising the Davies-based high-risk myeloma definition between patients. (**d**) UpSet plot showing the intersection of patients categorized as standard-risk (SR) or high-risk (HR) and non-progressor (NP) or rapid progressor (RP). (**e**) Kaplan-Meier curves depict survival outcomes for patients categorized based on risk stratification (HR vs SR), transplant as a frontline treatment, treatment type, and ISS staging. Two-sided p-values from a log-rank test are displayed. Patients lacking ISS stage information at baseline or who lack WGS information for cytogenetic risk stratification were omitted from the survival analysis.

https://doi.org/10.1038/s43018-025-01072-4

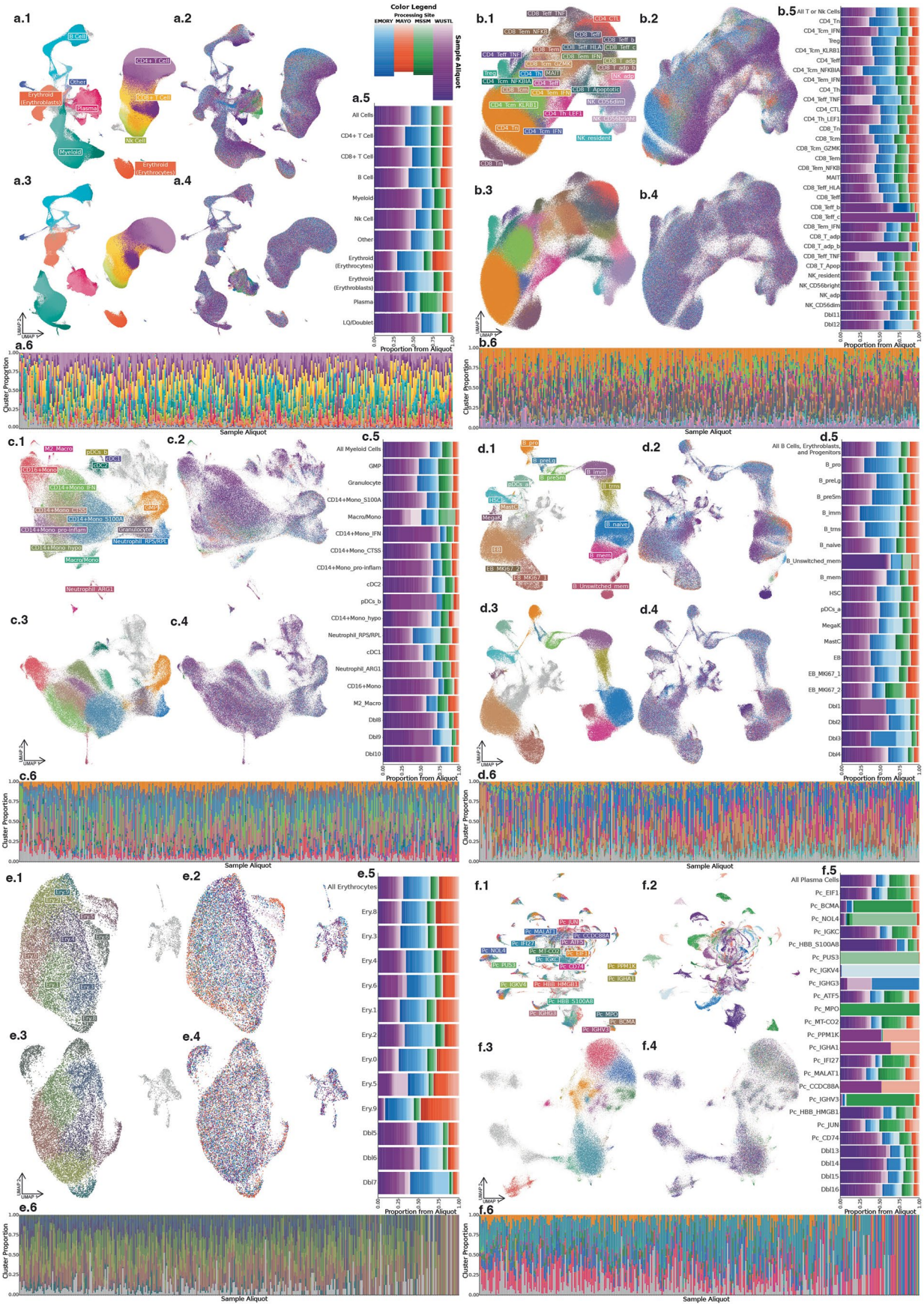

Extended Data Fig. 2 | See next page for caption.

https://doi.org/10.1038/s43018-025-01072-4

Extended Data Fig. 2 | Evaluation of Batch Effects in the scRNA-seq data. UMAP projections and per-sample cluster compositions across immune and tumor cell compartments, illustrating the effects of batch correction using Harmony approach. Each panel (**a-f**) corresponds to distinct cellular compartments, including (**a**) all cells, (**b**) T and natural killer cells, (**c**) myeloid cells, (**d**) B cells, erythroblasts, and progenitors, (**e**) erythrocytes, and (**f**) plasma cells, further subdivided into 6 subpanels (**x.1-x.6**). In panel (**a**), each cluster is colored by their lineage group, with different shades distinguishing the clusters *(see* Fig. 2a-c*)*. In panels (**b-f**), clusters are colored by their sub-compartment colors *(see* Fig. 2d-i, *Extended Data 3)*. Subpanels (**x.1-x.4**) display UMAPs before (**x.1-x.2**) and after (**x.3-x.4**) Harmony batch correction, colored by cell type (**x.1**, **x.3**) with doublets marked in gray or by processing site (**x.2**, **x.4**) with individual sample aliquots distinguished by lighter or darker shades of the respective color (Emory: blue, Mayo: red, MSSM: green, WUSTL: purple). (**x.5**) Stacked bar charts highlighting the sample aliquots contributing to each (**a.5**) lineage group or (**b.5-f.5**) cluster, where the size of each segment is proportional to the number of cells coming from a given sample in the respective population and colored as described in panels x.2 and x.4. (**x.6**) Stacked bar charts displaying the cellular composition within individual aliquots, where the size of each segment is proportional to the cells associated with that cluster as a fraction of all cells in the corresponding compartment, colored by cluster as described in panels x.1 and x.3.

https://doi.org/10.1038/s43018-025-01072-4

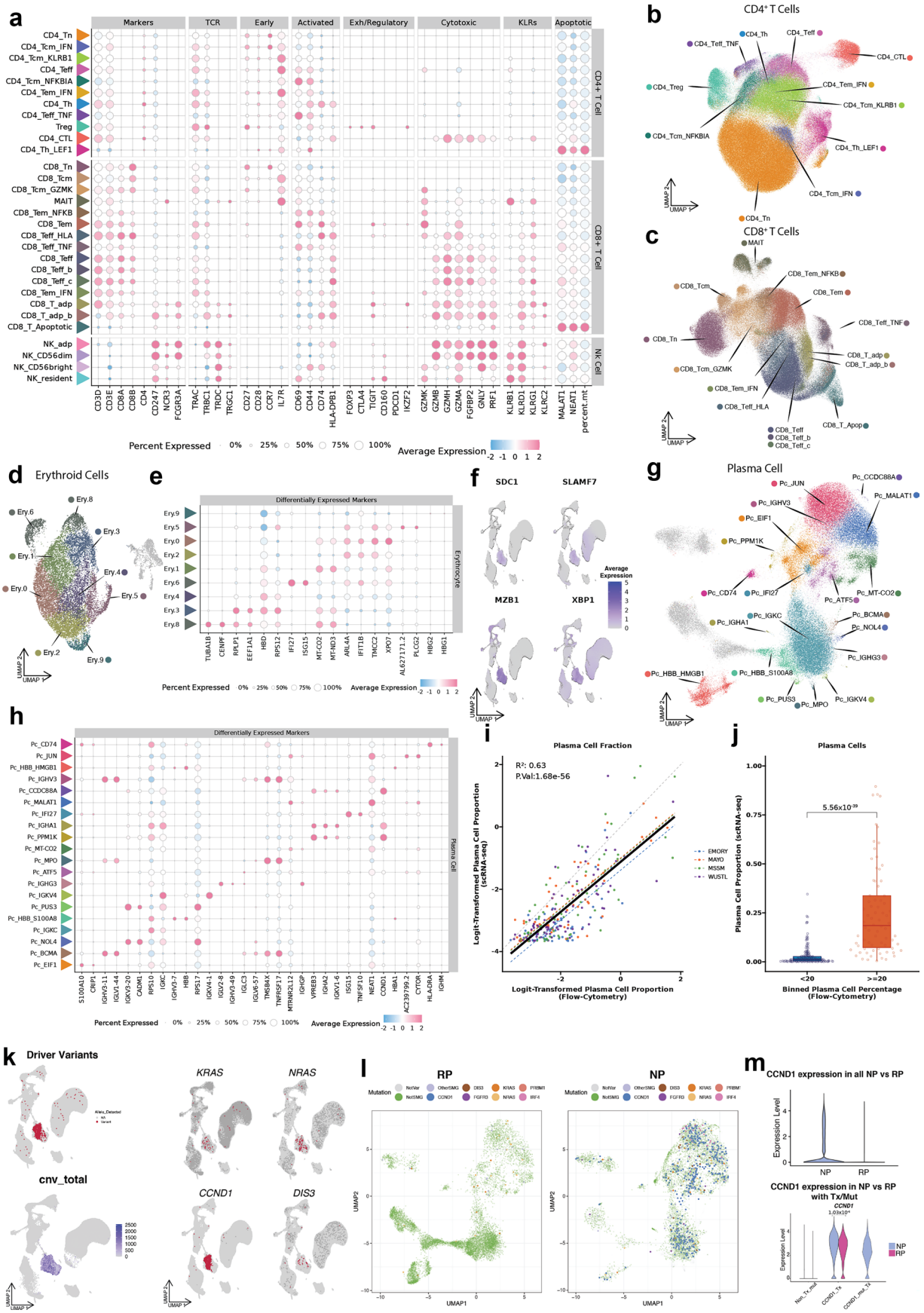

Extended Data Fig. 3 | See next page for caption.

https://doi.org/10.1038/s43018-025-01072-4

Extended Data Fig. 3 | Extended Cell Type Annotation information. (**a**) Dot plot displaying additional markers for $CD4^+$ T, $CD8^+$ T, and natural killer cell annotations. Scaled expression values for each gene are visualized on a red-blue color scale, with the size of each dot representing the percent expression of the corresponding gene. The colored triangle next to each cell name corresponds to the T and NK cell clusters (see Fig. 2d). (**b-c**) UMAPs displaying subclusters of $CD4^+$ T cells (**b**) and $CD8^+$ T cells (**c**). (**d-e**) UMAP (**d**) and dot plot displaying the top differentially expressed markers (**e**) for mature erythrocyte populations. (**f**) Feature plot displaying plasma cell markers. UMAP embeddings correspond to those displayed in Fig. 2a. (**g-h**) UMAP (**g**) and dot plot displaying the top differentially expressed markers (**h**) for the plasma cell compartment. (**i**) Scatter plot showing the relationship between logit-transformed plasma cell proportions in $CD138^{neg}$ scRNA-seq data and plasma cell fractions estimated via flow cytometry on unsorted aspirates. Each dot represents an individual sample, colored by processing site. The black line with p and R^2 values represents the line of best fit average across processing sites, where dashed color lines represent fits for individual processing sites. (**j**) Box plot depicting the plasma cell proportion in the scRNA-seq data for each patient ($n_{patient}$=263). Patients are binned based on whether their plasma cell fraction is ≥20% ($n_{patient}$=74) or <20% ($n_{patient}$=189), as estimated by flow cytometry on unsorted samples. Two-sided p-values comparing the groups is estimated via a linear model. In the box plots, bounds of the box represent the 25^{th} and 75^{th} percentile, with the center displaying the median. Whiskers extend to 1.5*IQR beyond the bounds of the box. (**k-m**) Analyses to assess for malignancy of the plasma cells in the $CD138^{neg}$ scRNA-seq data. (**k**) UMAP highlighting cells with driver overall and individual gene mutations in red and inferred copy number in purple. UMAP embeddings correspond to those displayed in Fig. 2a (**l**) UMAP of all cell types of RP (*left*) or NP (*right*) cohort samples showing various driver mutations. (**m**) *CCND1* expression across cells in the RP vs NP patient cohorts *(top)*. *CCND1* expression in cells from patients with mutations (mut) and/or translocations (Tx) determined based on analysis of WES and WGS data (*bottom*). Unadjusted p-values from a wilcoxon rank-sum test between RP and NP samples is displayed if significant.

https://doi.org/10.1038/s43018-025-01072-4

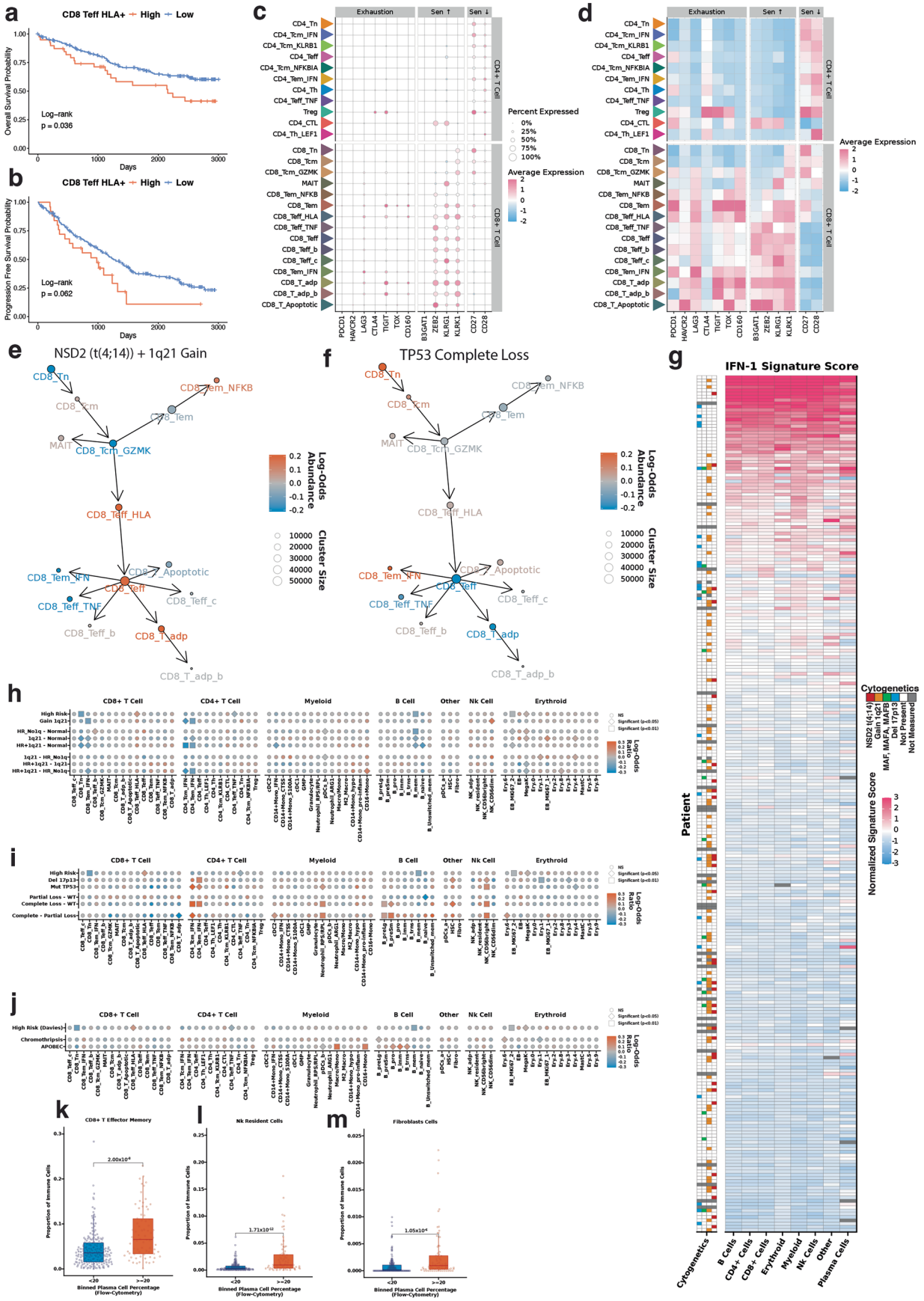

Extended Data Fig. 4 | See next page for caption.

https://doi.org/10.1038/s43018-025-01072-4

Extended Data Fig. 4 | Summary of Cytogenetic Risk Associated Immune Alterations in Multiple Myeloma. (**a**) Survival based on CD8 Teff HLA$^+$ cell abundance as a fraction of CD8$^+$ T cells (p = 0.036, log-rank test). Cell abundances were batch-corrected using regression residuals. Cut-off was determined by maximally selected rank statistics at the 82% quantile (191 low, 39 high). (**b**) Progression-free survival analysis from regression of the above described CD8 Teff HLA$^+$ metrics (p = 0.062, log-rank test) with cutoff set at the 89% quantile (205 low, 25 high). (**c**-**d**) Scaled expression of 'dysfunctional' T cell signature genes, including exhaustion and senescence markers (Supplementary Table 4). Dot plot (**c**) showing percent of cells expressing each gene with dot size and average expression with color (red = high, blue = low) and tile plot (**d**) showing average expression across cluster. Rows are clusters, and columns are genes, grouped by signature category. (**e**-**f**) Trajectory plots depict the predicted differentiation of CD8$^+$ T cell subtypes from CD8$^+$ naïve T cells. Arrows indicate directionality and dots represent trajectory clusters colored by batch-adjusted log-odds abundance and sized by cell count. Comparisons shown for patients with both t(4;14)[*NSD2*] and 1q21 gain (**e**) and TP53 complete loss (**f**) compared to those without them (orange = high, blue = low). (**g**) Per patient heatmap of overall IFN-I response signature scores. Red corresponds to high signature score, blue corresponds to a lower signature score. Signature scores are normalized within each cell lineage. Patients with no cells of a specific type will have a grey bar for their IFN-I signature score. Patient tumor cytogenetics are displayed in a title map to the left of the signature score plot. (**h**) Dot plots of differential cellular abundance analysis for patients with 1q21 gain in combination with other high-risk abnormalities. Each row corresponds to a comparison between 1q21 and other cytogenetic events. "HR_No1q" = high risk without 1q21 gain; "HR+1q21" = high risk with 1q21 gain. Colors indicate log-odds ratios, and shapes indicate two-sided p-values comparing cluster proportions from a linear model (circle = ns, diamond = $p < 0.05$, square = $p < 0.01$). (**i**) Dot plot of differential cellular abundance analysis for patients with partial or complete loss of TP53 via mutation or copy number loss. Partial loss is defined as either monoallelic loss of 17p13 or one non-synonymous mutation of *TP53*. Complete loss is defined as biallelic loss of 17p13 or monoallelic loss of 17p13 with mutation. (**j**) Dot plot summarizing differential cellular abundance analysis for patients with Chromothripsis or APOBEC events. (**k**-**m**) Box plots illustrating the relationship between bone marrow plasma percentages (>=20%, $n_{patient} = 74$; <20%, $n_{patient} = 189$), as estimated via flow cytometry before CD138 isolation (x-axis), and the abundance of CD8$^+$ T effector memory cells ($n_{patient}$=263) (**k**), BM-resident NK cells (**l**), and fibroblasts (**m**). Two-sided p-values for each comparison were computed using a linear model. In the box plots, bounds of the box represent the 25th and 75th percentile, with the center displaying the median. Whiskers extend to 1.5*IQR beyond the bounds of the box.

https://doi.org/10.1038/s43018-025-01072-4

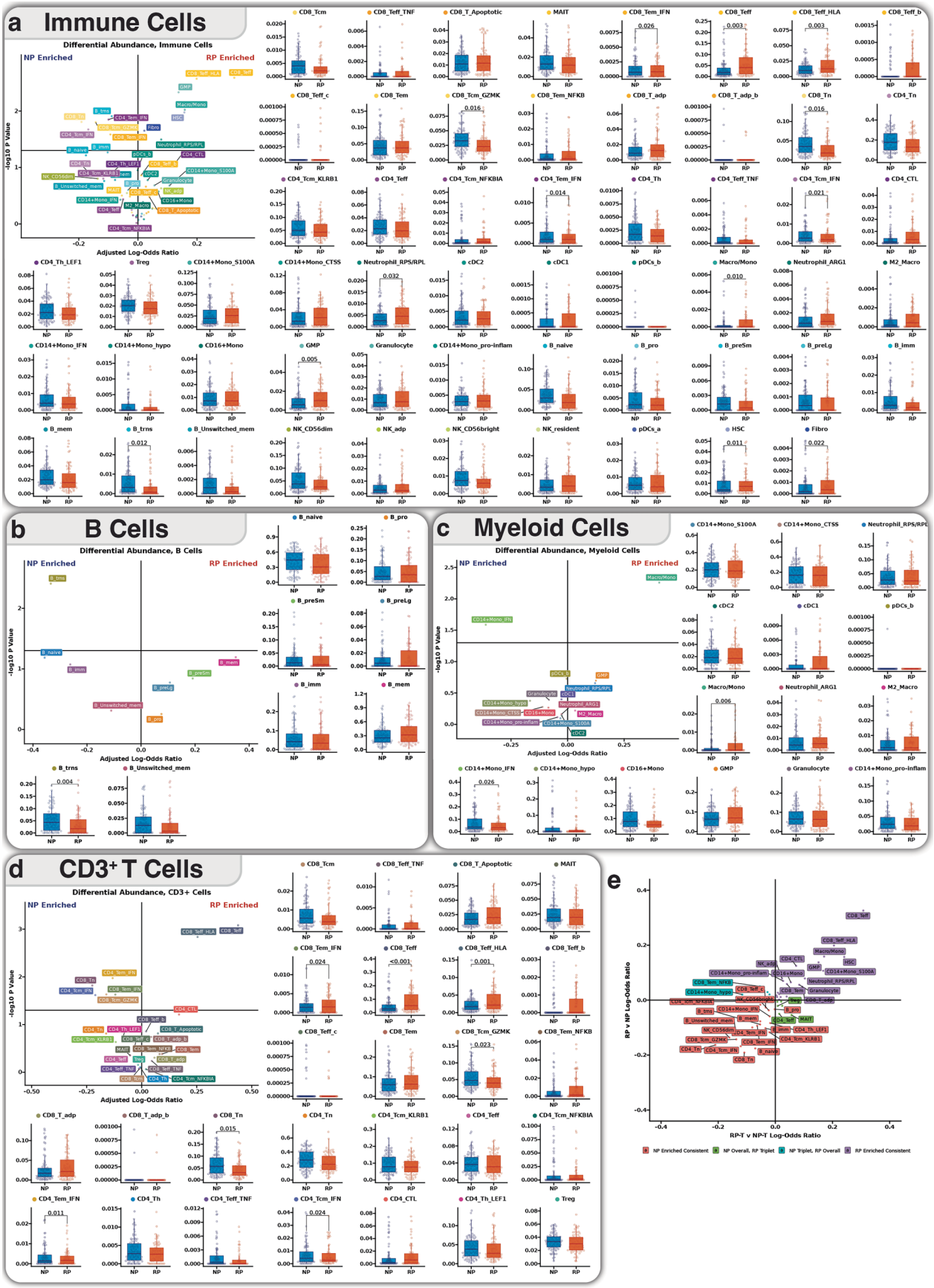

Extended Data Fig. 5 | See next page for caption.

https://doi.org/10.1038/s43018-025-01072-4

Extended Data Fig. 5 | Differential abundance analyses for immune subpopulations comparing rapid progressors versus non-progressors. (**a-d**) Summary differential abundance volcano plots and individual cluster box plots, computed as either a fraction of (**a**) all immune cells, (**b**) B cells, (**c**) myeloid cells, or (**d**) $CD3^+$ cells, comparing RP and NP patients. Each panel consists of a volcano plot in the top left, displaying the log-odds ratio (x-axis) derived from a site-adjusted linear model associating progression group with logit-transformed cell proportions, and the y-axis displays the -log10 of the two-sided p-value from the linear model. Points are colored according to cluster identity in Fig. 2.
Box plots depict the per-patient proportion for each cluster within each compartment, with individual patients shown as open circles (Rapid Progressors (RP, $n_{patient} = 67$)=Orange, Non-Progressors (NP, $n_{patient} = 83$)= Blue). Two-sided p-values are displayed above the box plot if the populations are significantly different between RP and NP ($p < 0.05$) as assessed using a linear model. In the box plots, bounds of the box represent the 25^{th} and 75^{th} percentile, with the center displaying the median. Whiskers extend to 1.5*IQR beyond the bounds of the box. (**e**) Comparison of differential abundance profiles between triplet therapy patients and the overall cohort. The x and y axes display log-odds ratio change in proportion between RP (positive) and NP (negative) patients across triplet therapy patients (x-axis) or all patients (y-axis) as a fraction of immune cells.

https://doi.org/10.1038/s43018-025-01072-4

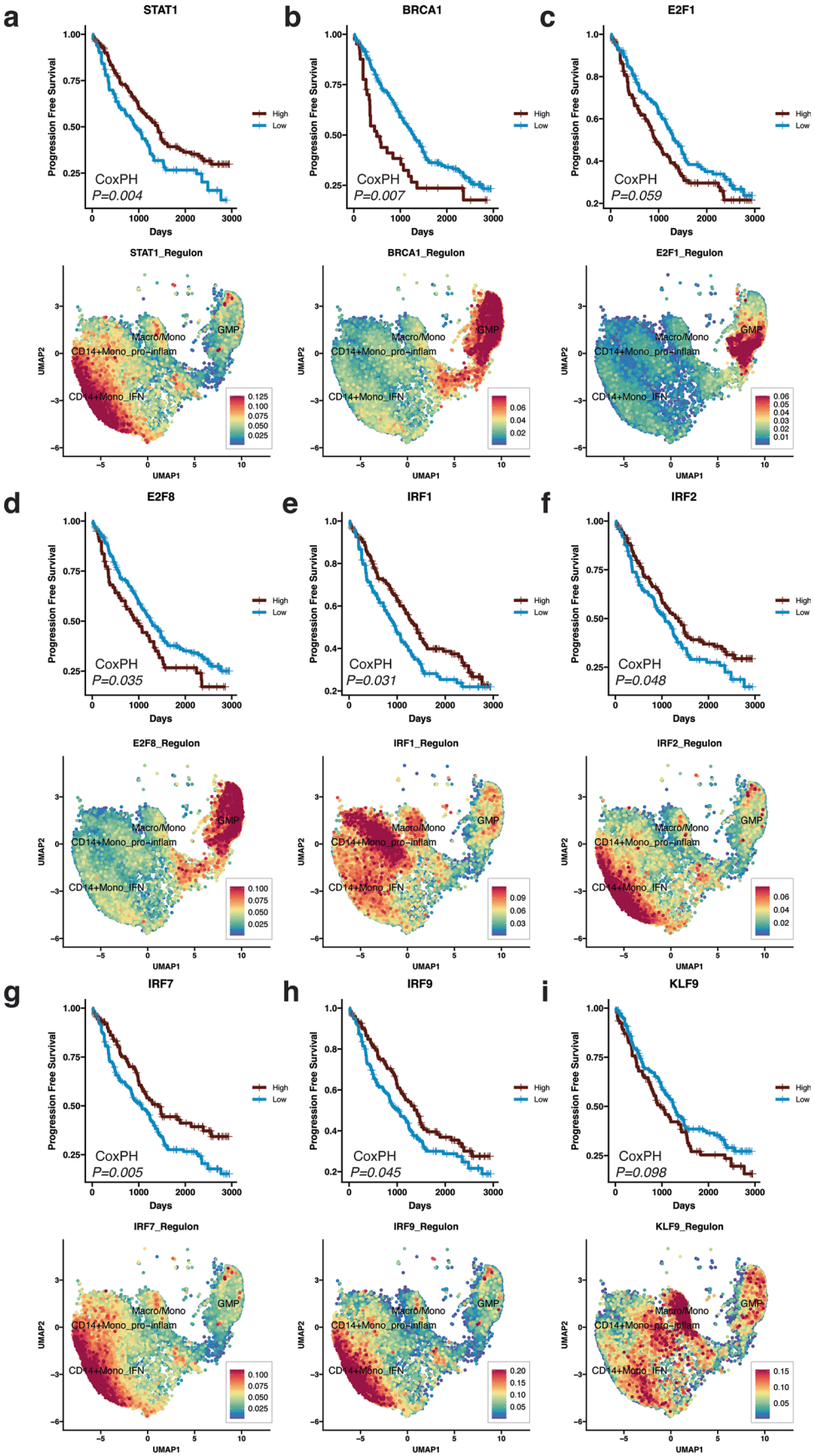

Extended Data Fig. 6 | See next page for caption.

https://doi.org/10.1038/s43018-025-01072-4

Extended Data Fig. 6 | Selected gene regulators and their survival associations in myeloid populations. Kaplan-Meier curves *(top)* and feature plots displaying the per-cell AUC scores *(bottom)* in selected myeloid populations for STAT1 (**a**), BRCA1 (**b**), E2F1 (**c**), E2F8 (**d**), IRF1 (**e**), IRF2 (**f**), IRF7 (**g**), IRF9 (**h**), and KLF9 (**i**) regulons. Gene regulator analysis and regulon identification were performed using pySCENIC on selected myeloid clusters. Kaplan-Meier curves are based on the average AUC value across the selected myeloid populations. The cut-point approach was implemented to stratify patients into either high or low regulon expression groups. Two-sided p-values indicate the significance of a CoxPH model fitted to the regulon AUC score.

https://doi.org/10.1038/s43018-025-01072-4

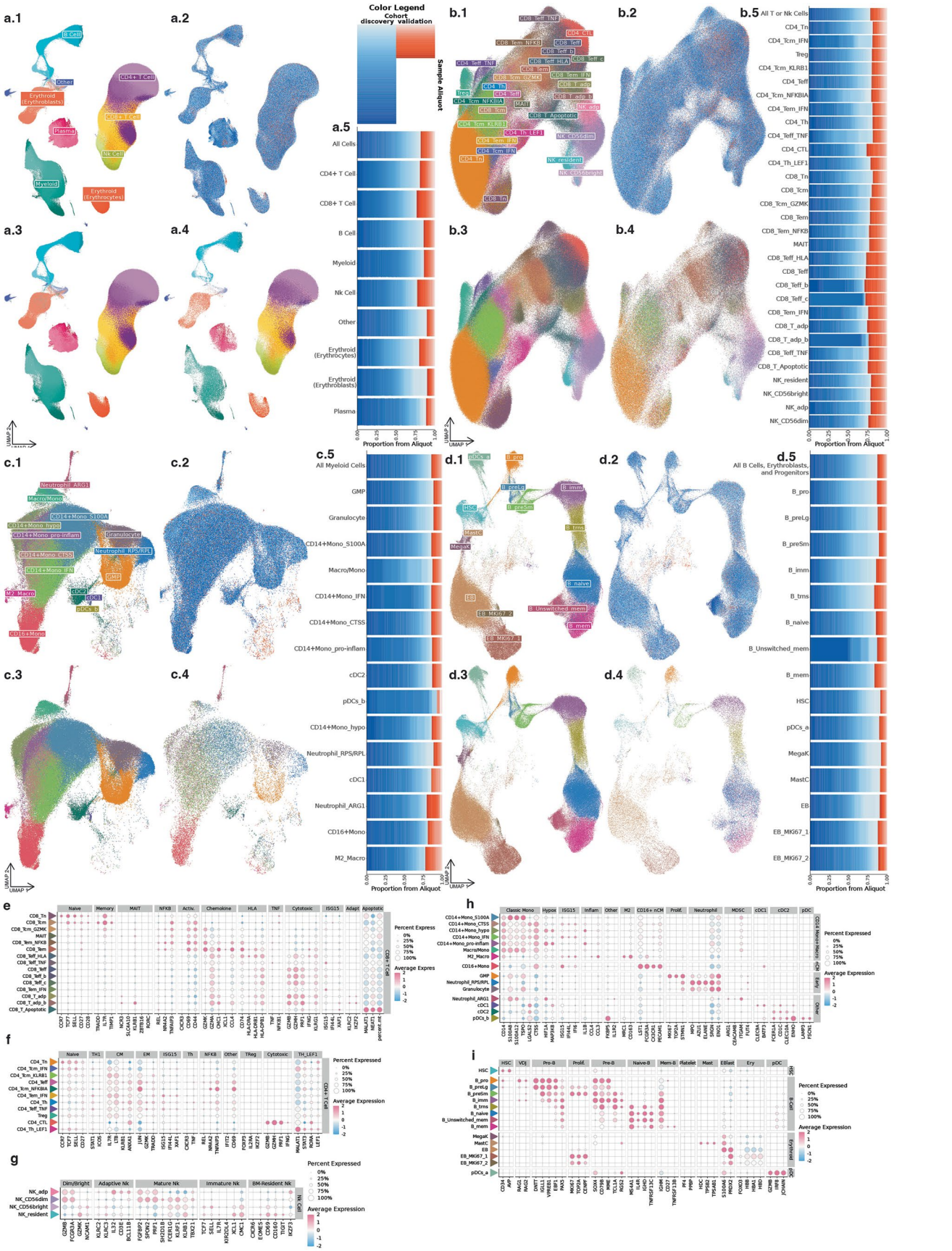

Extended Data Fig. 7 | See next page for caption.

https://doi.org/10.1038/s43018-025-01072-4

Extended Data Fig. 7 | UMAP and dot plot comparisons of validation and discovery cohorts across cell compartments. UMAP projections and stacked bar charts comparing cellular composition between discovery and validation cohorts across major immune cell compartments. Each panel (**a**-**d**) corresponds to a distinct cellular compartment including (**a**) all cells, (**b**) NK/T cells, (**c**) myeloid cells and (**d**) B cells, erythroblasts and progenitor cells, further subdivided into 5 subpanels (**x.1**-**x.5**). Subpanels (**x.1**-**x.2**) display UMAPS of both discovery and validation cells colored by cell type (**x.1**) or sample (**x.2**). Subpanels (**x.3**-**x.4**) show the same UMAPS separated by discovery (**x.3**) and validation (**x.4**) cohorts, colored by cell type. Subpanels (**x.5**) contain stacked bar charts representing the distribution of cells within each cluster across individual samples and separated by cohort. Samples from the discovery cohort are colored different shades of blue, while samples from the validation cohort are colored different shades of red. (**e**-**i**) Validation cohort dot plot showing the previously described cluster markers for (**e**) $CD8^+$ cells, (**f**) $CD4^+$ cells, (**g**) natural killer cells, (**h**) myeloid cells, and (**i**) B cells, erythroblasts, and progenitor cells.

https://doi.org/10.1038/s43018-025-01072-4

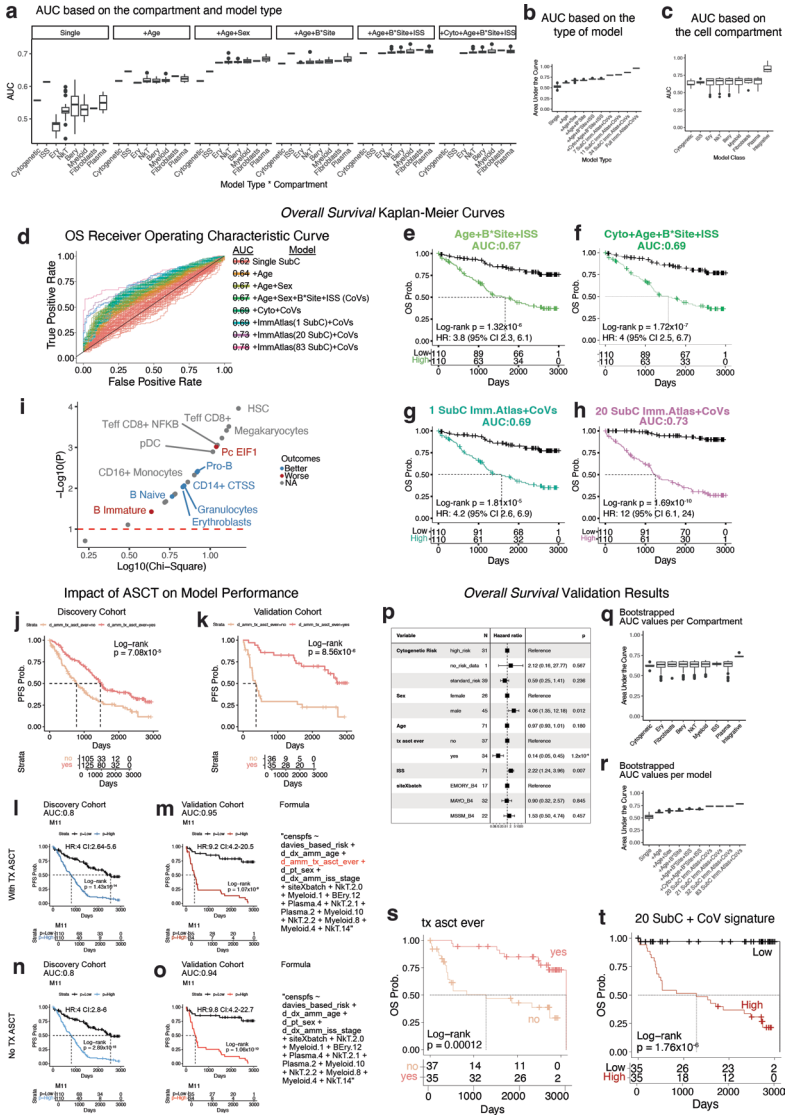

Extended Data Fig. 8 | Additional Model Diagnostics and Predictive Modeling of Overall Survival and Progression in MM Using Immune Signatures, Cytogenetics, and Clinical Features. Panels (**a-c**) show model AUCs in the discovery cohort across immune compartments: (**a**) AUCs by immune cell compartments and variable combinations, (**b**) Boxplots showing the distribution of AUCs for models integrating a single cell type with various covariates, along with the AUC for the top models integrating all clinical covariates and either 7, 11, 34, or all immune populations, and (**c**) Boxplots showing the AUCs for models derived from individual immune populations, grouped by cellular compartment. In the box plots, bounds of the box represent the 25th and 75th percentile, with the center displaying the median. Whiskers extend to 1.5*IQR beyond the bounds of the box. Whiskers extend to 1.5*IQR beyond the bounds of the box. (**d-i**) Receiver operating characteristic (ROC) and Kaplan-Meier (KM) analysis for overall survival (OS) prediction in the discovery cohort. (**d**) ROC curves for models with single immune subclusters (SubC), clinical covariates (CoV), cytogenetics, and combinations. Covariates include age, batch, site, ISS stage and cytogenetics. KM curves depict predicted OS based on (**e**) clinical covariates (**f**) cytogenetics + clinical covariates, (**g**) Immune Atlas Signature + clinical covariates, and (**h**) the top 20 predictive immune subclusters + clinical covariates. (**i**) The importance of immune subclusters for predicting the OS colored by favorable (blue) or poor (red) OS association. (**j-o**) ASCT's contribution to survival prediction in discovery and validation cohorts. KM curves showing ASCT association with OS in discovery (**j**) and validation (**k**) cohorts. Predictive models including ASCT, cytogenetics, clinical variables, and top immune features in discovery (**l**) and validation (**m**). Equivalent models excluding ASCT as a variable, still stratifying high- versus low-risk patients in discovery (**n**) and validation (**o**) cohorts. (**p-t**) OS prediction in the validation cohort. (**p**) A forest plot based on a multivariate CoxPH illustrating the bias of ASCT and ISS for OS. Two-sided p-values from the CoxPH model are displayed. (**q**) Box plot of bootstrapped AUCs for models using various immune compartments ($n_{patient}$=71), with the integrative model as a superior option. However, the AUC for OS remained below 0.75 in general. (**r**) Box plot of bootstrapping applied to an integrative model of feature selection based on AUC to identify the optimal model for OS prediction using immune populations, clinical information, cytogenetics, and ASCT. In the box plots, bounds of the box represent the 25th and 75th percentile, with the center displaying the median. Whiskers extend to 1.5*IQR beyond the bounds of the box. (**s**) KM curves show the effect of ASCT on the prediction of OS. (**t**) Integrative model using the top 20 immune signatures combined with clinical and cytogenetic information in the prediction of OS.

https://doi.org/10.1038/s43018-025-01072-4

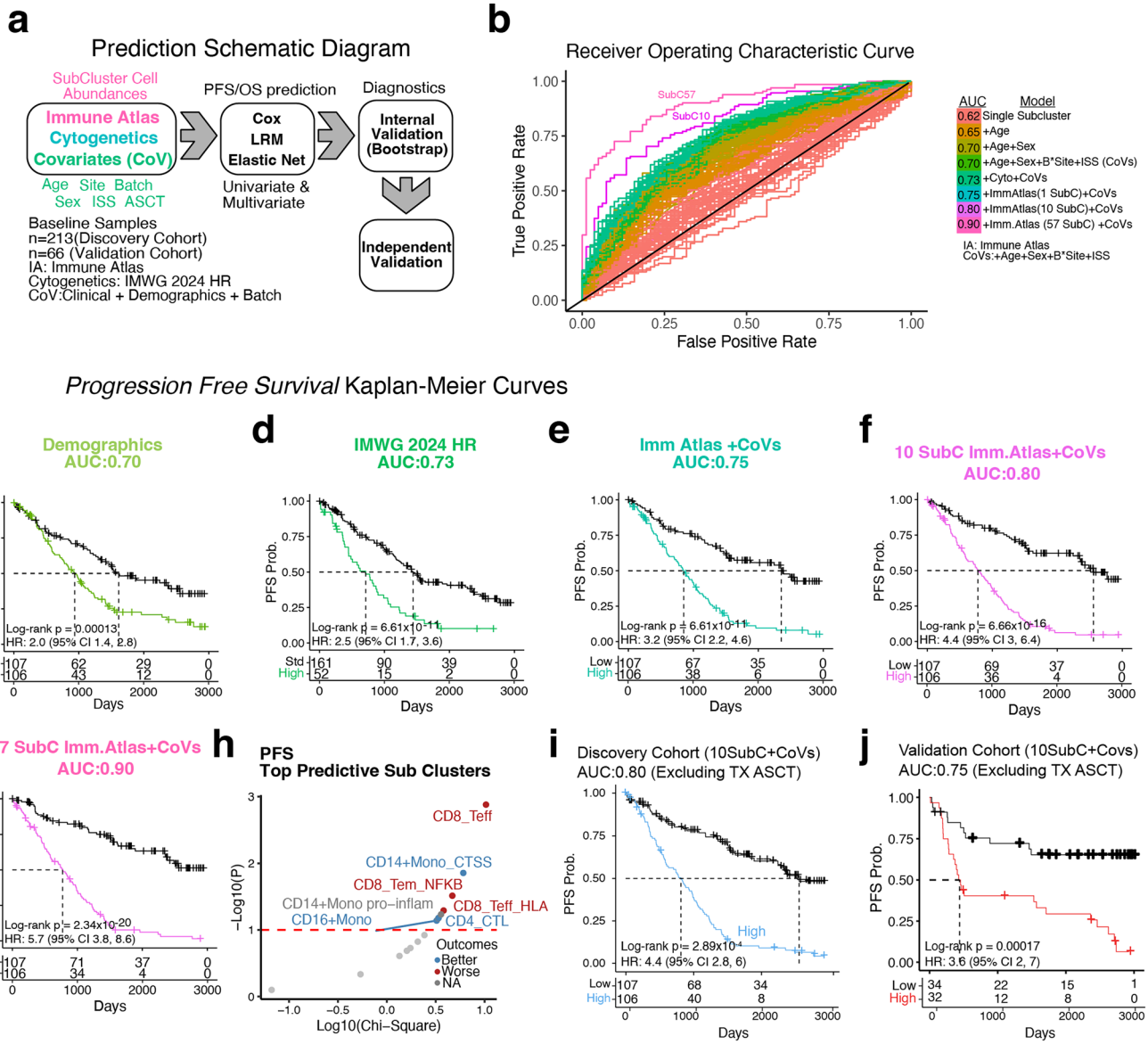

Extended Data Fig. 9 | See next page for caption.

https://doi.org/10.1038/s43018-025-01072-4

Extended Data Fig. 9 | Prediction of MM progression by integration of IMWG cytogenetics risk along with immune signatures. (**a**) Diagram illustrating the type of variables that were tested (immune signatures, IMWG cytogenetics, and clinical covariates) followed by the three regression strategies used (elastic net, logistic regression, and Cox) with bootstrap validation for model selection. (**b**) Receiver operating characteristic (ROC) curves for progression prediction models based on single clusters, clinical variables, and cytogenetics or immune atlas variables alone and in combination are shown and colored based on the specific group of models. The labels include subclusters (SubC) and covariates (CoV), which include age, batch, site, ISS, and cytogenetics. Kaplan-Meier curves showing the separation of patients with high or low scores for prediction of PFS are shown for (**c**) demographics-based, (**d**) IMWG 2024 high-risk criteria, and (**e**) Immune Atlas signatures. Kaplan-Meier curves show the separation of patients when cytogenetic risk scores are combined with the (**f**) best 10 predictive immune atlas subclusters or (**g**) 57 subclusters. (**h**) Volcano plot displaying the importance of immune subclusters for predicting the progression based on the coefficients from the modeling. The clusters with better and poor MM outcomes are shown with blue and red colors, respectively. Receiver operating characteristic (ROC) curves for using 10 subclusters and excluding ASCT for discovery (**i**) and validation (**j**) cohorts. (**k**) Dot plot showing the average scaled expression of marker genes for the "MatNeut2" phenotype reported in Jong et al., 2024. Expression is visualized on a red-blue color scale, with the size of each dot corresponding to the percent expression of marker genes. Expression is normalized relative to the average cluster expression across all $CD14^+$ monocyte clusters.

nature portfolio

Corresponding author(s): George Mulligan, PhD, Li Ding, PhD, Sacha Gnjatic, PhD, Ioannis Vlachos, PhD, Manoj Bhasin, PhD

Last updated by author(s): Oct 6th, 2025

Reporting Summary

Nature Portfolio wishes to improve the reproducibility of the work that we publish. This form provides structure for consistency and transparency in reporting. For further information on Nature Portfolio policies, see our Editorial Policies and the Editorial Policy Checklist.

Statistics

For all statistical analyses, confirm that the following items are present in the figure legend, table legend, main text, or Methods section.

n/a	Confirmed
☐	☒ The exact sample size (*n*) for each experimental group/condition, given as a discrete number and unit of measurement
☐	☒ A statement on whether measurements were taken from distinct samples or whether the same sample was measured repeatedly
☐	☒ The statistical test(s) used AND whether they are one- or two-sided *Only common tests should be described solely by name; describe more complex techniques in the Methods section.*
☐	☒ A description of all covariates tested
☐	☒ A description of any assumptions or corrections, such as tests of normality and adjustment for multiple comparisons
☐	☒ A full description of the statistical parameters including central tendency (e.g. means) or other basic estimates (e.g. regression coefficient) AND variation (e.g. standard deviation) or associated estimates of uncertainty (e.g. confidence intervals)
☐	☒ For null hypothesis testing, the test statistic (e.g. *F*, *t*, *r*) with confidence intervals, effect sizes, degrees of freedom and *P* value noted *Give P values as exact values whenever suitable.*
☒	☐ For Bayesian analysis, information on the choice of priors and Markov chain Monte Carlo settings
☐	☒ For hierarchical and complex designs, identification of the appropriate level for tests and full reporting of outcomes
☐	☒ Estimates of effect sizes (e.g. Cohen's *d*, Pearson's *r*), indicating how they were calculated

Our web collection on statistics for biologists contains articles on many of the points above.

Software and code

Policy information about availability of computer code

Data collection: No software was used for data collection.

Data analysis	Code involved in the processing and analysis of single-cell RNA sequencing data has been deposited on GitHub https://github.com/theMMRF. Cell Ranger v6.0.1 was used for alignment of sequencing data to the GRCh38 reference genome. DropletUtils (v1.14.2) was used for empty droplet removal. CellBender (v0.3.0) was used to remove ambient RNA. DoubletFinder, Scrublet (v0.2.3), and Pegasus (v1.8.1) were used for doublet identification. Seurat (v4.3) R package was used for single-cell analyses. Harmony (v0.1) was used for batch correction. Limma was used for differential expression and abundance analysis. RStatix (v0.7.2) and DirichletReg (v0.7-1) were used for differential abundance analysis. Survival (v3.2.7) and survminer (v0.4.9) packages were used for survival analyses. Slingshot (v2.6.0) was used for trajectory analysis. UCell (v2.2.0) was used for signature score calculation. ReactomePA (v1.42.0) was used for gene set enrichment analysis. CellChat (v2.1.0) was used for cell-cell communication analysis. pySCENIC (v0.12.1) was used for gene regulatory network analysis. FNN (v1.1.4) was used for label transfer. edgeR (v4.0.16) was used for processing bulk or pseudobulked counts data. GSVA (v1.15.0) was used for computing signature scores on bulk or pseudobulked counts data.

For manuscripts utilizing custom algorithms or software that are central to the research but not yet described in published literature, software must be made available to editors and reviewers. We strongly encourage code deposition in a community repository (e.g. GitHub). See the Nature Portfolio guidelines for submitting code & software for further information.

Data

Policy information about availability of data

All manuscripts must include a data availability statement. This statement should provide the following information, where applicable:

- Accession codes, unique identifiers, or web links for publicly available datasets
- A description of any restrictions on data availability
- For clinical datasets or third party data, please ensure that the statement adheres to our policy

All the single-cell raw data, processed summary data and clinical information used for this project are under controlled access at MMRF's VLAB shared resource. MMRF requires anyone interested in accessing the data apply for access at https://mmrfvirtuallab.org and to meet following minimum qualifications: 1) must be a permanent employee of their institution and at a level equivalent to a tenure-track professor, 2) senior investigator that is overseeing laboratory or research program. If the access request is approved, usually within a week, investigators will receive an email with instructions to download the data.
Alternatively, a Seurat object with limited meta data is available at Zenodo (doi: 10.5281/zenodo.11150168). Zenodo additionally contains a copy of the Immune Atlas Cell Annotation Dictionary, which provides additional information about cluster annotation and marker expression for those who wish to use the pre-annotated dataset. Source data for Figures 1-7, and Extended Data Figures 1-9 have additionally been provided as Source Data files. For all other additional inquiries, please email ImmuneAtlasNetwork@themmrf.org.

Research involving human participants, their data, or biological material

Policy information about studies with human participants or human data. See also policy information about sex, gender (identity/presentation), and sexual orientation and race, ethnicity and racism.

Reporting on sex and gender	Metadata from patients in this cohort includes Sex (biologic attribute) but not gender. The frequency of "Male" and "Female" patients with respect to our primary covariates of interest (Risk, Progression) are provided. Survival analysis comparing the outcomes of male and female patients in our dataset are also shown. We did not observe significant associations with sex and either risk or outcomes.
Reporting on race, ethnicity, or other socially relevant groupings	Metadata from patients include self reported race and ethnicity. We did not identify any significant association between race and our covariates of interest. Subsequent analysis do not focus on race currently in this paper.
Population characteristics	Patients had newly diagnosed, previously untreated multiple myeloma. Patients are from the MMRF CoMMpass study, which recruited from 84 clinical sites located in the United States, Canada, Spain, and Italy. Our analysis primarily focuses on cytogenetic risk stratification, and progression free survival. In addition to sex, race, and ethnicity, patient age at diagnosis, BMI, ISS stage, ECOG assessment, first induction therapy, and whether the patient did or did not receive ASCT in their first line are also described.
Recruitment	Samples from this analysis were derived from patients enrolled in the CoMMpass study (NCT01454297). The criteria for inclusion in this study are as follows: Inclusion Criteria: Patient is at least 18 years old. Patient has been diagnosed with symptomatic MM with measurable disease that includes at least one of the following: Serum M protein ≥ 1g/dl Urine M protein ≥ 200 mg/24 hrs Involved free light chain level ≥ 10 mg/dl and an abnormal serum free light chain ratio (<0.26 or >1.65). The patient is a candidate for systemic therapy that includes an IMiD® (e.g., lenalidomide, pomalidomide, thalidomide) and/or proteasome inhibitor (e.g., bortezomib, carfilzomib) as part of the initial regimen. No more than 30 days from baseline bone marrow evaluation as per this protocol to initiation of first-line therapy. Patient has read, understood and signed informed consent.

Exclusion Criteria:
Patient is already receiving systemic therapy for MM (a single dose of bisphosphonates and up to 100 mg total dose of dexamethasone or equivalent corticosteroids are permitted prior to registration on study).
Patient had another malignancy within the last 5 years (except for basal or squamous cell carcinoma, or in situ cancer of the cervix).
Patient is enrolled in a blinded clinical trial for the first-line treatment of multiple myeloma. Patients may be enrolled in subsequent clinical trials as long as continued access to data and tissue, as per this protocol, is not prohibited.

Ethics oversight

All samples for the study were obtained from the MMRF CoMMpass clinical trial (NCT01454297). Procedures involving human participants as part of this trial were performed by the ethical standards of the MMRF research committee. Written informed consent was obtained from patients for the collection and analysis of samples and clinical information by the MMRF. The Institutional Review Board at each participating medical center approved the study protocol. The list of participating institutes that have approved the study protocol is available at ClinicalTrials.gov (NCT01454297).

Note that full information on the approval of the study protocol must also be provided in the manuscript.

Field-specific reporting

Please select the one below that is the best fit for your research. If you are not sure, read the appropriate sections before making your selection.

☒ Life sciences ☐ Behavioural & social sciences ☐ Ecological, evolutionary & environmental sciences

For a reference copy of the document with all sections, see nature.com/documents/nr-reporting-summary-flat.pdf

Life sciences study design

All studies must disclose on these points even when the disclosure is negative.

Sample size	This analysis focuses on 337 patients from the MMRF CoMMpass study. No formal statistical analysis was used to estimate the number of samples required for this study. The number of samples chosen would target over ~1 million cells, which would allow for high resolution of the bone marrow immune compartment.
Data exclusions	Samples from patients who received standard triplet or doublet therapy, and had CD138-negative bone marrow samples available at baseline were select for analysis. This sub-cohort of patients shows similar demographic and clinical characteristics to the full CoMMpass study. Two scRNA-seq samples were excluded prior to downstream analysis, in which greater than 65% of cells from the sample were identified as mm10 spike-in cells.
Replication	This study follows a previous pilot study on the feasibility of a multi-center, single-cell RNA sequencing analysis (Yao et al., 2022, Pilcher et al., 2023). Samples for analysis was split across four different medical centers and universities, in four different shipment batches. Batch effects between processing center and shipment batch were controlled for throughout analysis. External data for validation is not currently available.
Randomization	Samples are from an observational clinical trial and no randomization was performed. Therapy selection was determined by the physician. Patient categorization is based on observed patient outcomes or cytogenetics.
Blinding	In the observational trial, site investigators and analysts were not blinded to therapy selected. Patient groupings were based on observed outcomes or cytogenetic information.

Reporting for specific materials, systems and methods

We require information from authors about some types of materials, experimental systems and methods used in many studies. Here, indicate whether each material, system or method listed is relevant to your study. If you are not sure if a list item applies to your research, read the appropriate section before selecting a response.

Materials & experimental systems

n/a	Involved in the study
☐	☒ Antibodies
☐	☒ Eukaryotic cell lines
☒	☐ Palaeontology and archaeology
☒	☐ Animals and other organisms
☐	☒ Clinical data
☒	☐ Dual use research of concern
☒	☐ Plants

Methods

n/a	Involved in the study
☒	☐ ChIP-seq
☐	☒ Flow cytometry
☒	☐ MRI-based neuroimaging

Antibodies

Antibodies used: CD38 (BD Biosciences, 340677), CD45/PTPRC (BD Biosciences, 340665), CD138/SDC1 (BD Biosciences, 347205), CD319/SLAMF7

Antibodies used	(Invitrogen/eBioscience, 12-2229-42), CD13/ANPEP (BD Biosciences, 340686), CD19 (BD Biosciences, 340720), CD20/MS4A1 (BD Biosciences, 346581), CD27 (BD Biosciences, 654665), CD28 (BD Biosciences, 348047), CD33 (BD Biosciences, 340679), CD52 (Life Technologies, MHCD5204), CD56/NCAM1 (BD Biosciences, 340724), CD117/KIT (BD Biosciences, 340867), FGFR3/CD333 (R&D Systems, FAB766P), Kappa (BD Biosciences, 643774), and Lambda (Life Technologies, MH10614)
Validation	Flow cytometry was conducted in a CAP/CLIA lab as a laboratory developed test at Spectrum Health, Grand Rapids Michigan

Eukaryotic cell lines

Policy information about cell lines and Sex and Gender in Research

Cell line source(s)	NIH/3T3 Cells (ATCC CRL-1658). Cell lines were purchased directly from ATCC.
Authentication	Cell lines are authenticated by ATCC. No additional authentication was performed.
Mycoplasma contamination	No mycoplasma contamination was detected by ATCC. No additional testing for mycoplasma contamination was performed.
Commonly misidentified lines (See ICLAC register)	No commonly misidentified cell lines were used in this study.

Clinical data

Policy information about clinical studies

All manuscripts should comply with the ICMJE guidelines for publication of clinical research and a completed CONSORT checklist must be included with all submissions.

Clinical trial registration	NCT01454297
Study protocol	This is a non-interventional clinical trial investigating the association of outcomes with molecular markers in multiple myeloma. Additional information on the study protocol is accessible on clinicaltrials.gov (https://clinicaltrials.gov/study/NCT01454297)
Data collection	Patients in the MMRF CoMMpass study were enrolled from sites in Canada, Spain, and the United States between the years of July 2011 and June 2015. Sites in Italy recruited additional patients until June 2016
Outcomes	The primary objective of the MMRF CoMMpass study was to identify molecular profiles and clinical characteristics that define various subpopulations of multiple myeloma patients at diagnosis and relapse. This paper identifies immunologic subtypes, defined by scRNA-seq expression and cellular abundance profiles, associated with myeloma. This paper also utilizes previously produced tumor cytogenetic and transcriptomic data on tumor cells collected as part of this study. Secondary objectives of the MMRF CoMMpass study was to collect information on progression free survival and overall survival, which are also presented within this manuscript. Targetted observation periods were eight years following initial diagnosis.

Plants

Seed stocks	n/a
Novel plant genotypes	n/a
Authentication	n/a

Flow Cytometry

Plots

Confirm that:

☐ The axis labels state the marker and fluorochrome used (e.g. CD4-FITC).

☐ The axis scales are clearly visible. Include numbers along axes only for bottom left plot of group (a 'group' is an analysis of identical markers).

☐ All plots are contour plots with outliers or pseudocolor plots.

☐ A numerical value for number of cells or percentage (with statistics) is provided.

Methodology

Sample preparation	Not available - Conducted in a CAP/CLIA certified laboratory running a laboratory developed test
Instrument	Not available - Conducted in a CAP/CLIA certified laboratory running a laboratory developed test
Software	Not available - Conducted in a CAP/CLIA certified laboratory running a laboratory developed test
Cell population abundance	Not available - Conducted in a CAP/CLIA certified laboratory running a laboratory developed test
Gating strategy	Not available - Conducted in a CAP/CLIA certified laboratory running a laboratory developed test. Flow cytometry was not performed to separate cells into CD138-positive and CD138-negative components.

☐ Tick this box to confirm that a figure exemplifying the gating strategy is provided in the Supplementary Information.